FACULTY OF ENGINEERING AND ARCHITECTURE

Exploring Methods to Improve the Detection Limit of Waveguide-Enhanced Raman Spectroscopy

Zuyang Liu

Doctoral dissertation submitted to obtain the academic degree of
Doctor of Photonics Engineering

Supervisors
Prof. Roel Baets, PhD - Prof. Nicolas Le Thomas, PhD
Department of Information Technology
Faculty of Engineering and Architecture, Ghent University

May 2023

GHENT UNIVERSITY

ISBN 978-94-6355-710-8
NUR 950
Wettelijk depot: D/2023/10.500/42

Members of the Examination Board

Chair

Prof. Filip De Turck, PhD, Ghent University

Other members entitled to vote

Prof. Jana Jágerská, PhD, The Arctic University of Norway, Norway
Peter Offermans, PhD, imec & OnePlanet Research Center, the Netherlands
Prof. Günther Roelkens, PhD, Ghent University
Prof. Geert Van Steenberge, PhD, Ghent University
Haolan Zhao, PhD, Ghent University

Supervisors

Prof. Roel Baets, PhD, Ghent University
Prof. Nicolas Le Thomas, PhD, Ghent University

Acknowledgements

As a Chinese idiom puts it, hard-working is the boat sailing on the endless ocean of learning. During my doctoral study, I have felt lost countless times in this ocean of learning. Sometimes it comes from a search for solutions to a specific problem, and sometimes it originates from confusion about the way forward. But I was lucky to have my supervisors: Roel Baets and Nicolas Le Thomas. Roel has a wealth of knowledge and experience in his field and a vision ahead of his time. Nicolas has a very solid knowledge of mathematics and physics, as well as an in-depth mastery of experiments. They helped steer my research on the right course and showed me how to continue my own adventure. I would like to express my utmost gratitude to my supervisors. Also, a special thanks must go to Haolan Zhao, who mentored me closely in the first years of my doctoral study. At the start of my study, I could never find my way around without the time he spent teaching me in the lab and answering my questions.

I would like to thank the rest of my examination board: Prof. Filip De Turck, Prof. Jana Jágerská, Dr. Peter Offermans, Prof. Günther Roelkens, and Prof. Geert Van Steenberge. Their valuable effort and time helped achieve a better shape of this thesis.

I have great fellow Ph.D. students and postdocs who are always available for fruitful discussions and generous assistance in the Photonics Research Group. Many of them were members of the Raman group: Xiaomin Nie, Ali Raza, Nina Turk, Kristof Reynkens, and Yang Li. I have cherished insightful discussions during Raman meetings. Beyond the Raman group, I have also received help from Jing Zhang, Grigorij Muliuk, Fabio Pavanello, Zhongtao Ouyang, Tom Vanackere, Jasper De Witte, Maximilien Billet, and many more. There are so many good people in our research group that are always willing to help. Moreover, my friendly and considerate officemates provided me with the atmosphere I needed. Thank you, Camiel, Isaac, Kasper, Lukas, Max, Nina, Stijn Cuyvers, Stijn Poelman, Tom Reep, Tom Vandekerckhove, and Xin, for tolerating me.

The Photonics Research Group cannot remain functional without our great support staff. Whenever I encounter a problem in the measurement room, I always turn

to Jasper Jans, Michael Vanslembrouck, or Clemens Krückel. Like magicians, they could always come up with solutions. I have also turned to another magician, Peter Guns, who constantly supports our wild experiment ideas with great machining work. In the cleanroom, I have received assistance from Liesbet Van Landschoot, Steven Verstuyft, and Muhammad Muneeb with admirable expertise and patience. I am also thankful to Kristien De Meulder, Ilse Van Royen, and Ilse Meersman, who kept the research going on in one way or another.

I feel fortunate to have found many Chinese friends in Gent. The little community provides a comforting sense of home, especially during the pandemic when the home is too far away policy-wise. I will refrain from naming everyone in the Chinese community of PRG as it has grown quite big and can easily take half a page. I want to say a special thanks to Chupao, Hong, Xiangfeng, Xiaoning, Yufei, and Yuting for the bliss we shared, mostly before COVID. Outside the group, I also found warmth with my dearest friends: Fan, Jia, Lei, Mengmeng, Qiming, Sheng, Shiqing, Xiangyu, and Yun.

Lastly, I am particularly thankful to my family. I can only concentrate on my study because of your unconditional support, emotional and financial. The last few years have been difficult due to the pandemic. But I believe everything will be better soon, and I can become a better daughter. And I would like to thank my boyfriend Chonghuai. It is great to have a companion along this journey who understands me so well and supports my decisions.

Gent, 2023
Zuyang Liu

Contents

List of Acronyms

A

ALD	Atomic Layer Deposition
AWG	Arrayed Waveguide Grating

B

BCB	Benzocyclobutene

C

CMOS	Complementary Metal–Oxide–Semiconductor
CTAB	Cetyltrimethylammonium Bromide

D

DI	De-Ionized

E

EBL	Electron Beam Lithography
E-field	Electrical Field

F

FOM	Figure of Merit
FTS	Fourier Transform Spectrometer
FWHM	Full Width at Half Maximum

H

HMDS	Hexamethyldisilazane
HSQ	Hydrogen Silsesquioxane

I

ICP	Inductively Coupled Plasma
IPA	Isopropanol
IR	Infrared

L

LF	Length Factor
LPCVD	Low Pressure Chemical Vapor Deposition

M

MIBK	Methyl Isobutyl Ketone

MO	Microscope Objective
μTP	Micro-Transfer-Printing

N

NA	Numerical Aperture
NIR	Near-Infrared

O

OPA	Optical Phased Array
OSA	Optical Spectrum Analyzer

P

PBS	Polarizing Beam Splitter
PDMS	Polydimethylsiloxane
PECVD	Plasma Enhanced Chemical Vapor Deposition
PIC	Photonic Integrated Circuit

R

RIE	Reactive Ion Etching

S

SBR	Signal-to-Background Ratio
SERS	Surface Enhanced Raman spectroscopy

SMF	Singlemode Fiber
SNR	Signal-to-Noise Ratio
SOI	Silicon-on-Insulator
SRS	Stimulated Raman Spectroscopy

T

TEOS	Tetraethoxysilane
TMAH	Tetramethylammonium Hydroxide

U

UV	Ultra-Violet

W

WERS	Waveguide Enhanced Raman Spectroscopy

Samenvatting

Op verschillende gebieden, waaronder chemie, biologie en farmacie, is er een enorme behoefte aan snelle en nauwkeurige detectie van de chemische samenstelling van een materiaal. Vooral gemultiplexeerde detectie in complexe omgevingen blijft een uitdaging met de huidige methoden. Ramanspectroscopie biedt labelvrije, ondubbelzinnige identificatie van chemische samenstellingen. Hierbij wordt gebruik gemaakt van ramanverstrooiing, waarbij de invallende fotonen een interactie aangaan met de moleculen van de stof, waardoor deze in een hogere trillingsmodus worden gebracht of een overgang naar een lagere trillingsmodus wordt geïnduceerd. Tijdens dit proces verliezen of winnen de fotonen energie van de analysemoleculen, waardoor de frequentie verandert. Een nauwkeurig onderzoek van het verstrooide licht kan de trillingsmodi onthullen, die nauw verband houden met de chemische bindingen van de molecule. Het is echter een relatief zwak proces, met een verstrooiingsdoorsnede die ordes van grootte kleiner is dan die van absorptie en fluorescentie. Gewoonlijk wordt het ramansignaal van een stof opgewekt door er een pomplaser op te richten met behulp van vrije-ruimteoptiek, waarbij de detectie beperkt blijft tot het focusvolume. De signaalintensiteit van ramanspectroscopie kan aanzienlijk worden verbeterd met behulp van een fotonische geïntegreerde schakeling (PIC). Vergeleken met vrije-ruimteoptiek hebben fotonische golfgeleiders een sterk elektrisch veld in de evanescente staart van geleide modi en een uitgebreider interactievolume. Op deze manier kunnen de prestaties van confocale ramanmicroscopen met ordes van grootte overtroffen worden. Bovendien is het uiteindelijke systeem veel compacter.

In de Photonics Research Group van de Universiteit Gent en IMEC hebben we verschillende on-chip benaderingen voor ramanspectroscopie onderzocht, waaronder *waveguide-enhanced Raman spectroscopy* (WERS), *surface-enhanced Raman spectroscopy* (SERS), en gestimuleerde ramanspectroscopie. Er zijn verschillende bouwblokken ontwikkeld geworden, waaronder diëlektrische golfgeleiders, plasmonische golfgeleiders, filters met roosterondersteuning en geïntegreerde fouriertransformatiespectrometers. Met de relevante componenten kan een on-chip ramansensor worden geassembleerd. In dit doctoraal werk streven we ernaar de totale detectiegrens van de on-chip ramansensor met ten minste een factor 10 te verbeteren om veeleisender toepassingen mogelijk te maken, zoals bewaking van de waterkwaliteit, bloedanalyse en detectie van chemische stoffen. Dit vereist nieuwe ontwerpen van de relevante bouwblokken en de systeemarchitectuur. Dit proefschrift onder-

zoekt dit vanuit vier aspecten: het golfgeleidermateriaal en -ontwerp, de verdichting van de te analyseren stof, een efficiëntere licht koppeling van laserpomp naar chip en een gedeeltelijk geïntegreerde spectrometer.

In WERS wordt het ramansignaal geëxciteerd en verzameld via het evanescente veld van golfgeleidermodi die overlappen met te analyseren stof in de mantel. Jammer genoeg genereert het elektrische veld in de golfgeleiderkern een breedbandig signaal dat bepaald wordt door de eigenschappen van het kernmateriaal, namelijk de ramanachtergrond. Dit veroorzaakt extra ruis en vermindert de signaal-ruisverhouding. Golfgeleidermaterialen met een lagere ramanachtergrond verdienen de voorkeur. Niettemin verdient het ook de voorkeur een golfgeleider met een hoog indexcontrast te kiezen, aangezien de discontinuïteit bij materiaalinterfaces het evanescente veld versterkt. Uit de vergelijking van verschillende golfgeleiderplatforms door Raza *et al.* (*Opt. Express* 2019) blijkt dat siliciumnitride (Si_3N_4) en tantaalpentoxide (Ta_2O_5) een goed evenwicht vertonen tussen indexcontrast en ramanachtergrondintensiteit. De brekingsindex van Ta_2O_5 (n=2.11) is iets hoger dan die van Si_3N_4 (n=1.89), hetgeen kan leiden tot een sterker ramansignaal. De signaalintensiteit kan verder worden verhoogd door het golfgeleiderontwerp te optimaliseren. Sleufgolfgeleiders bijvoorbeeld, sluiten het grootste deel van het elektrische veld in de mantel in. Ik heb de prestaties van een reeks Ta_2O_5-sleufgolfgeleiders numeriek geëvalueerd door de specifieke omzettingsefficiëntie η_0 te onderzoeken. De sleufbreedte is gevarieerd van 40 nm tot 150 nm. Het optimale ontwerp kan beter presteren dan Si_3N_4 golfgeleiders met een 150-nm brede sleuf met een factor 5.1. In samenwerking met het team van Prof. Blumenthal van de Universiteit van Californië, Santa Barbara, fabriceerden wij 400-nm hoge Ta_2O_5-sleufgolfgeleiders met behulp van elektronenbundellithografie (EBL). Vervolgens heb ik de golfgeleiders getest met ethanol als modelanalyt. Het ramansignaal is gemeten op de Ta_2O_5 golfgeleiders en een Si_3N_4 slot golfgeleider ter vergelijking. De signaalintensiteit is 4.8-maal zo hoog als in de optimale Ta_2O_5 golfgeleider, zoals blijkt uit figuur 1. De gemeten verbetering komt ongeveer overeen met de simulatie. Echter, beperkt door het etsproces is aanzienlijke over-etsing onvermijdelijk, resulterend in een tamelijk extreme aspectverhouding van de smalle golfgeleiders. Dit beïnvloedt de mechanische robuustheid van de golfgeleiders, vooral bij vloeistofdetectie. Smalle golfgeleiders van Ta_2O_5 kunnen een veelbelovend alternatief zijn voor Si_3N_4 golfgeleiders, zodra het etsproces is verbeterd en andere relevante componenten op het materiaalplatform zijn ontwikkeld.

Plaatselijke verdichting van de doelmoleculen kan de signaalintensiteit van verdunde analyten aanzienlijk verbeteren. Als de doelanalyt bekend is, kunnen we de detectielimiet verhogen door de golfgeleider te bekleden met een selectief adsorptiemiddel. Wij bestudeerden de prestaties van Si_3N_4-sleufgolfgeleiders gecoat met hexamethyldisilazaan (HMDS) gemodificeerd mesoporeus silica. Het sorptiemiddel werd gesynthetiseerd door de groep van Prof. Lendl van de Technische Universiteit van Wenen. Geholpen door de methylgroepen op poreuze oppervlakken die door HMDS zijn aangebracht, vertoont de mesoporeuze silicafilm een sterke

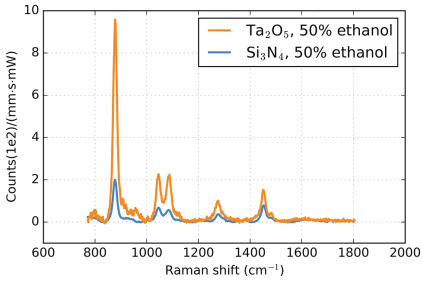

Figuur 1: Ramansignaal van ethanol, gemeten op respectievelijk Ta_2O_5 en Si_3N_4 sleufgolfgeleiders.

hydrofobiciteit. Het heeft een hogere affiniteit voor hydrofobe moleculen dan voor hydrofiele. Daarom kan het hydrofobe analyten uit waterige oplossingen verdichten, wat gebruikelijk is bij waterkwaliteitscontrole. Wij gebruikten cyclohexanon als een gemodificeerde analyt voor een hydrofoob oplosmiddel dat in de industrie wordt gebruikt. Met de gefunctionaliseerde golfgeleiders hebben wij een duidelijk ramansignaal aangetoond van cyclohexanon uit zijn waterige oplossing met een concentratie van 0.97 mM, zoals getoond in figuur 2. Met de huidige configuratie kan de detectiegrens van cyclohexanon het niveau van 10-μM bereiken. Multiplexdetectie met een andere hydrofobe analyt - 1-indanon - werd gedemonstreerd met een goede gevoeligheid voor beide analyten. Herhaalde desorptietests bewijzen de duurzaamheid en herbruikbaarheid van de gefunctionaliseerde golfgeleider. Verdichting van andere analyten kan worden gerealiseerd door de oppervlakte-eigenschappen van de mesoporeuze silica dienovereenkomstig te wijzigen.

Momenteel wordt de excitatie van het ramansignaal gerealiseerd vanuit vrijstaande lasers die via randkoppelaars gekoppeld worden in de diëlektrische golfgeleiders. Hoewel deze koppelstructuren een grote bandbreedte hebben en goed bestand zijn tegen fabricagevariaties, hebben ze een laag koppelingsrendement (-7 dB/facet) en zijn zij gevoelig voor onnauwkeurige optische uitlijning. Van roosterkoppelingen is bekend dat zij beter bestand zijn tegen verkeerde uitlijning, vooral wanneer zij worden ondersteund door microlenzen. Hun koppelingsefficiëntie kan aanzienlijk worden verhoogd door een bodemreflector op te nemen in de structuur. Bodemreflectoren zijn echter niet standaard bij de massaproductie van PIC's met behulp van mature platforms. Dit verhoogt de kosten en de fabricagetijd. Wij hebben een micro-transfer-printed (μTP) Si_3N_4 roosterkoppelaar voorgesteld, waarbij het diffractierooster en de bodemreflector in een latere fabricagefase op een doelcircuit worden geprint. De dwarsdoorsnede en het bovenaanzicht zijn geschetst in figuur 3. Licht wordt met hoge efficiëntie door het reflectorondersteunde rooster gekoppeld in de bovenste golfgeleiderlaag. Vervolgens wordt het van de roosterlaag naar de

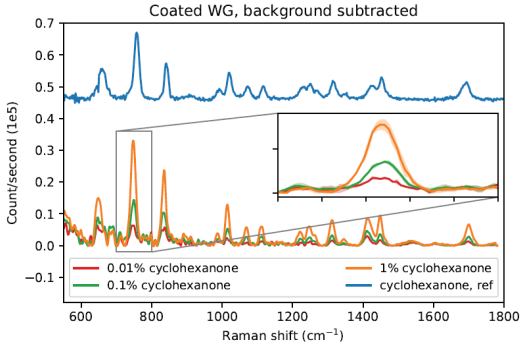

Figuur 2: Ramansignaal van cyclohexanon met verschillende volumeconcentraties in water, gemeten met behulp van een Si_3N_4 sleufgolfgeleider gefunctionaliseerd door HMDS-gemodificeerd mesoporeus silica. De volumeconcentratie van 0.01% komt overeen met 0.97 mM.

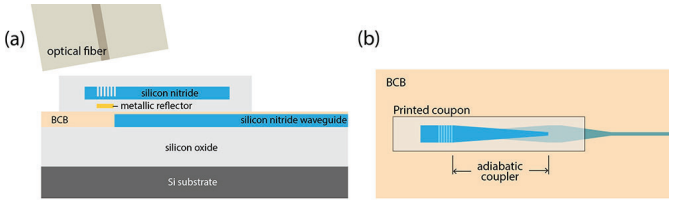

Figuur 3: Structuur van de Si_3N_4 grating coupler. (a) Dwarsdoorsnede. (b) bovenaanzicht.

onderste golfgeleiderlaag gekoppeld via een adiabatische koppelaar van 150 μm lang. Deze biedt een betere tolerantie voor verkeerde uitlijning en variaties in vergelijking met directionele koppelaars. De totale koppelingsefficiëntie van optische vezel naar het doelcircuit kan -1 dB bereiken in tweedimensionale FDTD-simulaties. De component werd vervaardigd in de cleanroom van de Universiteit Gent. In onze metingen bereikt de koppelingsefficiëntie -2 dB rond de golflengte van 840 nm, zoals getoond in figuur 4. Vergeleken met randkoppelingen kan de roosterkoppeling de signaalintensiteit met een factor 3 verhogen bij hetzelfde laservermogen.

Gevoelige, gekoelde spectrometers zijn vaak nodig om de bijzonder zwakke ramansignalen te detecteren. De omvang van dergelijke spectrometers staat verdere miniaturisering van het systeem in de weg. In dit werk hebben wij hebben de tweedimensionale optische *phased array* (OPA) gebruikt, bestaande uit golfgeleiders en roosterkoppelingen, voorgesteld door Karel Van Acoleyen *et al.* (*IEEE Photon.*

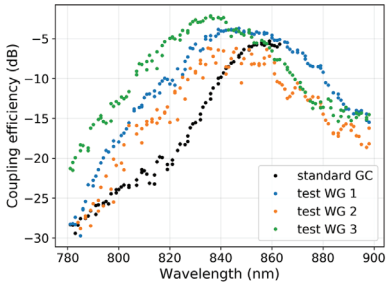

Figuur 4: Koppelingsefficiëntie per poort gemeten op drie golfgeleiders met μTP roosterkoppelingen en één golfgeleider met standaard uniforme roosterkoppelingen.

Technol. Lett. 2011). Licht wordt in een reeks golfgeleiders gesplitst via een sterkoppelaar. De golfgeleiders hebben stelselmatig grotere lengtes die een vaste fasevertraging introduceren tussen aangrenzende golfgeleiders. Aan het einde van elke golfgeleider wordt het licht door een roosterkoppelaar naar boven gebroken, waardoor een reeks bundels met vast (maar golflengteafhankelijk) fazeverband wordt gevormd. Daardoor wordt de globale bundel in twee orthogonale richtingen gestuurd naarmate de golflengte verandert. De ene wordt bepaald door de *phased array*, de andere door de fasematching van het rooster. We combineren de OPA op een Si_3N_4 PIC met een fourierbeeldvormingssysteem in de vrije ruimte, waarbij de quasi-parallelle bundel wordt afgebeeld op een punt op een beeldsensor. De coördinaat van het punt komt overeen met de richting van de bundel. Uit deze coördinaat kunnen we dus de golflengte van de input afleiden. De spectrometer wordt compacter. Bovendien wordt het handig om een standaard beeldsensor in de PIC te integreren. De PIC met detectiegolfgeleiders moet bij omgevingstemperatuur worden gehouden voor onze doeltoepassingen. Aangezien de beeldsensor ruimtelijk gescheiden is van de PIC, is het mogelijk om een gekoelde beeldsensor in het systeem te integreren. Wij hebben de OPA vervaardigd op een Si_3N_4-platform en getest met een fourierbeeldvormingsopstelling. Een breedbandig testsignaal wordt met succes gereconstrueerd uit het opgenomen beeld, zoals getoond in figuur 5. De spectrale resolutie bedraagt 0.5 nm in het spectrale bereik van 750–850 nm. Dit spectrale bereik wordt beperkt door onze afstembare laser die bij de kalibratie wordt gebruikt. Theoretisch is het spectrale bereik meer dan 200 nm breed.

Samengevat heb ik verschillende aspecten van een WERS-sensor onderzocht om een sterk verbeterde detectielimiet aan te tonen. Door de bovengenoemde componenten te optimaliseren, kunnen we de gevoeligheid met minstens een factor 15 verbeteren en de omvang van de WERS-sensor verkleinen. Dit werk brengt ons dichter bij een gevoelige, compacte, robuuste en kostenefficiënte ramansensor.

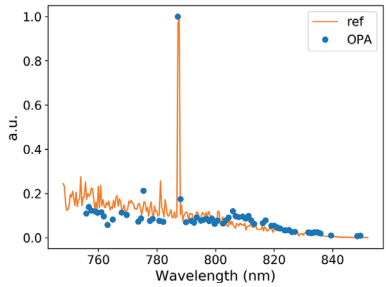

Figuur 5: De spectra gemeten met respectievelijk een Si_3N_4 OPA en een Fourier-space imaging opstelling (blauw) en met een commerciële optische spectrum analyzer (oranje).

Summary

In various fields, including chemistry, biology, and pharmaceutics, there is a tremendous need for rapid and accurate detection of chemical compositions. Especially multiplexed sensing in complex environments remains challenging with current methods. Raman spectroscopy offers label-free, unambiguous identification of chemical compositions. It utilizes Raman scattering, where the incident photons interact with analyte molecules, exciting them to a higher vibrational mode or inducing a transition to a lower vibrational mode. In this process, the photons lose or gain energy from the analyte molecules, resulting in a frequency change. A close examination of the scattered light can reveal the vibrational modes, which are closely related to the molecule's chemical bonds. However, it is a relatively weak process, with a scattering cross-section orders of magnitude smaller than absorption and fluorescence. Conventionally, the Raman signal of an analyte is excited by focusing a pump laser onto it using free-space optics, where the detection is limited to the focus volume. The signal intensity of Raman spectroscopy can be significantly enhanced using a photonic integrated circuit (PIC). Compared to free-space optics, photonic waveguides have a strong electric field in the evanescent tail of fundamental modes and a more extended interaction volume. As a much smaller system, it can outperform confocal Raman microscopes by orders of magnitude.

In the Photonics Research Group of Ghent University and IMEC, we have explored several on-chip approaches for Raman spectroscopy, including waveguide-enhanced Raman spectroscopy (WERS), surface-enhanced Raman spectroscopy, and stimulated Raman spectroscopy. Various components were developed, including dielectric waveguides, plasmonic waveguides, grating-assisted filters, and integrated Fourier transform spectrometers. An on-chip Raman sensor can be assembled using the relevant components. We aim to improve the overall detection limit of the on-chip Raman sensor by at least a factor of 10 to facilitate more demanding applications, such as water quality monitoring, blood analysis, and trace chemical detection. It requires novel designs of the relevant components and the system architecture. This thesis explores it from four aspects: the waveguide material and design, the analyte enrichment, more efficient coupling, and a partly integrated spectrometer.

In WERS, the Raman signal is excited and collected through the evanescent field of waveguide modes that overlap with the cladding. Meanwhile, the electric

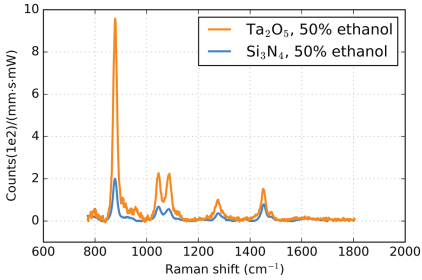

Figure 6: Raman signal of ethanol, measured on Ta_2O_5 and Si_3N_4 slot waveguides, respectively.

field in the waveguide core generates a broadband signal determined by core material properties, namely the Raman background. It induces extra noise and decreases the signal-to-noise ratio. Waveguide materials with lower Raman background are preferable. Nevertheless, it is also preferable to choose a waveguide platform with high index contrast, as the discontinuity at material interfaces enhances the evanescent field. From the comparison of several waveguide platforms by Raza *et al.* (*Opt. Express* 2019), silicon nitride (Si_3N_4) and tantalum pentoxide (Ta_2O_5) are found to exhibit a good balance between index contrast and Raman background intensity. The refractive index of Ta_2O_5 (n=2.11) is slightly higher than that of Si_3N_4 (n=1.89), which can lead to a stronger Raman signal. The signal intensity can be further boosted by optimizing the waveguide design. For instance, slot waveguides confine most of the electric field in the cladding. I numerically evaluated the performance of a series of Ta_2O_5 slot waveguides by examining the specific conversion efficiency η_0. The slot width is varied from 40 nm to 150 nm. The optimal design can outperform Si_3N_4 slot waveguides with a 150-nm wide slot by a factor of 5.1. In collaboration with the team of Prof. Blumenthal of University of California, Santa Barbara, we fabricated 400-nm high Ta_2O_5 slot waveguides using electron beam lithography (EBL). I then tested the waveguides using ethanol as a modal analyte. The Raman signal is measured on the Ta_2O_5 waveguides and a Si_3N_4 slot waveguide for comparison. The signal intensity is 4.8-fold stronger on the optimal Ta_2O_5 waveguide, as shown in Figure 6. The measured improvement roughly matches the simulation. However, limited by the etching process, significant over-etching is inevitable, resulting in a rather extreme aspect ratio of the narrow waveguides. It affects the durability of the waveguides, especially in liquid sensing. Ta_2O_5 narrow slot waveguides can be promising alternatives to Si_3N_4 slot waveguides as soon as the etching process is improved and other relevant components are developed on the material platform.

Locally enriching the target molecules can significantly improve the signal

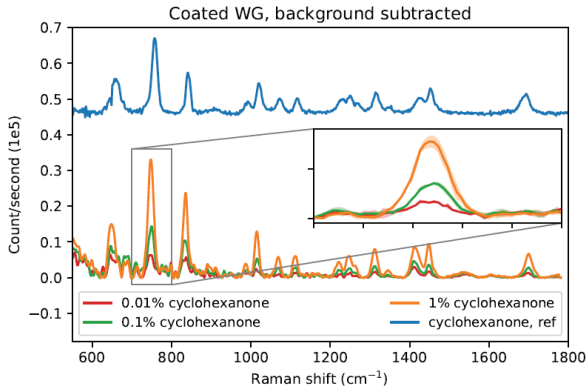

Figure 7: Raman signal of cyclohexanone with different volume concentrations in water measured using a Si_3N_4 slot waveguide functionalized by HMDS-modified mesoporous silica. The volume concentration of 0.01% corresponds to 0.97 mM.

intensity of dilute analytes. If the target analyte is known, we can boost the detection limit by coating the waveguide with a selective adsorbent. We studied the performance of Si_3N_4 slot waveguides coated by hexamethyldisilazane (HMDS) modified mesoporous silica. The sorbent cladding was synthesized by the group of Prof. Lendl of Vienna University of Technology. Assisted by the methyl groups on porous surfaces introduced by HMDS, the mesoporous silica film exhibits strong hydrophobicity. It has a higher affinity to hydrophobic molecules than hydrophilic ones. Hence it can enrich trace hydrophobic analytes from aqueous solutions, which is common in water quality monitoring. We employed cyclohexanone as a moded analyte for a hydrophobic solvent used in industry. Using the functionalized waveguides, we demonstrated a distinct Raman signal of cyclohexanone from its aqueous solution with a concentration of 0.97 mM, as shown in Figure 7. With the current configuration, the detection limit of cyclohexanone can reach the 10-μM level. Multiplexed detection with another hydrophobic analyte - 1-indanone - was demonstrated with good sensitivity for both analytes. Repeated desorption tests prove the durability and reusability of the functionalized waveguide. Enrichment of other analytes can be realized by modifying the surface properties of the mesoporous silica accordingly.

Currently, the excitation of the Raman signal is coupled from free-standing lasers into the dielectric waveguides through edge couplers. Although having broad bandwidth and good tolerance to fabrication variations, the edge couplers have low coupling efficiency (-7 dB/facet) and are sensitive to optical alignment. Grating couplers are known to be more tolerant of misalignment, especially when assisted

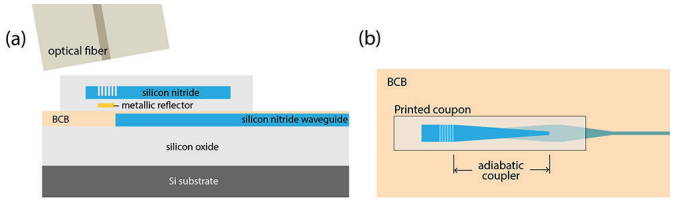

Figure 8: Structure of the μTP Si_3N_4 grating coupler. (a) Cross-section. (b) Top view.

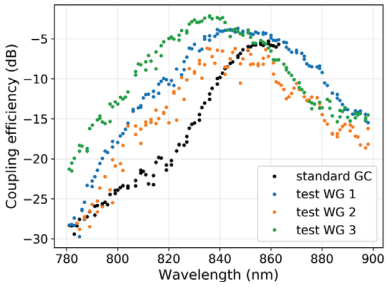

Figure 9: Coupling efficiencies per port measured on three waveguides with μTP grating couplers and one waveguide with standard uniform grating couplers.

with micro-lenses. Their coupling efficiency can be considerably increased by including a bottom reflector. However, bottom reflectors are not standard in the mass production of PICs using mature platforms. It will increase the cost and time of fabrication. We proposed a micro-transfer-printed (μTP) Si_3N_4 grating coupler, where the diffraction grating and the bottom reflector are printed onto a target circuit in a later fabrication stage. The cross-section and top view are sketched in Figure 8. Light is coupled through the reflector-assisted grating with high efficiency. Then it is coupled from the grating layer to the bottom waveguide layer through an adiabatic coupler, 150 μm long. It offers better tolerance to misalignment and variations compared to directional couplers. The overall coupling efficiency from optical fiber to the target circuit can reach -1 dB in two-dimensional FDTD simulations. The component was fabricated in the cleanroom of Ghent University. In our measurements, the coupling efficiency reaches -2 dB around the wavelength around 840 nm, as shown in Figure 9. Compared to edge couplers, the grating coupler can increase the signal intensity by a factor of 3 with the same laser power.

Sensitive, cooled spectrometers are often required to detect Raman signals due to their intrinsic weakness. The bulkiness of such spectrometers hinders further

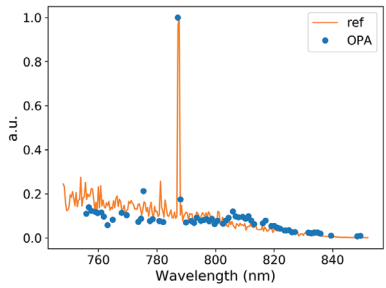

Figure 10: The spectra measured with a Si_3N_4 OPA and a Fourier-space imaging setup (blue) and with a commercial optical spectrum analyzer (orange), respectively.

miniaturization of the system. We adopted the two-dimensional optical phased array (OPA) consisting of arrayed waveguides and grating couplers, proposed by Karel Van Acoleyen *et al.* (*IEEE Photon. Technol. Lett.* 2011). Light is split into an array of waveguides through a star coupler. The waveguides have consecutively increased lengths that introduce a fixed phase delay between adjacent waveguides. At the end of each waveguide, a grating coupler diffracts the light upwards, forming a phased array. The diffracted beam is steered in two orthogonal directions as the wavelength changes. One is governed by the phased array, while the other is by the phase-matching condition of the grating. We combine the OPA on a Si_3N_4 PIC with a Fourier-space imaging system in free space, where the quasi-parallel beam is imaged onto a point on an image sensor. The coordinate of the point corresponds to the direction of the beam. Therefore, by examining the coordinate on the image sensor, we can deduce the wavelength of the input. The spectrometer becomes more compact. Moreover, it becomes convenient to integrate an off-the-shelf image sensor with the PIC. The PIC with sensing waveguides should be kept at ambient temperatures for our target applications. As the image sensor is spatially separated from the PIC, it is also convenient to integrate a cooled image sensor into the system. We fabricated the OPA on a Si_3N_4 platform and tested it with a Fourier-space imaging setup. A broadband test signal is successfully reconstructed from the captured image, as shown in Figure 10. The spectral resolution reaches 0.5 nm in the spectral range of 750–850 nm. This spectral range is set by our tunable laser used in calibration. Theoretically, the spectral range is beyond 200 nm wide.

In summary, I explored different aspects of a WERS sensor to demonstrate an unprecedented detection limit. By optimizing the aforementioned components, we can improve the sensitivity by at least a factor of 15 and reduce the size of the WERS sensor. This work brings us closer to a sensitive, compact, robust, and cost-efficient Raman sensor.

1 Introduction

1.1 Background and rationale

In various fields including chemistry, biology, and pharmaceutics, there is a tremendous need for the identification and quantification of chemical compositions. In certain cases, multiple analytes need to be detected simultaneously in complex environments, such as blood analysis and water quality monitoring. There is a myriad of techniques available, including affinity-based, spectroscopic, or optical sensing methods. The affinity-based methods, such as enzyme-linked immunosorbent assay (ELISA) and western blot, are widely performed with high throughput. But it is expensive and time-consuming to develop sensitive, well-characterized affinity ligands for the target analyte. The problem becomes more complicated when multiplexing is preferred. There is also a well-developed technique called liquid chromatography-mass spectroscopy (LC-MS) combining affinity-based separation and spectroscopic analysis. It can separate different chemical compositions based on their affinity to a certain adsorbent, offering accurate identification of compounds in complex mixtures. However, the instrumental complexity, size, and operation time limit the use of LC-MS to laboratory environments. Various types of miniaturized optical chemical sensors are also developed for such applications. Table 1.1 lists some main categories and examples from the literature. Optical signals can be generated from different mechanisms such as fluorescence, refractive

		Sensor platforms		
		Optical fibers	Waveguides	Plasmonics
Working principle	Fluorescence	[1, 2]	[3, 4]	[5, 6]
	Refractive index	[7–9]	[10–12]	[9, 11, 13]
	Absorption	[14, 15]	[16–18]	[19, 20]
	Raman	[21, 22]	[17, 23, 24]	[25–28]

Table 1.1: Main categories of optical chemical sensors and some examples from literature

index variations, absorption, and Raman scattering. In fluorescence sensing, the presence of an analyte can affect various aspects of the fluorescence generated by a fluorophore, such as intensity, lifetime, frequency, anisotropy, and so on. The species and quantity of the analyte can be determined by measuring the aforementioned parameters. Sensitive detection of various analytes has been demonstrated using optical fibers [1, 2], photonic waveguides [3, 4], or plasmonic structures [5, 6] to deliver the excitation. However, the performance depends strongly on the proper choice of fluorophores, which becomes more difficult in complex environments. A similar problem exists in refractive index sensing, where the presence of an analyte is probed from a change in the refractive index utilizing various principles [7–13]. The change in refractive index cannot be linked directly to a specific analyte without proper labeling or pre-treatment of samples. For fluorescence and refractive index sensing, the sensor needs to be characterized for each target analyte. In absorption spectroscopy, a tunable laser or broadband light source in the infrared and a spectrometer are required to measure the absorbance of the analyte at a series of wavelengths. Absorption occurs when the photon frequency matches one of the vibrational frequencies determined by molecular structures. From the absorbance spectrum, analytes can be identified with excellent specificity. It has been extensively explored for detecting gas and biomolecules on different platforms [14–20]. Although this label-free technique relaxes the requirement for sample preparation, the components it requires complicate the system. There is still a high demand for a simple, cost-efficient, and compact system with high throughput, especially for multiplexed detection.

Raman spectroscopy is a promising technique. It is based on an inelastic scattering process named Raman scattering, discovered by C. V. Raman and K. S. Krishnan in 1928. A pump laser with a fixed wavelength is required to excite the Raman signal spontaneously. It probes the vibrational modes of the analyte molecules, which are closely related to the chemical bonds. This label-free technique offers to identify and quantify compositions with excellent chemical specificity. Conventionally, it is realized using confocal Raman spectroscopy, where the pump is directly focused onto the analyte using free space optics. However, Raman scattering has a rather small scattering cross-section, resulting in an intrinsically

weak signal. The confocal Raman microscopes usually contain high-power lasers, bulky optics, and cooled spectrometers to detect the signal. The application in non-laboratory environments is limited as well as other sensing technologies. To bring this functionality outside the laboratories, there are preliminary works on the miniaturization of confocal Raman microscopes [29–31]. They are realized using miniaturized free space optics or optical fibers.

To further reduce the size and cost of a Raman system, various lab-on-a-chip approaches have been explored [32–34]. The Photonics Research Group of Ghent University and IMEC has pioneered the development of photonic-chip-based Raman spectroscopy. A range of waveguide-based modalities have been realized, such as waveguide-enhanced Raman spectroscopy (WERS) [35], surface-enhanced Raman spectroscopy (SERS) [36, 37], and stimulated Raman spectroscopy (SRS) [38]. It has been demonstrated that a silicon nitride waveguide can generate a Raman signal orders of magnitude stronger than confocal Raman microscopes [39]. However, due to the intrinsically small scattering cross-section, the signal intensity is still insufficient for more demanding applications. For instance, in water quality monitoring and blood analysis, it is common to look for analytes with a concentration below 100 mg/L.

Further improvement of photonic-chip-based Raman spectroscopy is required to fulfill the requirements of such applications. We choose to proceed with WERS. In this approach, the Raman signal is enhanced by the strong evanescent field and extended interaction volume of a dielectric waveguide. Compared to SERS, WERS is more tolerable to high pump power, easier in fabrication, and does not suffer from metal absorption. As discussed by A. Raza in his thesis [40], SERS and WERS have similar performance in bulk sensing given the same pump power. Therefore, with higher pump power, WERS is expected to outperform SERS by at least a factor of 10. Meanwhile, the system of WERS is much simpler than SRS. Overall, a WERS sensor can achieve a good balance among signal intensity, system complexity, and fabrication compatibility.

The over-arching goal of this thesis is to realize an integrated Raman sensor with an unprecedented detection limit. It requires novel approaches in the design of all components of the photonic chip. In this thesis, we explore the detection limit of WERS by targeting the following four objectives:

- Explore more performant waveguide platforms and designs. Improve the detection limit by a factor of 4–5.
- Locally enrich the analyte selectively. Improve the detection limit by a factor up to 600.
- Reduce the coupling loss at the input and output of the photonic chip. Improve

the detection limit by a factor of 2–3.

- Develop an integrated spectrometer with a resolution of at least 1 nm over a bandwidth of 100 nm.

Combining these improvements into an integrated system, we can realize a compact, low-cost, sensitive, and selective Raman sensor. A more detailed overview of the content is included in the following section.

1.2 Thesis outline

In **Chapter 2**, we briefly go through the basic principle of Raman scattering and WERS. First, I present the selection rule and scattering cross-section of spontaneous Raman scattering. Next, by approximating an emitting molecule to an oscillating dipole, I calculate the Raman conversion efficiency of WERS and compare it to confocal Raman spectroscopy. Then, I give an overview of the Raman background of the waveguide core, an important feature in WERS. Finally, I list the relevant components of a WERS system.

In **Chapter 3**, I present a comparison of different waveguides and a systematic study of tantalum pentoxide slot waveguides. I first compare the refractive index and Raman background of different waveguide materials based on previous studies. Then different waveguide designs are compared for evanescent sensing. Afterward, the performance of a series of tantalum pentoxide slot waveguides is evaluated numerically and experimentally. As expected, it delivers a stronger Raman signal than silicon nitride waveguides.

In **Chapter 4**, I study selective local enrichment of the analyte around silicon nitride waveguides. This section starts with an overview of the chosen sorbent: HMDS-modified mesoporous silica. After introducing the fabrication process of mesoporous-silica-cladded waveguides, I experimentally demonstrate a strong enrichment of non-polar analyte around the waveguide. Simultaneous detection of multiple analyte is also realized. Finally, the reusability of the cladded waveguide is proved by repeated desorption tests.

In **Chapter 5**, I demonstrate a micro-transfer-printed silicon nitride grating coupler. I first introduce the basics of micro-transfer-printing technology. Next, I show the structure, working principle, and numerically estimated coupling efficiency of the grating coupler. Then I present the fabrication process and discuss some problems encountered during process development. Finally, high coupling efficiency is experimentally obtained on a silicon nitride circuit.

In **Chapter 6**, I show a hybrid spectrometer based on an on-chip optical phased array and a free-space imaging setup. I first introduce the working principle of the integrated and free-space sections, respectively. Then the performance of this spectrometer is theoretically evaluated from two aspects: spectral resolution and spectral range. Next, it is experimentally tested by measuring a spectrum generated by a tunable laser and a broadband supercontinuum light source. It holds the potential of an integrated spectrometer with a small footprint, high resolution, and wide spectral range.

In **Chapter 7**, the last chapter of this thesis, I summarize the aforementioned sub-projects and discuss the prospect of the outcomes of this thesis.

1.3 Publications

This dissertation has led to the following list of publications in conferences and international peer-reviewed journals.

1.3.1 Publications in international journals

1. **Z. Liu**, H. Zhao, B. Baumgartner, B. Lendl, A. Stassen, A. Skirtach, N. Le Thomas, and R. Baets, "Ultra-sensitive slot-waveguide-enhanced Raman spectroscopy for aqueous solutions of non-polar compounds using a functionalized silicon nitride photonic integrated circuit," *Optics Letters* **46**(5), pp. 1153 (2021).

   I experimentally examined the performance of silicon nitride slot waveguides functionalized using HMDS-modified mesoporous silica.

2. X. Nie, N. Turk, Y. Li, **Z. Liu**, and R. Baets, "High extinction ratio on-chip pump-rejection filter based on cascaded grating-assisted contra-directional couplers in silicon nitride rib waveguides," *Optics Letters* **44**(9), pp. 2310 (2019).

   I participated in the design, fabrication, and measurement of the grating-assisted filters in the initial phase.

1.3.2 Publications in international conferences

1. **Z. Liu**, N. Le Thomas, and R. Baets, "On-chip silicon nitride, optical phased array as a broadband near-infrared spectrometer," in *Proceedings of SPIE:*

Integrated Optics: Devices, Materials, and Technologies XXVII, pp. 12424-14 (2023).

I designed, fabricated, and tested the on-chip spectrometer.

2. **Z. Liu**, G. Muliuk, J. Zhang, G. Roelkens, N. Le Thomas, and R. Baets, "Micro-transfer printed silicon nitride grating couplers for efficient on-chip light coupling," in *Proceedings of SPIE: Integrated Optics: Devices, Materials, and Technologies XXVI*, pp. 1200404 (2022).

   I designed, fabricated, and tested the micro-transfer-printed grating couplers.

3. **Z. Liu**, Q. Zhao, P. Shi, B. Mitchell, H. Zhao, N. Le Thomas, D. Blumenthal, and R. Baets, "Tantalum Pentoxide Slot Waveguides for Waveguide Enhanced Raman Spectroscopy," in *Proceedings of Conference on Lasers and Electro-Optics Europe*, pp. CH-6.2 (2021).

   I designed and tested the tantalum pentoxide slot waveguides.

4. N. Le Thomas, **Z. Liu**, C. Lin, H. Zhao, and R. Baets, "Raman on-chip: Current status and future tracks," in *Proceedings of SPIE: Integrated Optics: Devices, Materials, and Technologies XXV*, pp.1168908 (2021, invited).

   I helped review the section about analyte enrichment using mesoporous silica.

5. **Z. Liu**, H. Zhao, B. Baumgartner, B. Lendl, A. Skirtach, N. Le Thomas, and R. Baets, "Ultra-sensitive silicon nitride waveguide-enhanced Raman spectroscopy for aqueous solutions of organic compounds," in *Proceedings of Conference on Lasers and Electro-Optics*, pp. SF2N.6 (2020).

   I tested the performance of silicon nitride waveguides functionalized using mesoporous silica.

6. **Z. Liu**, H. Zhao, A. Raza, N. Le Thomas, and R. Baets, "On the Performance of Tantalum Pentoxide and Silicon Nitride Slot Waveguides for On-Chip Raman Spectroscopy," in *Proceedings of European Conference on Integrated Optics*, pp. W.Po1.26 (2019).

   I numerically evaluated the performance of tantalum pentoxide and silicon nitride slot waveguides.

7. X. Nie, N. Turk, **Z. Liu**, and R. Baets, "Grating assisted contra-directional filters with high rejection ratio in silicon nitride rib waveguides," in *Proceedings of European Conference on Integrated Optics*, pp. T.Po2.11 (2019).

   I participated in designing, fabricating, and measuring the on-chip filters in the initial phase.

2

Waveguide enhanced Raman spectroscopy

Raman spectroscopy is a label-free technique and can identify chemical compositions with excellent specificity. It probes the vibrational modes that are closely related to the chemical bonds of molecules. However, it suffers from an intrinsically small scattering cross-section, resulting in an extremely weak signal. Conventionally, a Raman system consists of a high-power laser, a confocal microscope, and a cooled spectrometer. It is widely used in laboratories in various fields. Nonetheless, the bulkiness has limited its application in non-laboratory environments. Various methods have been developed to minimize the system. Among these methods, waveguide-enhanced Raman spectroscopy (WERS) replaces confocal microscopes with a photonic waveguide. It excites and collects the Raman signal through the evanescent field of the mode propagating in the waveguide. With a strong electric field at the material interfaces and an extended interaction volume, the signal is significantly enhanced compared to a confocal Raman microscope. WERS combines the specificity of Raman spectroscopy and the compactness of photonic integrated circuits (PICs). The cost of an on-chip Raman sensor can be reduced to a few euros in mass production. To further improve the detection limit of WERS, various relevant components are being studied. In this chapter, I briefly discuss the basics of Raman spectroscopy and the advantages of WERS. Then I quantify the efficiency of WERS and discuss the challenges. Lastly, I provide an overview of the structure

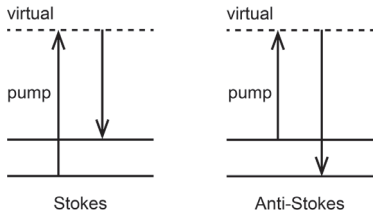

Figure 2.1: Energy level diagram of Stokes and anti-Stokes Raman scattering.

of a WERS sensor.

2.1 Basics of spontaneous Raman scattering

C. V. Raman and K. S. Krishnan discovered spontaneous Raman scattering in 1928. In Raman scattering, the light scattered from a medium contains frequencies different from the excitation. It is called Stokes scattering when the frequency decreases and anti-Stokes when it increases compared to the pump frequency. As shown in the simplified energy diagram of a molecule in Figure 2.1, the Raman Stokes scattering involves a transition from the ground state to a higher vibrational state through an intermediate virtual state. On the contrary, the Raman anti-Stokes scattering consists of transitioning from a higher vibrational state to the ground state through a virtual state. In thermal equilibrium, the population in the ground state is more than in the higher vibrational state. Therefore, the intensity of Stokes scattering is much stronger than the anti-Stokes scattering under thermal equilibrium. It is worth noting that if the pump had higher energy, the molecule could be excited to a higher electronic state, where the lifetime is longer, and fluorescence can be generated. Fluorescence is much stronger than Raman scattering as a resonant phenomenon, shadowing the Raman signal of analytes. Therefore, the pump wavelength of Raman spectroscopy should be long enough to avoid fluorescence.

The higher vibrational state corresponds to a higher vibrational energy of the molecule. Vibrations of the molecule can be described by its internal degrees of freedom. Considering the motion in the x, y, and z directions of all atoms in the molecule, there are $3n$ degrees of freedom in total, where n is the number of atoms in the molecule. Among them, three describe translations that do not change the relative position of atoms. For non-linear molecules, such as H_2O, there are three rotations around x, y, and z axes. Therefore, the remaining degrees of freedom for vibrational modes is $3n - 6$. For linear molecules, such as H_2 and CO_2, the

rotation around its own axes does not count as a rotational mode. It leaves $3n-5$ degrees of freedom for vibrational modes. However, not all of the vibrational modes are Raman-active. It can be understood through the classic model of light-matter interaction.

From a classic point of view, light-matter interaction is often treated as the interaction between an electromagnetic (EM) field and a dipole. The incidence EM field **E** drives the dipole oscillation, resulting in an induced dipole moment **p**:

$$\mathbf{p} = \alpha \mathbf{E}. \tag{2.1}$$

where α is polarizability. The polarizability α depends on the distribution of charges in the molecule, which is closely related to the chemical bonds. α can be Taylor expanded around its static value α_0 at equilibrium position as:

$$\alpha = \alpha_0 + \sum_i \left(\frac{\partial \alpha}{\partial Q_i} \right) Q_i + \cdots \tag{2.2}$$

where Q_i represents the normal coordinate of a vibrational mode i. If the normal coordinate at the equilibrium position for the mode Q_i is noted as Q_0^i, the normal coordinate Q_i can be written as:

$$Q_i = Q_0^i \cos(\omega_i t) \tag{2.3}$$

where ω_i is the corresponding frequency. Taking the first two terms of eq. (2.2) into the induced dipole moment **p**, it becomes

$$\mathbf{p} = \alpha_0 \mathbf{E}_0 \cos(\omega_0 t) + \mathbf{E}_0 \sum_i \left(\frac{\partial \alpha}{\partial Q_i} \right) Q_0^i \{ \cos[(\omega_0 - \omega_i) t]] + \cos[(\omega_0 + \omega_i) t] \} \tag{2.4}$$

which is a superposition of three frequencies corresponding to the incidence, the Stokes scattering, and the anti-Stokes scattering. Only the vibrational modes fulfilling $\partial \alpha / \partial Q_i \neq 0$ can contribute to the radiation. In other words, only the vibrational modes that can change the polarizability are Raman-active, e.g. symmetric stretching. Other modes cannot be observed in Raman spectroscopy, e.g. unsymmetric stretching. However, as unsymmetric stretching changes the dipole moment, it is active in infrared (IR) spectroscopy. Comprehensive explanations of the principle of IR spectroscopy can be found in literature [41]. The two techniques can complementarily determine most chemical bonds in molecules.

In free space, the scattered power by a Raman-active mode is related to the incidence intensity I_0 as

$$P = \sigma_0 I_0 \tag{2.5}$$

where σ_0 is the scattering cross-section of the Raman mode with a unit of cm^2. It is related to molecular properties and the incidence wavelength λ_0 as

$$\sigma_0 = \frac{\pi^2 \alpha_i^2}{\epsilon_0^2 \lambda_0^4} \tag{2.6}$$

where α_i is the polarizability of the Raman mode. The cross-section of Raman scattering is rather small. For instance, the Raman scattering cross-section of a dye rhodamine 6G (R6G) is around 2×10^{-27} cm^2 with a pump wavelength of 785 nm [42]. As a comparison, the fluorescence cross-section of R6G is at the level of 2×10^{-16} cm^2 [42].

As shown in eq. (2.6), a shorter pump wavelength can significantly increase the Raman scattering cross-section σ_0. However, a short wavelength can also induce strong fluorescence, orders of magnitude stronger than Raman scattering. Meanwhile, for biological and pharmaceutical applications, it is preferable to avoid the strong absorption of water and hemoglobin in ultra-violet (UV) and IR range [43]. Therefore, we choose the pump wavelength to be 785 nm, which excites a moderate Raman signal, induces limited fluorescence, and falls in the near-infrared (NIR) absorption window.

2.2 Signal enhancement by dielectric waveguide

In confocal Raman microscopes, the excitation is usually focused onto the analyte through a microscope objective, as sketched in Figure 2.2. The excitation power is focused into a diffraction volume determined by the focus depth D and solid angle Ω. The conversion efficiency η_c from pump power P_{pump} to Stokes power P_S is given by:

$$\eta_c = \frac{P_S}{P_{pump}} = \Omega D \rho \sigma \tag{2.7}$$

where ρ is the molecular density of the analyte, and σ the differential scattering cross-section. σ is related to the scattering cross-section σ_0 as

$$\sigma = \frac{d\sigma_0}{d\Omega} \tag{2.8}$$

because the dipole emission is not uniform in all directions.

The beam propagating through the analyte is assumed to be Gaussian, with dimensions sketched in Figure 2.3. When the divergence angle θ_0 is small, it can be approximated to

$$\theta_0 \approx \frac{w(z)}{z} = w_0 \sqrt{\frac{1}{z^2} + \frac{1}{z_R^2}} \tag{2.9}$$

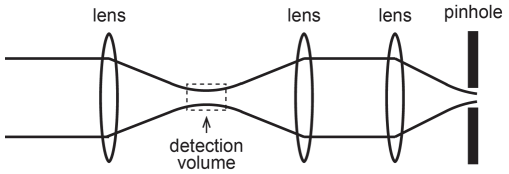

Figure 2.2: Sketch of the detection part of a confocal Raman microscope

where $w(z)$ is beam radius at the position z. z_R represents the Rayleigh range, where the beam radius reaches $\sqrt{2}$ times the beam waist w_0. It is related to the beam waist w_0 as

$$z_R = \frac{\pi n w_0^2}{\lambda} \tag{2.10}$$

where n is the refractive index of the analyte. The focus depth D is defined as

$$D = 2z_R \tag{2.11}$$

When the position z is large, the divergence angle θ_0 becomes

$$\lim_{z \to +\infty} \theta_0 = \frac{w_0}{z_R} \tag{2.12}$$

With a small divergence, the solid angle Ω is estimated as

$$\Omega \approx \pi \theta_0^2 = \pi \left(\frac{w_0}{z_R} \right)^2 = \frac{\lambda}{n z_R} \tag{2.13}$$

Putting eq. (2.11) and (2.13) into the conversion efficiency η_c, we arrive at

$$\eta_c = 2\rho\sigma \frac{\lambda_p}{n} \tag{2.14}$$

where λ_p is the pump wavelength. The efficiency of a diffraction-limited system only depends on the pump wavelength and analyte properties. There is little room for improvement in the optical system.

Dielectric waveguides have been explored as a better alternative to free-space optics in Raman spectroscopy [39]. The evanescent field of dielectric waveguides can interact with the cladding and excite the Raman signal. With high-index-contrast waveguides, the electric field is relatively strong at the interfaces between the waveguide and cladding. Also, the extended length of waveguides greatly improves the interaction volume between the pump and the analyte. A stronger Raman signal is excited. Meanwhile, the collection is more efficient as high-index-contrast waveguides can collect light from a wider angle, i.e., have a higher

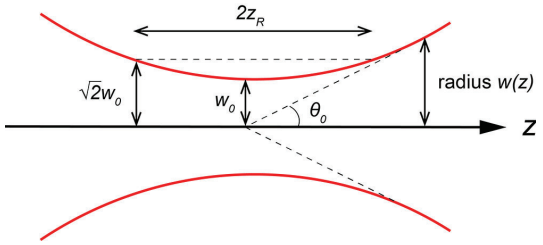

Figure 2.3: Sketch of a Gaussian beam propagating along the z-axis

numerical aperture (NA). The NA of a waveguide is usually defined as

$$NA = \sqrt{n_{core}^2 - n_{clad}^2} \tag{2.15}$$

which increases with the index contrast.

The conversion efficiency of WERS can be calculated by approximating an emitting molecule to an oscillating dipole. For a dipole in a homogeneous medium with a refractive index n, the spontaneous decay rate γ_0 is expressed as

$$\gamma_0 = \frac{n\omega^3|\mathbf{d}|^2}{3\pi\hbar\epsilon_0 c^3} \tag{2.16}$$

where ω is the angular emission frequency, and $\mathbf{d}$ the dipole moment [44]. In WERS, only the molecules relatively close to the waveguide can contribute to the Raman signal. The inhomogeneous local environment alters the spontaneous emission rate [45]. Part of the spontaneous emission is coupled to a waveguide mode. From Fermi's golden rule in the weak coupling regime, the spontaneous emission rate γ_{wg} near a waveguide is

$$\gamma_{wg} = \frac{2\pi}{\hbar^2}|g\left(\mathbf{r},\omega\right)|^2\rho\left(\omega\right) \tag{2.17}$$

where $g\left(\mathbf{r},\omega\right)$ is the coupling strength between the dipole and the EM field, and $\rho(\omega)$ the density of states. The coupling strength is given by

$$|g\left(\mathbf{r},\omega\right)|^2 = \xi^2|\mathbf{d}\cdot\mathbf{E}(\mathbf{r},\omega)|^2 \tag{2.18}$$

where ξ is an energy normalization constant that relates the emission frequency with the total energy density $\langle W_{EM}\rangle$. The latter is given by

$$\langle W_{EM}\rangle = \frac{\epsilon_0}{4}\frac{\partial\omega\epsilon\left(\mathbf{r},\omega\right)}{\partial\omega}|\mathbf{E}\left(\mathbf{r},\omega\right)|^2 + \frac{\mu_0}{4}|\mathbf{H}\left(\mathbf{r},\omega\right)|^2 \tag{2.19}$$

where μ_0 is the vacuum permeability. The total energy $\hbar\omega$ carried by a waveguide mode with angular frequency ω can be calculated by integrating the energy density $\langle W_{EM}\rangle$ over the entire waveguide cross-section as

$$\hbar\omega = 4L\xi^2 \iint \langle W_{EM}\rangle d\mathbf{r} \tag{2.20}$$

Therefore, the normalization constant ξ can be calculated as

$$\xi^2 = \frac{\hbar\omega}{4L\iint\langle W_{EM}\rangle d\mathbf{r}}. \tag{2.21}$$

Meanwhile, the density of states $\rho(\omega)$ can be given as

$$\rho(\omega) = \frac{L}{\pi v_g} \tag{2.22}$$

Combining eq. (2.17)–(2.22), the spontaneous emission rate γ_{wg} of a dipole positioned in a medium with refractive index n near a single-mode waveguide can be derived as

$$\gamma_{wg} = \frac{\omega|\mathbf{d}|^2}{\hbar v_g \epsilon_0 n^2 A_{eff}\left(\mathbf{r},\omega\right)} \tag{2.23}$$

where v_g and A_{eff} are the group velocity and effective area of a waveguide mode, respectively. The effective area A_{eff} can be derived from the electric field distribution in the medium with $n = \sqrt{\epsilon}$ as

$$A_{eff}(\mathbf{r}_0, w) = \frac{\iint \epsilon_0\epsilon\left(\mathbf{r}\right)|\mathbf{E}(\mathbf{r},w)|^2 d\mathbf{r}}{\epsilon_0\epsilon(\mathbf{r}_0)|\mathbf{e}_0\cdot\mathbf{E}(\mathbf{r}_0,w)|^2}. \tag{2.24}$$

The normalized spontaneous decay rate can be expressed as

$$\frac{\gamma_{wg}}{\gamma_0} = \frac{3}{4\pi}\frac{c\lambda^2}{n^3 v_g A_{eff}} = \frac{P_{wg,all}}{P_0}, \tag{2.25}$$

which equals the ratio of power coupled into a waveguide mode and the power $P_{wg,all}$ emitted in free-space P_0. The latter is given by

$$P_0 = \frac{4\pi^3 c|\mathbf{d}|^2}{3\epsilon_0\lambda_S^4} \tag{2.26}$$

where λ_S is the Stokes wavelength. And the molecule excited by the fundamental mode has a dipole moment $\mathbf{d}$ of

$$|\mathbf{d}|^2 = \alpha^2|\mathbf{e}_0\cdot\mathbf{E}\left(\mathbf{r}_0,\lambda_P\right)|^2\frac{n_g P_{pump}}{c\epsilon_0\iint\epsilon\left(\mathbf{r}\right)|\mathbf{E}\left(\mathbf{r},\lambda_P\right)|^2 d\mathbf{r}} \tag{2.27}$$

where α is the polarizability of the Raman mode, and λ_P the pump wavelength.

The power coupled to the waveguide mode can propagate in both directions. In practice, we only collect the Raman signal from one facet of the waveguide. Hence the power coupled into the forward propagation P_{wg} is given by

$$\frac{P_{wg}}{P_0} = \frac{1}{2}\frac{\gamma_{wg}}{\gamma_0} = \frac{3}{8\pi}\frac{n_g}{n}\left(\frac{\lambda}{n}\right)^2 \frac{\epsilon_0\epsilon(\mathbf{r}_0)|\mathbf{e}_0 \cdot \mathbf{E}\left(\mathbf{r}_0, w\right)|^2}{\iint \epsilon_0\epsilon(\mathbf{r})|\mathbf{E}(\mathbf{r}, w)|^2 d\mathbf{r}} \tag{2.28}$$

Using eq. (2.26) and eq. (2.27), one can derive that

$$\frac{P_{wg}(\mathbf{r}_0)}{P_{pump}} = \frac{\pi^2\alpha^2}{\epsilon_0^2\lambda_S^4}\frac{\eta(\mathbf{r}_0)}{2} = \frac{\sigma\eta(\mathbf{r}_0)}{2}, \tag{2.29}$$

where the conversion efficiency $\eta(\mathbf{r}_0)$ at the position $\mathbf{r}_0$ equals

$$\eta(\mathbf{r}_0) = n_g\left(\lambda_p\right) n_g\left(\lambda_s\right) \frac{\lambda_s^2}{n} \frac{|\mathbf{E}\left(\mathbf{r}_0, \lambda_p\right)|^2}{\iint \epsilon\left(\mathbf{r}\right)|\mathbf{E}\left(\mathbf{r}, \lambda_p\right)|^2 d\mathbf{r}} \frac{|\mathbf{E}\left(\mathbf{r}_0, \lambda_s\right)|^2}{\iint \epsilon\left(\mathbf{r}\right)|\mathbf{E}\left(\mathbf{r}, \lambda_s\right)|^2 d\mathbf{r}}. \tag{2.30}$$

The top cladding of a waveguide is filled with oscillating molecules with a molecular density ρ. On an arbitrary cross-section of the waveguide, the total power coupled to the waveguide is calculated as:

$$\frac{dP_{wg}}{P_{pump}} = \frac{\rho\sigma\eta_0}{2}dz \tag{2.31}$$

where the dimensionless parameter η_0 is

$$\eta_0 = \iint \eta\left(\mathbf{r}_0\right) \mathrm{d}\mathbf{r}_0. \tag{2.32}$$

The specific conversion efficiency η_0 only depends on the electric field distribution on waveguide cross-sections. It can be numerically evaluated in waveguide simulation tools such as Lumerical MODE solutions and Fimmwave. As an indicator of WERS performance of a waveguide, η_0 is exploited to compare different designs in the following chapter.

We must consider the propagation loss to evaluate the overall power collected from a dielectric waveguide. It mainly originates from surface roughness and absorption. The intensities of the pump and signal both decrease along propagation. As presented for instance by A. Raza [40], the overall power of backward propagating Raman signal can be calculated as

$$\begin{aligned} \frac{P_{wg}}{P_{pump}} &= \frac{1}{2}\rho\sigma\eta_0 \int_0^L e^{-\alpha_p z} e^{-\alpha_s L} dz \\ &= \frac{1}{2}\rho\sigma\eta_0 \left(\frac{1 - e^{-(\alpha_p+\alpha_s)L}}{\alpha_p + \alpha_s}\right), \end{aligned} \tag{2.33}$$

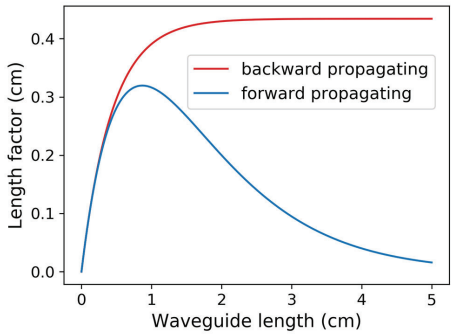

Figure 2.4: Length factor (LF) of forward and backward propagating Raman signals. The waveguide loss is assumed to be 5 dB/cm.

where L is the waveguide length, and α_p and α_s the loss coefficients (unit: cm^{-1}) at pump and Stokes wavelengths, respectively. Similarly, the overall power of forward propagating Raman signal is

$$\begin{aligned}\frac{P_{wg}}{P_{pump}} &= \frac{1}{2}\rho\sigma\eta_0 \int_0^L e^{-\alpha_p z} e^{-\alpha_s (L-z)} dz \\ &= \frac{1}{2}\rho\sigma\eta_0 e^{-\alpha_p L} \left(\frac{e^{(\alpha_p - \alpha_s)L} - 1}{\alpha_p - \alpha_s} \right) \approx \frac{1}{2}\rho\sigma\eta_0 e^{-\alpha_p L} L.\end{aligned} \tag{2.34}$$

The approximation stands when the difference between α_s and α_p is small. The last terms involving L in eq. (2.33) and (2.34) are called the length factors (LF). Assuming a waveguide loss of α_p=α_s=5 dB/cm, the length factors for both propagation directions are plotted in Figure 2.4. In the backward propagation regime, the derivative of the length factor rapidly approaches zero. For waveguides longer than an optimal length, the added interaction volume is counterweighed by the propagation loss back to the input facet. In the forward propagation regime, LF peaks at an optimal length of $L = 1/\alpha$, at which a balance is achieved between propagation loss and interaction volume. It is worth noting that the maximum LF is higher in backward propagation, as the Raman signal excited by the un attenuated pump is immediately collected at the input.

Comparing eq. (2.14) and eq. (2.33), the Raman signal generated by a dielectric waveguide is stronger than a confocal microscope by a factor of:

$$N = \frac{n\eta_0}{4} \frac{\mathrm{LF}}{\lambda_p}. \tag{2.35}$$

Typically, η_0 of Si_3N_4 strip waveguides is below 0.1. As plotted in Figure 2.4, LF can reach 0.4 cm, which is around 5×10^3 times larger than the pump wavelength of 785 nm. The enhancement factor N can be further improved by increasing the conversion efficiency η_0 and reducing the propagation loss of the waveguide.

2.3 Raman background: features and origin

Figure 2.5 shows typical Raman spectra of ethanol measured with a Si_3N_4 waveguide and a confocal microscope. The peak around 520 cm^{-1} in the Si_3N_4 signal is a signature of crystalline silicon. It is generated from light scattered from the silicon substrate. On top of the discrete peaks of ethanol, dielectric waveguides generate a broad background in the Raman signal. It is called the Raman background, which imposes extra shot noise on the Raman signal of the analyte and reduces the signal-to-noise ratio (SNR). Le Thomas *et al.* attributed the origin of Raman background to the fundamental thermodynamic fluctuations in amorphous waveguide materials [46]. These fluctuations cause thermorefractive phase noise to the optical signal. For higher frequencies, as relevant in Raman spectroscopy, the thermodynamic fluctuations should be considered spatially and temporally correlated. It results in an exponential decay in the optical spectrum as the frequency decreases, which agrees with the general shape of the Raman background of a Si_3N_4 waveguide. The correlation length and variance of those fluctuations are determined by waveguide material properties, such as composition and synthesis methods. Therefore, different waveguide platforms can introduce different Raman backgrounds. We need a waveguide material with a lower Raman background to ensure the optimal SNR. In the next chapter, we will compare the Raman background of several common waveguide materials.

2.4 Components in a WERS sensor

In the last section, I demonstrated the large enhancement factor N of WERS compared to confocal Raman microscopes. It is closely related to the conversion efficiency and the waveguide loss. Both factors are defined by the properties of the waveguide, including material, geometry, sidewall roughness, etc. It is safe to say that the waveguide is the core component of WERS. In this thesis, several waveguide materials and geometries are explored to identify the optimal design. We also tried to functionalize the waveguide to selectively enrich some analytes from the cladding.

Other components are required to form a complete on-chip system besides the

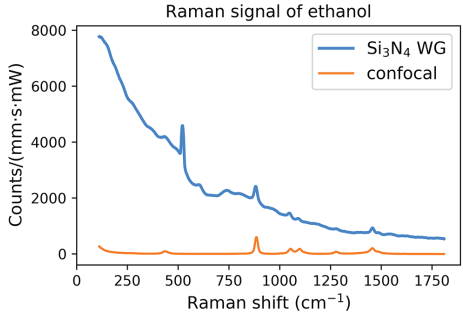

Figure 2.5: Raman signal of bulk ethanol measured with a Si_3N_4 waveguide (blue) and a confocal Raman microscope (orange), respectively. The peak at 520 cm^{-1} on the blue line is a characteristic peak of crystalline silicon. The intensity of the blue curve is doubled.

waveguide. First, a pump laser is essential. To generate adequate Raman signal spontaneously, the pump power should be higher than 1 mW and remains stable for at least one minute. Meanwhile, the linewidth should be narrow and the wavelength should not drift much over time. Currently, a 785 nm laser with narrow linewidth, moderate power, and good stability cannot be integrated on Si_3N_4 platforms. Hence a free-standing laser diode is still necessary. On-chip couplers are needed to couple the output of such a laser into the sensing waveguide. Due to the mismatch between the mode profiles of Si_3N_4 waveguides and single-mode optical fibers, the coupling efficiency of Si_3N_4 couplers is often limited. To ensure an efficient coupling from laser to waveguide, novel couplers should be developed.

Second, a spectrometer is also essential. Due to the intrinsic weakness of Raman signals, bulky benchtop spectrometers cooled to below -20°C are conventionally used for detection. There is still no on-chip alternative with comparable resolution, bandwidth, and noise level. In this thesis, I tried integrating part of the spectrometer on-chip to reduce the footprint while maintaining good performance.

Some additional functionalities may be needed in the system. For instance, a band-pass filter can reject the pump wavelength before the spectrometer. In spontaneous Raman scattering, the pump is over ten orders of magnitude stronger than the Raman signal. We risk severe saturation, blooming, or even damage to the image sensor of the spectrometer without a pump filter.

The goal of this study on WERS is to pave the way toward an integrated Raman sensor with an unprecedented detection limit and a robust system architecture. Therefore, we must explore the options and improve from all possible aspects. In

this thesis, we studied the sensing waveguide, the couplers, and the spectrometer and brought the performance of all three components to a new high. We are steps closer to a complete system for WERS.

2.5 Conclusion

In this chapter, I aim to provide an overview of WERS from principle to implementation. We first discussed the basic principle and selection rules of Raman scattering. Although a shorter pump wavelength can give rise to a larger scattering cross-section and subsequently a stronger Raman signal, it also risks undesirable fluorescence, orders of magnitude stronger than Raman signals. Therefore, we choose the pump wavelength of 785 nm, which avoids fluorescence and the absorption of water. Then, I compared the conversion efficiency from pump to signal of two types of collection systems: the free-space optics and the photonic waveguides. From theoretical evaluation, we found that the enhancement of Raman signal provided by the waveguide is higher by several orders of magnitude. The exact value is determined by waveguide properties, such as waveguide geometry, material, and propagation loss. However, the waveguide core material generates a broad background in the Raman signal, inducing extra shot noise. It is intrinsic to material properties. Lastly, I listed the relevant components in WERS besides the sensing waveguide. In this work, we aim to improve the overall performance of a WERS sensor from all possible aspects.

3

Waveguide materials and design

The sensing waveguide is at the core of an on-chip Raman sensor. It primarily defines the performance of the system. Much effort has been devoted to finding an optimal waveguide design for on-chip Raman spectroscopy. The electric field can be locally enhanced by introducing plasmonic structures, such as gold nanodome [47], gold antennas [26], and metal slot waveguides [48]. However, the patterning of these gold structures is not compatible with CMOS (complementary metal-oxide-semiconductor) processing. It involves incompatible metal and requires electron beam lithography or metal lift-off. It hinders the cost-efficient mass production of on-chip Raman sensors. Nonetheless, the pump power must not exceed 1 mW due to strong local enhancement and photodegradation of the analyte. The limited pump power prevents the plasmonic waveguides from generating a stronger signal than dielectric waveguides, which can easily withstand tens of milliwatts of pump power. Therefore, WERS with a suitable dielectric waveguide can generate a stronger Raman signal while being easier to fabricate.

Two main aspects of dielectric waveguides can be optimized: material and design. The former determines the Raman background and the refractive index, while the latter mainly affects the proportion of the electric field in the cladding. Using waveguide platforms with low Raman background and high index contrast is preferable. With a higher index contrast, the electric field at material interfaces is enhanced, and a stronger Raman signal of the cladding is generated. Silicon

nitride (Si_3N_4) has been widely used for WERS for its versatility and maturity [24, 35,49]. Other platforms with higher index contrast and lower Raman background are also being studied, such as tantalum pentoxide (Ta_2O_5). To exploit the potential of these high-index-contrast platforms, the waveguide geometry needs to be optimized to confine the electric field more in the cladding. In this chapter, I first compare the Raman background of several different waveguide materials. Then, the performance of difference waveguide designs is evaluated from their electric field distribution and specific conversion efficiency η_0. Finally, I present an experimental study of Ta_2O_5 slot waveguides for WERS.

3.1 Raman background of several candidate materials for WERS

The waveguides used in WERS should be transparent at the pump wavelength and tolerant to high optical intensities. Although the choice of pump wavelength varies from ultra-violet (UV) to near-infrared (NIR), we mainly consider the NIR range in this thesis. Additionally, the availability of other components on the platform, such as lasers, filters, and spectrometers, is convenient when building an integrated on-chip Raman sensor. The optimal material should also have high index contrast and low Raman background. On the one hand, higher index contrast enhances the intensity of the electric field at interfaces between waveguide and cladding. Despite the reduced volume of the evanescent field due to tighter confinement, the overall enhancement of the Raman signal is more substantial than a lower index contrast platform. On the other hand, different materials have different features and intensities in the Raman background, generating shot noise. A strong Raman background can compromise the SNR improvement from high index contrast. Choosing a platform that can balance the index contrast and Raman background is preferable.

Several platforms have been studied with respect to these two aspects by Raza *et al.* [50]. The study includes four waveguide materials, including aluminum oxide (Al_2O_3), Si_3N_4, Ta_2O_5 and titanium oxide (TiO_2). The Al_2O_3, Ta_2O_5, and TiO_2 layers were all deposited in sputtering systems. The Si_3N_4 was deposited by plasma enhanced chemical vapor deposition (PECVD). On each platform, the Raman conversion efficiency η_0 is numerically evaluated for strip waveguides with a range of widths and heights. The optimal widths and heights are listed in Table 3.1. The highest refractive index of TiO_2 gives rise to the highest η_0 and the strongest Raman signal.

But TiO_2 waveguides suffer from severe noise. The detection limit is deter-

Material	Refractive index	Optimal Geometry (nm^2)	Optimal η_0
Al_2O_3	1.60	525×1125	0.039
Si_3N_4	1.89	425×575	0.172
Ta_2O_5	2.11	275×500	0.266
TiO_2	2.33	250×350	0.375

Table 3.1: The refractive indices, optimal strip waveguide geometries, and optimal conversion efficiencies (η_0) of different waveguide platforms [50]

mined by not only the signal intensity but also the noise intensity. Many factors contribute to the noise, including the shot noise, readout noise, dark count, and the Raman background. The last term generates shot noise and fine features that may overshadow the Raman signal. As the Raman background origins from thermodynamic fluctuations, it depends on waveguide material properties [46]. It is measured under the same experimental condition for the four waveguide platforms, as presented in Figure 3.1. The intensities are normalized by waveguide lengths and coupling efficiencies. The shaded area represents the standard deviation among five measurements on the same waveguide platform. Note that the synthesis method of the waveguide material may prominently affect the Raman background. For instance, it has been observed that Si_3N_4 deposited via PECVD and low-pressure chemical vapor deposition (LPCVD) can generate different shapes in the Raman background. In this study, the Raman background of TiO_2 is eight times higher than that of Si_3N_4 and Ta_2O_5. It outweighs the improvement of η_0 and reduces the performance. Ta_2O_5 has similar background intensities as Si_3N_4, despite the prominent peak around 660 cm^{-1}. It is sometimes even lower than that of Si_3N_4 in high wavenumbers above 1000 cm^{-1}, where the "fingerprints" of various biological and pharmaceutical molecules appear. Si_3N_4 and Ta_2O_5 platforms are promising candidates for WERS for their excellent balance between index contrast and background intensity.

3.2 The optimal waveguide geometry

Various waveguide designs have been studied for evanescent sensing, including strip waveguides, slot waveguides [51–53], and subwavelength gratings [54–56]. The target is to confine the electric field in the cladding as strongly as possible while maintaining a relatively low propagation loss. The performance of the three structures has been studied by Kita *et al.* for Raman spectroscopy on the silicon-on-insulator (SOI) platform [57]. They defined a figure-of-merit (FOM) that involves the Raman signal intensity and the scattering loss. Compared to strip waveguides, slot waveguides can confine more electric field in the cladding. Compared to

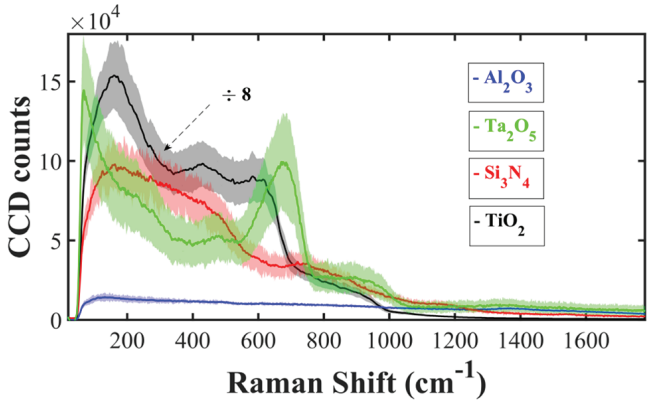

Figure 3.1: The Raman background measured from air-clad waveguides on different platforms [50]

subwavelength gratings, slot waveguides suffer less from the scattering loss from vertical sidewalls. From their numerical estimation, slot waveguides yield a higher FOM.

Similar conclusions apply to the Si_3N_4 platform. Figure 3.2 shows the simulated electric field (E-field) distribution on the cross-sections of Si_3N_4 strip and slot waveguides. None of the fundamental modes of the strip waveguide can confine more E-field in the cladding than the slot waveguide. The discontinuity of the E-field at high-index-contrast interfaces enhances the field in the slot, especially for the fundamental quasi-TE mode [58]. It has been demonstrated that a Si_3N_4 slot waveguide can generate an 8-fold greater Raman signal than a strip waveguide [35]. Regarding Si_3N_4 subwavelength gratings, simulations show less confinement in the cladding and more inside the waveguide material, which may lead to stronger Raman background. Slot waveguides offer stronger Raman signals and potentially better detection limit than strip waveguides and subwavelength gratings.

Currently, most studies of WERS are performed on Si_3N_4 platforms with either strip or slot waveguides. As discussed in the previous section, the Ta_2O_5 platform has higher index contrast and moderate Raman background. It is expected to deliver a stronger Raman signal than Si_3N_4, especially with slot waveguides. In the next section, I will compare Si_3N_4 and Ta_2O_5 slot waveguides numerically and experimentally.

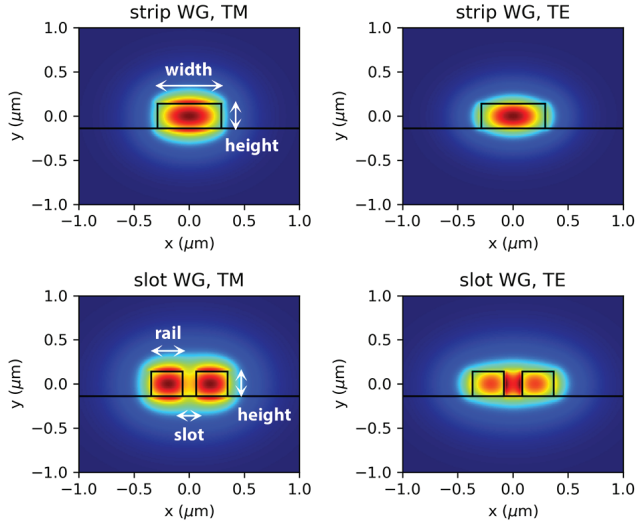

Figure 3.2: Electric field distribution of fundamental TE and TM modes on the cross-section of Si_3N_4 strip and slot waveguides

3.3 WERS performance of tantalum pentoxide slot waveguides

3.3.1 Numerical evaluation using conversion efficiency η_0

As discussed in the previous chapter, the power of Raman signal P_{wg} collected from the back-scattered light from a waveguide is given by

$$\frac{P_{wg}}{P_{pump}} = \frac{1}{2}\rho\sigma\gamma\eta_0 \mathrm{LF}, \tag{3.1}$$

where P_{pump} is the pump power, ρ the molecular density, σ the Raman scattering cross-section, and LF the length factor. The loss γ includes coupling loss, waveguide propagation loss, and losses in the spectrometer. The conversion efficiency η_0 can be estimated from the E-field distribution over the waveguide cross-section using eq. (2.32). Assuming that all waveguides have the same analyte and similar losses, a comparison of η_0 can predict the relative signal intensity of different geometries. In this section, we choose bulk ethanol as the modal analyte, which has a prominent peak at 880 cm^{-1}.

We simulated the E-field distribution over the cross-section of a series of slot waveguides using Lumerical MODE solutions. Figure 3.3 presents numerically estimated η_0 on Si_3N_4 and Ta_2O_5 platforms. We also consider two different thicknesses of the guiding layer: 300 nm and 400 nm. The optimal geometries and η_0 are listed in Table 3.2. It can be seen that the optimal η_0 increases with guiding layer thickness and index contrast. With 300 nm thickness, the optimal η_0 of Ta_2O_5 slot waveguides is 1.31, more than twice the value of Si_3N_4 slot waveguides (0.57). When the guiding layer thickness is 400 nm, the optimal η_0 raises to 1.33 and 0.63, respectively. With an increased waveguide thickness, the E-field is confined more in the waveguide and extends less into the bottom oxide cladding. The fraction of power confined in the slot area grows. However, if the rail width is kept the same, the fraction of power confined in the waveguide core also grows, faster than in the slot. It can be compensated by reducing the rail width. Therefore, the optimal geometry on a thicker guiding layer has narrower rail widths.

Comparison of Raman background intensity

I then try to put the contribution of Raman background into the evaluation of waveguides' performance. A stronger electric field in the waveguide core is assumed to induce a stronger Raman background. As the waveguide material and design change, the fraction of the E-field in the waveguide core also changes. This part of

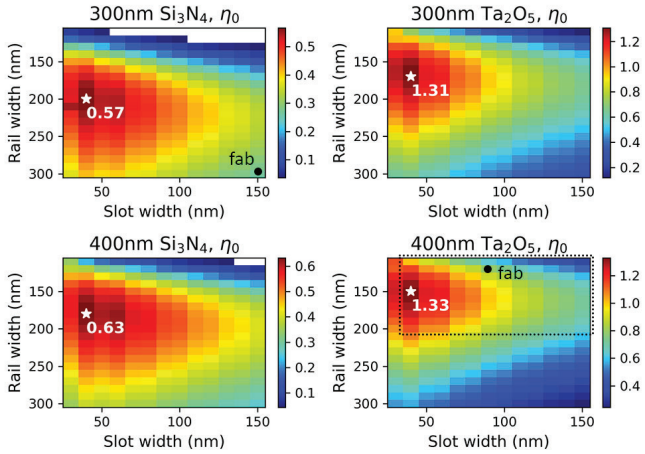

Figure 3.3: Simulated η_0 of Si_3N_4 and Ta_2O_5 slot waveguides.The optimal values are marked with a white star. The blank area in (a) and (c) has no fundamental TE mode. Dimensions of the fabricated Ta_2O_5 waveguides are marked with a dashed rectangle. The black dots represent the dimensions compared experimentally.

Material	Thickness (nm)	η_0	Rail (nm)	Slot (nm)
Si_3N_4	300	0.57	200	40
	400	0.63	180	40
Ta_2O_5	300	1.31	170	40
	400	1.33	150	40

Table 3.2: Optimal η_0 and geometries of Si_3N_4 and Ta_2O_5 slot waveguides from simulations

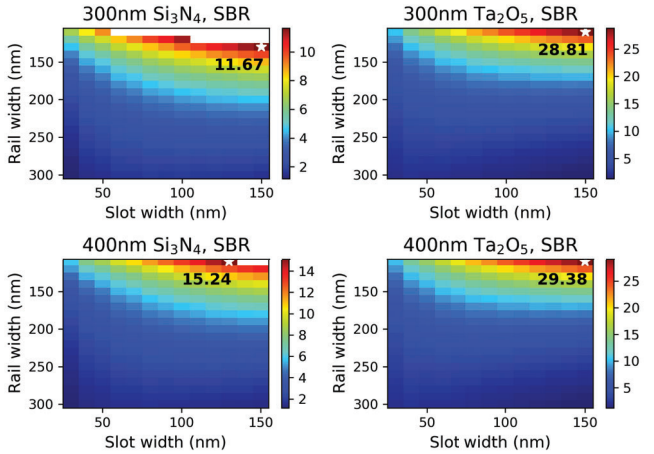

Figure 3.4: Simulated SBR of Si_3N_4 and Ta_2O_5 slot waveguides. The blank area in (a) and (c) has no fundamental TE mode.

the E-field excites the Raman background. By integrating equation (2.32) in the waveguide core instead of the top cladding, we obtain a conversion efficiency η_{bg} for the Raman background. To evaluate the signal and background intensities simultaneously, a figure-of-merit (FOM) is defined as the signal-to-background ratio (SBR), which is expressed as:

$$\mathrm{SBR} = \frac{\eta_0}{\eta_{\mathrm{bg}}}. \tag{3.2}$$

Note that this definition of SBR ignores the difference in the molecular density and the scattering cross-section between different compositions. It is a good indicator when comparing different designs on the same waveguide platform. When comparing different platforms, we must consider the measured intensity of the Raman background. The SBR of the same set of slot waveguides is plotted in Figure 3.4. It can be seen that waveguides with the widest slot and narrowest rails (on the top right corners) have the highest SBR. Although the E-field in the waveguide core is minimal, the E-field leaks to the oxide bottom cladding, introducing more propagation loss. It also introduces a background noise from silicon oxide.

In repeated measurements, we observe that the Raman background of a waveg-

uide is consistent despite some minor fluctuations. It can be measured separately and subtracted from Raman spectra in post-analysis with acceptable accuracy. The background subtraction will not be satisfactory if the shot noise of the Raman background dominates SNR, which applies to extremely weak Raman signals. In such cases, a waveguide with high SBR is suitable. But we prefer to avoid such extreme conditions through methods such as locally enriching the analyte. By increasing the signal intensity, the SNR is improved while the background subtraction is more accurate, better than using a dielectric waveguide with higher SBR. In this work, we focus more on the η_0. Meanwhile, for the highest η_0, the optimal slot width of 40 nm is not easily feasible with current fabrication technologies. Therefore, in practice, we usually choose the design with the highest η_0 that processings allow.

3.3.2 Fabrication

We fabricated a series of Ta_2O_5 slot waveguides with varied rail and slot widths. The rail width sweeps from 100 nm to 200 nm and the slot width from 40 nm to 150 nm, as marked in Figure 3.3. They were fabricated in the cleanroom of University of California, Santa Barbara, in the context of a collaboration with the team of Prof. D. Blumenthal. The process flow is sketched in Figure 3.5 by the dashed rectangle. 400-nm-thick Ta_2O_5 layer is sputtered onto a 3-μm-thick SiO_2 layer on a Si substrate. This step is accomplished by FiveNine Optics, a commercial facility for thin-film deposition. Then, a layer of ruthenium (Ru) is sputtered onto the sample as a hard mask, in which the pattern is defined using ebeam lithography (EBL) and reactive ion etching (RIE). Then the Ta_2O_5 underneath is etched in inductively coupled plasma (ICP) using CF_4 gas. Finally, the Ru hard mask is removed by dry etching with oxygen.

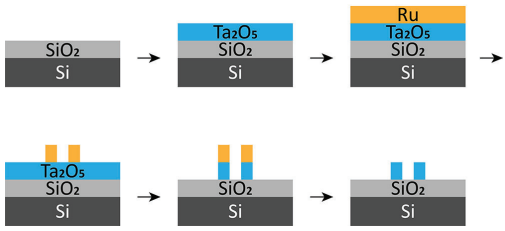

Figure 3.5: Process flow of Ta_2O_5 slot waveguides

Figure 3.6 shows the cross-sections of two waveguides under a scanning electron microscope (SEM). The slot widths are 40 nm and 70 nm in design, respectively.

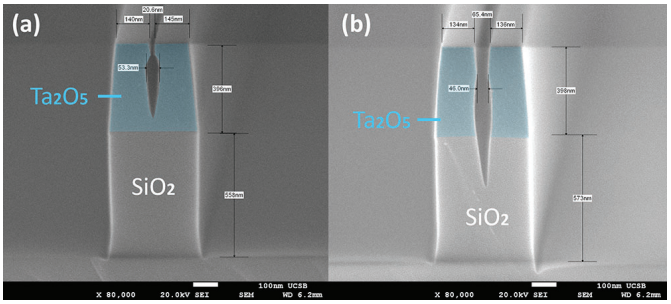

Figure 3.6: Cross-sections of the fabricated Ta_2O_5 slot waveguides under SEM. The target slot widths are 40 nm and 70 nm, respectively.

The reactive species cannot easily escape from such narrow openings. They widen the slot beneath the surface and cause a bottleneck-like shape. It changes the conversion efficiency and may induce wettability problems. Moreover, due to the scattering of reactive species, the etch rate inside the slot is lower than outside. It has led to about 500 nm over-etching into the SiO_2 outside the slots, as seen in Figure 3.6. With a total height of around 900 nm, the waveguides have an extreme aspect ratio and are subject to collapse. As shown in the images in Figure 3.7, the collapse may occur at the strip-to-slot transitions, where the extra rail is introduced from a narrow width. Such collapse happened widely on both samples we fabricated. Further optimization of the etching process is required to demonstrate acceptable durability.

3.3.3 Raman signal of ethanol on Ta_2O_5 and Si_3N_4 waveguides

The experimental setup is sketched in Figure 3.8. A Toptica XTRA II laser (785 nm) is used as the pump to excite the fundamental quasi-TE mode. The pump power before the objective is 5 mW. Light is coupled into and out of the waveguide with a microscope objective (NA=0.6) through an edge coupler 3-μm wide. The photonic chip is clamped vertically on a holder and placed in a Petri dish. Liquid can be applied into the Petri dish to cover the sensing window of the waveguide. A spectrometer analyzes the Raman signal in reflection with a camera cooled to -60°C. The integration time is 5 s for each spectrum.

First, by measuring the Raman signal of all waveguides under air cladding, we obtain the Raman background of each waveguide. Next, the sample is immersed

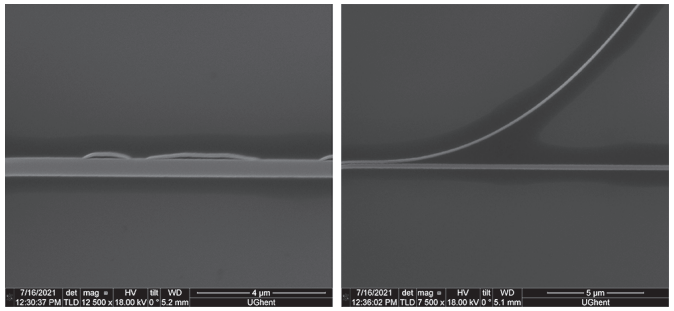

Figure 3.7: Top-down view of collapsed slot waveguides under SEM

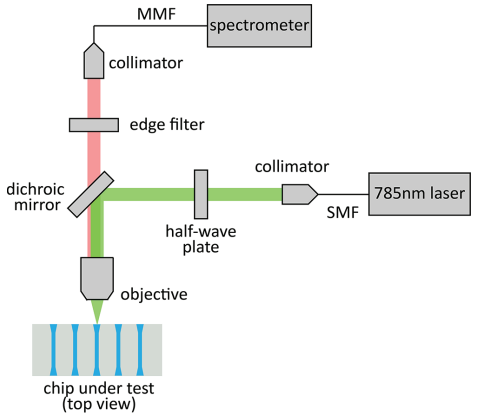

Figure 3.8: Experimental setup

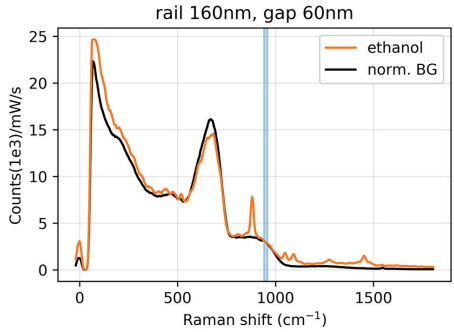

Figure 3.9: Raman spectra of one Ta_2O_5 slot waveguide with air (black) and ethanol (orange) cladding, respectively. The Raman background (black) is normalized.

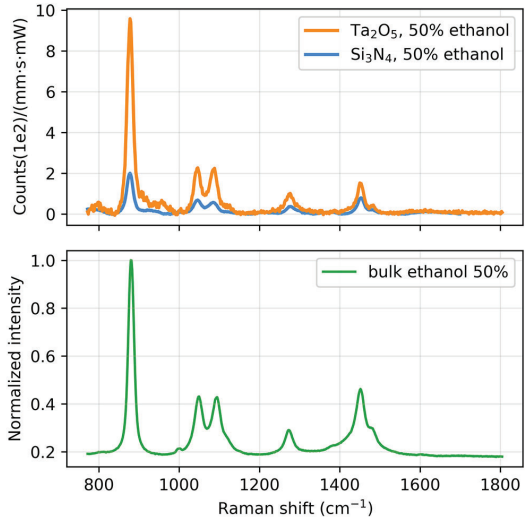

Figure 3.10: (Top) Raman spectra of 50% ethanol on Ta_2O_5 and Si_3N_4 slot waveguides. (Bottom) A reference signal of ethanol measured in bulk liquids confocally with an exposure time of 10 seconds.

in ethanol, and the waveguides are measured again. Figure 3.9 shows the air- and ethanol-clad spectra measured on one of the waveguides. The prominent peak around 670 cm^{-1} is a signature peak of Ta_2O_5. The signal intensity is represented by CCD counts on the spectrometer normalized by the pump power and integration time. Distinct peaks of ethanol can be observed in higher wavenumbers. Then, the Raman background is subtracted from the ethanol-clad spectrum, starting from normalizing the background. It is performed by minimizing the intensity difference between the two spectra in a spectral range next to the ethanol peak at 880 cm^{-1}, which is marked with a blue stripe in Figure 3.9. Once subtracted, it will cancel the Raman background around the peak with reasonable accuracy. However, as seen in spectral ranges further from the 880 cm^{-1} in Figure 3.9, the good agreement between the Raman background and the ethanol-clad signal is gradually lost. The intensity of the Raman background is lower below 400 cm^{-1} and above 1000 cm^{-1}. This change of the general shape can happen due to changed optical alignment and degraded sample condition. The physical cause remains uncertain.

Then the signal intensity of ethanol is obtained by subtracting the normalized background from the ethanol-clad spectrum. The waveguide with the highest signal intensity has a rail width of 120 nm and a slot width of 90 nm. In addition to the Ta_2O_5 slot waveguides, we also measured a conventional Si_3N_4 slot waveguide. It was fabricated by IMEC on a 300 nm Si_3N_4 platform with a rail width of 275 nm and a slot width of 150 nm. Both waveguides are marked by black dots in Figure 3.3 for comparison with the theoretical optimal. The Si_3N_4 waveguide is tested during immersion in 50% ethanol. For comparison, the above optimal Ta_2O_5 waveguide is tested under the same condition. The background-subtracted spectra are presented in Figure 3.10, which are normalized by the waveguide length, integration time, and pump power. The bottom half of Figure 3.10 includes a reference spectrum of ethanol measured using a confocal Raman microscope in bulk liquids. Good agreement of peak positions can be seen.

At the 880 cm^{-1} peak, the Ta_2O_5 waveguide generates a normalized count of around 960, while the Si_3N_4 waveguide gives approximately 200. From the fabricated cross-sections of the Ta_2O_5 and Si_3N_4 slot waveguides, η_0 are numerically calculated to be 1.23 and 0.24, respectively. The 5.1-fold difference in simulated η_0 matches the 4.8-fold difference in signal intensity.

It is worth noting that the other peaks in Figure 3.10 do not follow the 4.8-fold difference in intensity. The signal intensity of Si_3N_4 waveguide seems to increase with wavenumber. From the reference spectrum of ethanol shown in Figure 3.10, we observe that the 880 cm^{-1} peak is roughly 2.5-fold stronger than the 1450 cm^{-1} peak. This contrast also applies to the spectrum of the Si_3N_4 slot waveguide. However, the 880 cm^{-1} peak of the Ta_2O_5 waveguide is unproportionally strong.

Such relative intensity can be found in the original spectrum before background subtraction in Figure 3.9. A change in the optical alignment between the objective and the waveguide could have caused this difference. We observed that by changing the relative position of the waveguide, the general slope of the Raman signal slowly varies. The effect is more substantial in the spectral range further from the spectral center, which is about 900 cm^{-1} in this case. The optical alignment on those two waveguides was optimized by maximizing the signal in different spectral regions. More specifically, the alignment of the Ta_2O_5 waveguide was optimized next to the 880 cm^{-1} peak, and the Si_3N_4 around 660 cm^{-1}. It may have caused the difference in the relative intensity of ethanol peaks, especially at higher wavenumbers. With the current method of measurement and background subtraction, the result is most accurate in the optimized range.

3.4 Conclusions

This chapter discussed the importance of high-index-contrast waveguide platforms and optimized waveguide designs in WERS. Higher index contrast gives rise to a stronger evanescent field that enhances the Raman signal. Nonetheless, the waveguide material introduces a unique Raman background that generates noise. In certain conditions, the Raman signal is not significantly stronger than the Raman background, especially with low analyte concentrations. Therefore it is necessary to consider both the index contrast and Raman background when selecting a waveguide platform. Among several candidates, Ta_2O_5 is found with higher index contrast (n=2.11) and moderate Raman background, comparable to the conventional Si_3N_4 platform.

The waveguide geometry should also be carefully chosen to exploit the potential of a waveguide platform. From numerical calculations, slot waveguides can produce strong Raman signal with potentially lower Raman background and moderate propagation loss. We numerically evaluated the performance of a series of Ta_2O_5 slot waveguides and pinpointed the optimal geometry. When the guiding layer thickness is 400 nm, a Raman conversion efficiency η_0 of 1.33 can be achieved with a rail width of 150 nm and a slot width of 40 nm. 2.3 times higher than the optimal value on a 300 nm Si_3N_4 platform.

We fabricated and measured some Ta_2O_5 slot waveguides. A distinct Raman signal can be observed on the waveguides using ethanol as a modal analyte. Among all the waveguides, the one with a rail width of 120 nm and a slot width of 90 nm generates the strongest Raman signal of ethanol. We also measured on a conventional Si_3N_4 slot waveguide with 275-nm wide rails and a 150-nm wide slot. The signal intensity is 4.8-times stronger than the Si_3N_4 waveguide at the major peak

around 880 cm^{-1}. It matches the 5.1-fold difference in numerically computed η_0. The signal intensity of a new waveguide design can be predicted by comparing its η_0 to a baseline.

With the current etching process, the low etch rate in narrow slots and tilted inner sidewalls induced significant over-etching into the buried oxide. The aspect ratio of the waveguides reaches 3:1. It makes the waveguide very fragile, especially in measurements of bulk liquids. The durability problem prevents its application. Ta_2O_5 narrow-slot waveguides will be a promising candidate for WERS once the etching process is optimized and the durability is improved. For instance, the dry etching of Ta_2O_5 can be replaced by depositing Ta_2O_5 on pre-patterned photoresist followed by a lift-off process, as demonstrated by Khorasaninejad *et al.* in [59].

4

Analyte enrichment

In previous chapters, we discussed the principle of WERS and the optimization of dielectric waveguides. By exciting and collecting Raman signal from a photonic waveguide, the signal intensity is orders of magnitude stronger than a conventional Raman microscope. It can be further enhanced by selecting a better waveguide material and optimizing the design. However, detecting analytes in diluted concentrations is still challenging, especially below a millimole per liter (mM). This low concentration range is particularly interesting in various applications looking for specific compounds, such as water quality monitoring. One of the solutions is to selectively enrich the concentration of analytes locally around the waveguide. Various adsorbents have been studied for local analyte enrichment, such as biological molecules [60–62], polymers [24, 63–65], and mesoporous materials [66–68]. Sorbents have been adopted in WERS to enrich gas-phase chemicals, including volatile organic chemicals [69] and chemical warfare agent simulants [24, 70]. In this chapter, we extend sorbent-assisted WERS to liquid-phase sensing. Modified mesoporous silica is employed as the sorbent. Due to its higher affinity to hydrophobic molecules, it can enrich hydrophobic molecules present in water in trace amounts. In this study, we demonstrate sensitive Raman sensing of hydrophobic analytes in aqueous solutions using a functionalized Si_3N_4 slot waveguide. Some contents are adapted from our previous publication [71].

4.1 Mesoporous silica as a sorbent

The term "mesoporous" refers to porous materials with pore widths between 2 nm and 50 nm [72]. Mesoporous silica is a well-known high-surface-area sorbent versatile in surface chemistry [73–75]. It has been studied for catalysis [76,77], low-k dielectrics [78], separation [79,80], sensing [81,82], etc. Unlike some polymer adsorbents, mesoporous silica is not prone to swelling, providing better mechanical stability. Also, the layer properties are highly reproducible in preparation. However, due to its hydrophilicity, mesoporous silica is not chemically stable in aqueous environments. It is known that the durability in water can be improved by modifying the surface with hexamenthyldisilazane (HMDS). The reaction with HMDS adds methyl groups to the surface and turns the surface hydrophobic in post-synthesis. The highly hydrophobic methyl groups turn the surface hydrophobic.

Hydrophobic molecules are usually non-polar. In chemistry, polarity describes the distribution of electric charges over a chemical bond or a molecule. If the atoms attract electrons unevenly, the molecule would exhibit a permanent dipole moment, namely a polar molecule. For example, in water molecules (H_2O), the electrons are attracted towards the oxygen atom. As shown in Figure 4.1, the two hydrogen atoms situate at an angle, so the local variation of the two O-H bonds cannot fully cancel each other. Therefore, H_2O is a polar molecule that is slightly positive at the hydrogen end and slightly negative at the oxygen end. Atoms in symmetric biatomic molecules, e.g. H_2, share the electrons evenly, resulting in non-polar molecules. It is also non-polar if the polar bonds cancel out, such as CO_2, where the three atoms form a straight line. The common phrase "like dissolves like" describes the high solubility of polar in polar, and non-polar in non-polar. This is due to their similarity in the distribution of electric charges. On the contrary, the difference in charges reduces the affinity of polar to non-polar, and vice versa.

In many applications, we are interested in the small amount of non-polar composition dissolved in aqueous environments, such as some pollutants in water, and lipids in blood. The HMDS modified mesoporous silica show higher affinity to the non-polar molecules than the water-like solvent. The non-polar analyte in

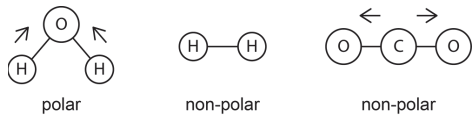

Figure 4.1: Examples of polar and non-polar molecules. The arrows represent the dipole moments.

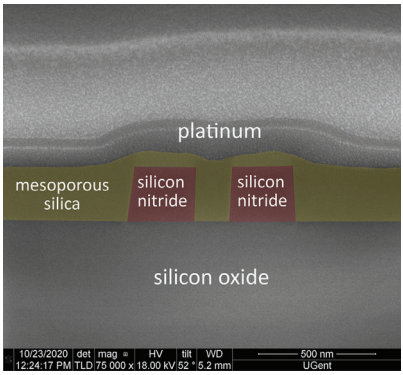

Figure 4.2: Cross-section of a Si_3N_4 slot waveguide coated with mesoporous silica. Platinum is deposited during focused ion beam (FIB) cross-sectioning.

interest can be strongly enriched in the sorbent. For example, Baumgartner *et al.* used it to enrich benzonitrile and valeronitrile in water for detection [67].

Previous works have shown that a photonic waveguide can generate a much stronger Raman signal than a confocal Raman microscope [83]. It paves the way for more demanding applications, such as water quality monitoring and blood testing. However, the current detection limit of WERS still needs to be improved by one or two magnitudes to meet the requirements. It may be overcome by applying a sorbent onto the waveguide and locally enrich the analyte. When detecting pollutants or biomolecules from aqueous environments, HMDS-modified mesoporous silica is a promising adsorbent that can be combined with Si_3N_4 waveguides.

We experimentally tested the HMDS-modified mesoporous silica on Si_3N_4 slot waveguides. The photonic chip is fabricated by IMEC on a silicon nitride platform. There is a 300-nm-thick Si_3N_4 layer deposited on top of a 2-μm-thick buried oxide via plasma-enhanced chemical vapor deposition (PECVD). The slot waveguides are then defined by deep UV lithography and reactive ion etching (RIE), with a slot width of 150 nm and a rail width of 300 nm. At both ends, the slot waveguides are tapered into 3-μm-wide strip waveguides for edge coupling. The coupling loss is at most 7.4 dB per facet, which is similar to that in previous experiments using bare Si_3N_4 slot waveguides [23]. A layer of SiO_2 is deposited on top of the Si_3N_4 core as the top cladding. Part of it is later removed to expose a 6-mm-long section for sensing.

The waveguides are then coated with a 425-nm-thick layer of mesoporous

silica that is later modified with HMDS. Figure 4.2 shows the cross-section of the final waveguide. Synthesis of the coating is performed at Vienna University of Technology in collaboration with the team of Prof. B. Lendl. The mesoporous silica is synthesized using the surfactant templating method [84]. In this method, a homogeneous solution of silica and surfactant is gradually concentrated, and the silica-surfactant micelles form oriented mesophases. Different film structures can be achieved by controlling the ratio between silica and surfactant, such as three-dimensional (3D) hexagonal or cubic. Then the surfactant is removed by rinsing with a solvent, leaving the silica mesoporous film. In this work, the soluble silica comes from tetraethoxysilane (TEOS) dissolved in ethanol, and the surfactant is cetyltrimethylammonium bromide (CTAB). After the self-assembly of the thin film, the surfactant is removed by immersion in absolute acetone. Meanwhile, HMDS is introduced in the absolute acetone to functionalize the surface.

4.2 Enrichment of non-polar analytes on waveguides

4.2.1 Comparison to bare waveguides

The experiment setup is shown in Figure 3.8. We use a Toptica XTRA II laser at 785 nm to excite the fundamental quasi-TE mode. The pump power is 60 mW before the objective. The Raman signal is analyzed by a spectrometer equipped with an Andor iDus 401 camera cooled to -60°C. For coupling light in and out of the waveguide, we use an objective with 0.6 NA and 40× magnification. Each spectrum is integrated for 5 s. In our experiments, we employed cyclohexanone as a model analyte, which is a common non-polar solvent in industry. It has a low solubility in water of 8.6 g/100 mL, which is equivalent to a volume concentration of 9%. Even with the maximum concentration in water, bare silicon nitride slot waveguides cannot generate a distinct Raman signal of cyclohexanone. As a non-polar compound, cyclohexanone dissolves better in non-polar solvents, such as isopropanol (IPA). Therefore, the analyte is firstly dissolved in IPA with 10%-30% volume concentrations and applied onto a bare Si_3N_4 slot waveguide. The result is shown in Figure 4.3(a). We can observe cyclohexanone peaks at 757 cm^{-1}, and its intensity increases with the concentration. The signal is quantified by the number of photons (or counts) on the center pixel of the peak. With 10% cyclohexanone, its peak height is 8450 counts per second (ct/s).

We then move to coated waveguides with cyclohexanone aqueous solutions. The result is shown in Figure 4.3(b). It shows the Raman spectra of deionized (DI) water, 0.01%, 0.1%, and 1% cyclohexanone probed by a Si_3N_4 slot waveguide coated with HMDS-modified mesoporous silica. The chip is cleaned with IPA and

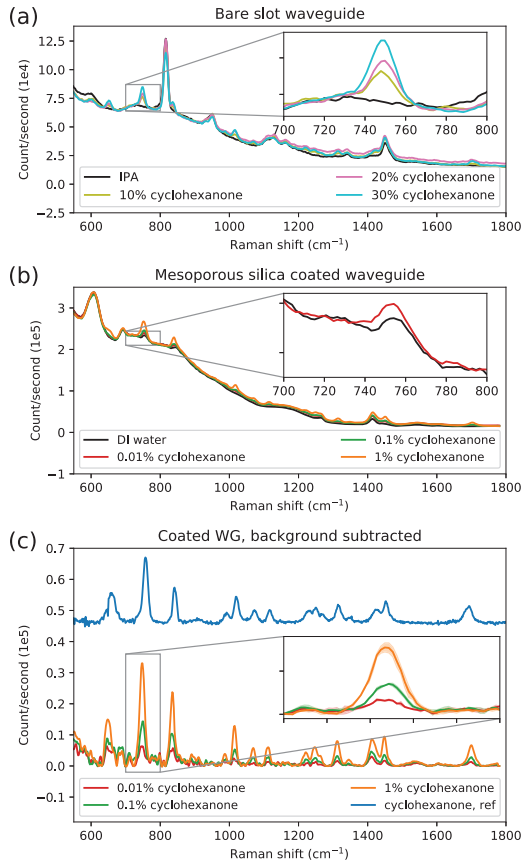

Figure 4.3: (a) Raman spectra of IPA and 10%, 20%, and 30% cyclohexanone in IPA on a bare Si_3N_4 slot waveguide. (b) Raman spectra of DI water and 0.01%, 0.1%, and 1% cyclohexanone in water on mesoporous-silica-coated Si_3N_4 slot waveguide. (c) Raman spectra of cyclohexanone solutions on coated waveguides, without background. The blue curve is a reference spectrum of cyclohexanone. The shaded rea in the inset corresponds to the deviation over two chips.

DI water between measurements, and the disappearance of cyclohexanone peaks validates the cleanliness of the chip. These spectra are normalized by minimizing the distance between the Raman background around the 757 cm^{-1} peak. We can identify some features induced by the coating and the broad features from the silicon nitride core. The inset of Figure 4.3(b) shows the Raman spectra around the 757 cm^{-1} peak with 0.01% cyclohexanone.

To quantify the performance of the coated waveguides, we first subtract the DI water background from the cyclohexanone results and then apply baseline correction using the asymmetric least squares method [85]. The results are shown in Figure 4.3(c) with the inset zooming onto the 757 cm^{-1} peak. The signal intensities are 6548, 14444, and 33083 ct/s, respectively. The blue curve is a reference spectrum of pure cyclohexanone measured in bulk liquid using the same confocal Raman microscope. An excellent correspondence can be seen between the reference and the measured spectra. Cyclohexanone measurements are repeated on another coated waveguide with the same geometry to characterize the reproducibility. The deviation between the two measurements is shown as the shaded areas in the inset of Figure 4.3(c). The results are highly consistent.

As shown in Figure 4.4(a), the peak intensity on the bare slot waveguide varies linearly with analyte concentration. The same signal intensity of 6548 ct/s can be achieved with 0.01% cyclohexanone on the coated waveguide or 6% on the bare waveguide, as indicated by the black dashed line in Figure 4.4(a). Therefore, at 0.01% cyclohexanone (equivalent to 970μM), the enrichment factor of the coating is around 600.

On the coated waveguides, we observe a nonlinear dependence of the signal intensity on bulk concentration, as shown in Figure 4.4(b). This is one of the typical behaviors of adsorbents. With limited absorption sites and no layering of the analyte, it is increasingly difficult to find sufficient spare sites with increasing ambient concentrations. The amount of absorbed molecule may eventually saturate at a high concentration, leading to a plateau in Figure 4.4(b). It is one of the most common absorption isotherms. There are other types of isotherms with different shapes. However, their characteristics and origins are beyond the scope of this thesis. A systematic discussion can be found in this technical report from the International Union of Pure and Applied Chemistry [86]. From Figure 4.4(b), a stronger enrichment is expected at lower concentrations. The signal intensity can be predicted by the Freundlich model, which is an empirical model between the number of absorbed molecules and the applied concentration. It can be expressed as

$$I = Kc^{1/n} \tag{4.1}$$

where I is the signal intensity, and c the ambient concentration. K and n are

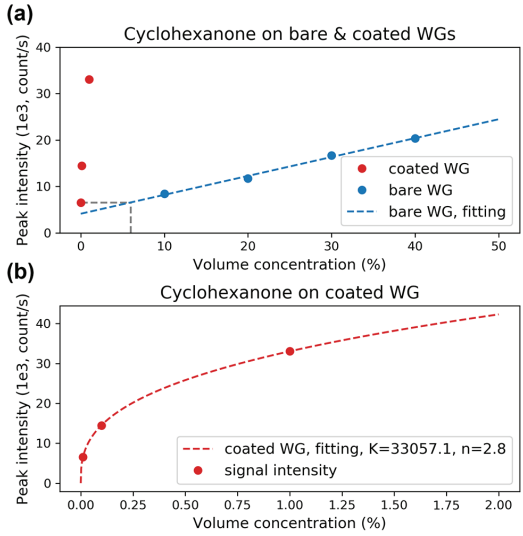

Figure 4.4: (a) Peak intensity at 757 cm^{-1} of cyclohexanone on bare and coated Si_3N_4 slot waveguides, repectively. The response of the bare waveguide can be predicted from a linear fitting on the signal intensity. (b) Peak intensity at 757 cm^{-1} of cyclohexanone on the coated waveguide. The fitting coefficients of the Freundlich model is listed in the figure.

constants that are related to absorbent properties. A fitting of the presented data to the Freundlich model shows that the detection limit of this coated waveguide may reach the 10-μM level.

Meanwhile, the peak height of 6550 ct/s for 0.01% cyclohexanone corresponds to a Raman conversion efficiency of 1.65×10^{-12}/cm from pump to Raman signal. It carries an error margin of 15% by considering the uncertainties in waveguide lengths, coupling loss and signal propagation loss within the microscope. In comparison, a conversion efficiency of 10^{-11}/cm for pure IPA is obtained with a Si_3N_4 strip waveguide [39]. It is equivalent to 7×10^{-16}/cm for 0.01% cyclohexanone, given the difference in molecular density and Raman scattering cross-section. Therefore, the coated slot waveguide outperforms the bare strip waveguide by a factor of around 2200.

The ultimate performance of the coated waveguide can be even higher. However, due to the nonlinear nature of the Freundlich model, an extensive study across multiple samples is necessary to fully quantify the potential of the waveguide sensor.

4.2.2 Multiplexed detection

It is well known that Raman spectroscopy can quantify multiple compounds simultaneously. However, on the coated waveguides, analytes might be competing for limited adsorption sites, and the signal of one compound can be influenced by another.

To characterize the coated waveguide's capability for multiplexed sensing, we measure the Raman signal of multiple aqueous solutions comprising varying amounts of cyclohexanone and 1-indanone. 1-Indanone is an aromatic non-polar solid compound that is involved in metabolism and drug synthesis. Figure 4.5(a) shows the spectrum of 97 mM (1%) cyclohexanone and 7.6 mM (1 g/L) 1-indanone with the DI water background already subtracted. Using the reference spectra obtained from bulk solutions, we can attribute the Raman peaks to each individual analyte, as shown in the inset. It indicates the coated waveguide can at least be used for multiplex identification.

We further investigate the potential for multiplex quantification. Figure 4.5(b)–(d) show the Raman spectra of the mixture with different mixing ratios, each measured three consecutive times. Figure 4.5(b) and (c) both have 1.9 mM (0.25 g/L) 1-indanone in the solution, while the cyclohexanone concentration is doubled from 24 mM (0.25%) to 48 mM (0.5%). The peak count of 1-indanone at 1150 cm^{-1} increases slightly from 142 to 167 ct/s. Similarly, the cyclohexanone signal also

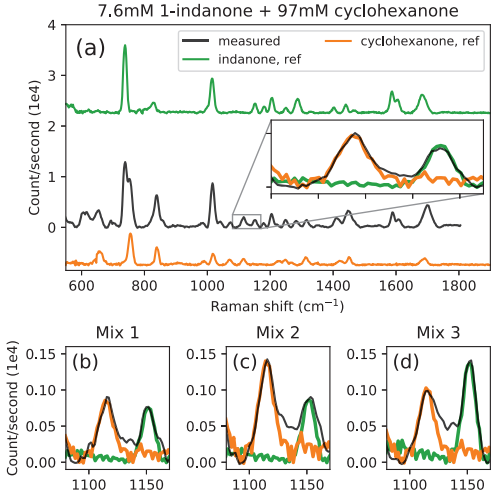

Figure 4.5: (a) Background-subtracted spectrum of 7.6 mM (1 g/L) 1-indanone and 97 mM (1%) cyclohexanone solution (black). The orange and green curves show the reference spectra of the two compounds, respectively. The inset shows the range 1075–1175 cm^{-1} and the fitted peak profiles. Raman spectra of different mixtures are included in (b), (c), and (d). The concentrations can be found in Table 4.1.

Figure nr.	1-indanone (g/L)	cyclohexanone (%)
(a)	1	1
(b)	0.25	0.25
(c)	0.25	0.5
(d)	0.5	0.25

Table 4.1: Concentrations of mixed solutions presented in Figure 4.5.

slightly increases from 184 to 210 ct/s from Figure 4.5(b) to (d) when the 1-indanone centration doubles.

We believe this variation in peak height is due to imperfect spectral analysis instead of real physical limitations. In Figure 4.5(b)–(d), the tail of one peak overlaps with the other and leads to a small increase in peak height. The spectrum from individual components can in principle be deconvolved by a well-trained mathematical model. However, building such a model requires a comprehensive mapping of the Raman spectra at varying concentrations, and it is beyond the scope of this study.

4.3 Desorption and reusability

Desorption of adsorbed molecules is essential to monitor the variations of the analyte concentration. To examine the desorption properties of the coated waveguide, we first immerse the sample in 6 g/L 1-indanone aqueous solution until the signal intensity reaches the maximum. Afterward, we quickly remove the solution and apply DI water. Meanwhile, we record the height of the 738 cm^{-1} peak with a 0.1 s integration time.

Figure 4.6 shows the temporal profiles of the signal intensity of two repeated experiments on one sample. The initial plummet of peak count corresponds to the application of DI water, which slightly disturbs the optical alignment between the waveguide and the microscope objective. Then, the peak counts quickly increase as the alignment restores. Also, the application of water reduces the propagation loss, and the peak count even increases beyond its original value. When the desorption reaches an equilibrium (t>200 s), a weak 1-indanone signal is still present. It suggests that the applied volume of DI water (approximately 1 mL) cannot fully desorb 1-indanone from the sorbent. However, we would like to emphasize that this is limited by the volume of DI water and the low solubility of 1-indanone in DI water.

To prove the desorption is currently only volume limited, we perform the measurement using IPA instead of DI water on the same chip. As 1-indanone has a higher solubility in IPA, we expect better desorption of 1-indanone from the coating. The results are shown in Figure 4.6(b). With the same volume as DI water, IPA almost completely removes the adsorbed 1-indanone.

It is important to note that the signal intensity always restores after immersion in 1-indanone again in the desorption tests. This desorption study further indicates the potential of concentration monitoring and the reusability of the coated waveguide.

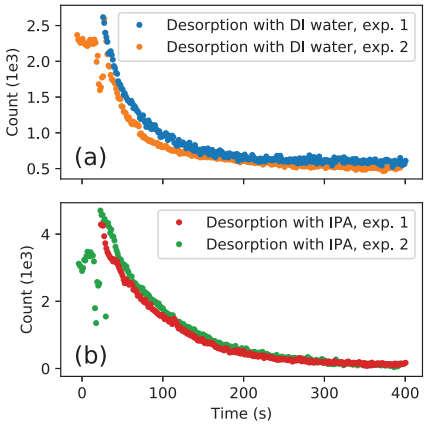

Figure 4.6: Desorption profiles of 1-indanone using (a) DI water and (b) IPA. The integration time of each measurement is 0.1 s. Desorption with each solvent was performed two times.

4.4 Conclusions

We present an ultra-sensitive on-chip Raman sensor for the identification and quantification of non-polar molecules in water. Combined with a mesoporous silica coating modified with HMDS, WERS shows much higher signal intensity of cyclohexanone in aqueous solutions compared to bare Si_3N_4 slot waveguides. For the lowest concentration (0.01%, 970μM) measured on a coated waveguide, the peak count of 6550 ct/s is equivalent to the peak count from 6% cyclohexanone on the bare slot waveguide. It suggests an enrichment factor of 600 in the coating for 0.01% cyclohexanone. The Raman conversion efficiency of 970 μM cyclohexanone solution from the pump to Raman signal is 1.65×10^{-12}/cm, with an error margin of 15%, which is three orders of magnitude stronger than bare strip waveguides [39]. We also show unambiguous simultaneous detection of 1-indanone and cyclohexanone. The precision is not significantly affected by the introduction of another compound. Besides, DI water with a volume of 1 mL can partly desorb 1-indanone molecules from the sorbent, while 1 mL IPA can virtually remove all the adsorbed molecules within minutes. It indicates the potential of the coated waveguides for the real-time monitoring of hydrophobic analytes.

The combination of Si_3N_4 slot waveguide and HMDS-modified mesoporous sil-

ica film is suitable for organic sensing using WERS. With considerable enrichment of non-polar molecules, promising simultaneous detection, and robustness of the sensor, this coated Si_3N_4 waveguide sensor holds potential for diverse applications, including the monitoring of non-polar contaminants and biomolecules in aqueous environments.

5

Micro-transfer-printed silicon nitride grating couplers

The excitation of the Raman signal requires a laser with moderate power and narrow linewidth in the near-infrared range, which is not yet readily integrated on silicon nitride platforms. Free-standing lasers are still commonly employed as pump for WERS. Two major categories are available to couple the laser into the PIC: grating couplers and edge couplers. We usually use edge couplers for WERS for their broad bandwidth and tolerance of fabrication variations. But the coupling efficiency of conventional single-layer, wide-to-narrow edge couplers is far from ideal, as low as -7 dB per facet. The coupling efficiency can be drastically improved by adapting the inverse taper [87], inter-layers [88], or staged tapers [89]. For wavelengths around 1550 nm, the coupling efficiency of Si_3N_4 edge couplers is reported to reach -0.35 dB experimentally [88, 89]. However, such designs require stringent optical alignment between the optical fiber and the coupler. For biological and pharmaceutical applications where a disposable chip is preferred, such critical alignment is inconvenient and challenging in practice. A design featuring simpler alignment and moderate coupling efficiency might better fulfill the purpose.

Compared to edge couplers, grating couplers offer better alignment tolerance and more flexible positions on the wafer. Conventional Si_3N_4 grating couplers have a moderate coupling efficiency of around -4 dB per port. Two factors have led to the unsatisfactory coupling efficiency. On the one hand, the coupling efficiency is

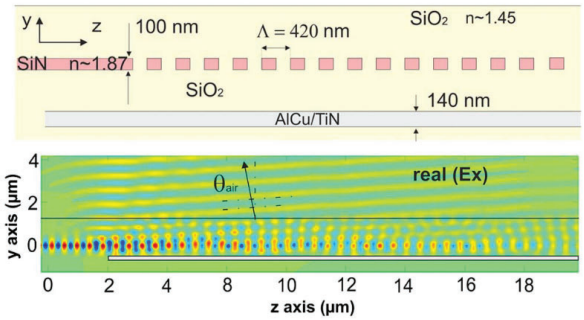

Figure 5.1: 2D cross-section schematic of a Si_3N_4 grating coupler and AlCu/TiN bottom reflector. The bottom figure represents the electric field in TE polarization. Reproduced from [90].

limited by the mode mismatch between the grating and the optical fiber. On the other hand, a considerable fraction of power is diffracted toward the substrate. It has been demonstrated that the efficiency can be boosted with bottom reflectors, such as metal, gratings, and distributed Bragg reflectors [90–92]. An example of such a bottom reflector is shown in Figure 5.1, by which the downward diffracted light is redirected. The depth and position of the bottom reflectors need to be optimized for each target wavelength and circuit design, resulting in additional modification to standard Si_3N_4 platforms. It would greatly increase the time and cost in large-scale processing of the on-chip Raman sensor.

This chapter presents a micro-transfer-printed Si_3N_4 fiber-to-chip coupler with a metallic bottom reflector. The grating couplers and bottom reflectors are fabricated separately and later transferred onto a circuit on a standard Si_3N_4 platform. In this way, the coupling efficiency is improved without jeopardizing the rest of PIC. Following an introduction to micro-transfer-printing technology, I present the working principle and simulation results of the device. Then, I discuss the fabrication process flow and some practical problems encountered. Finally, the measurement method and results are shown. Some content is adapted from our previous publication [93].

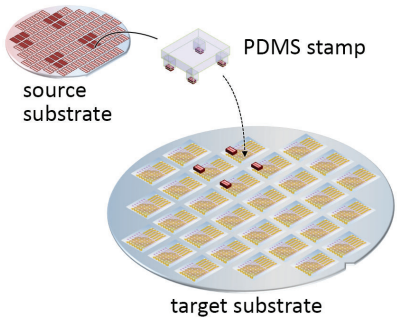

Figure 5.2: Schematic of micro-transfer-printing multiple components from a source substrate to target substrate in parallel using a PDMS stamp

5.1 Introduction to micro-transfer-printing technology

The standard Si_3N_4 platforms in large-scale processing only consist of the silicon substrate, SiO_2 cladding and Si_3N_4 guiding layer. It is not convenient to include grating couplers with bottom reflectors on such platforms. When bottom reflectors, either single-layer or distributed Bragg reflectors, are required in the circuit, the fabrication process must be adapted for each design, resulting in much more cost and processing time. However, the problem may be circumvented by fabricating the circuit and the grating couplers with bottom reflectors separately and integrating them later.

Chip-scale integration of materials and components has been widely explored in recent years. Particularly in silicon photonics, the lack of light sources, modulators, and detectors has led to continuous efforts looking for reliable integration technologies of heterogeneous components on Si platforms. Compared to the conventional flip-chip and wafer bonding, micro-transfer-printing (μTP) is a more recent technique developed since 2004 [94]. In the Photonics Research Group, the team of prof. Günther Roelkens has demonstrated the integration of various components using μTP technology. Examples include photodiodes [95–97], lasers [98–100], and amplifiers [101, 102] integrated on Si, Si_3N_4, and lithium niobate platforms. Such integration extends the limit of silicon photonics and paves the way toward fully integrated PICs.

Figure 5.3 depicts the basic process of printing a device onto a target circuit.

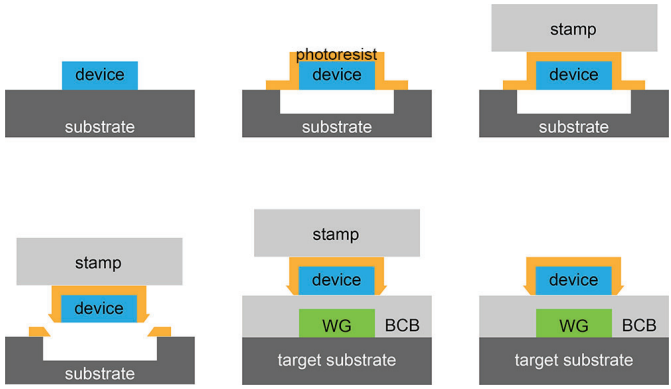

Figure 5.3: Schematic of a basic process of micro-transfer-printing using a polymer stamp. The photoresist can also be replaced by a hard mask.

μTP uses a polymer stamp to transfer components from the source substrate to the target substrate with high alignment accuracy. By transferring multiple components in parallel on one stamp, tens or hundreds of components can be transferred in one printing cycle, which takes down to 30 seconds. Moreover, as the components are pre-fabricated densely, it wastes less source material than previous techniques. A general process of μTP is shown in Figure 5.2. Devices are picked up by an elastomeric stamp made of polydimethylsiloxane (PDMS) and printed onto a target substrate with circuits. After the patterning of the devices, local openings are dry-etched into the source substrate. Then a sacrificial layer between the device and the substrate is removed to release the devices from the substrate. The devices are kept suspended on the substrate by tethers, which are broken during picking up. When picking up a device, the PDMS stamp is aligned and brought into tight contact with the top surface of the device and then moves up at high speed. In this case, the adhesion of the device to the stamp is more substantial than to the substrate. After aligning the device to the target circuit, the stamp is deposited onto the target substrate and pulled up slowly. Contrary to picking-up, the adhesion to the substrate is higher, and the device is attached to the target substrate using either Van der Waals forces or an adhesion promoter. As the PDMS stamps are transparent, visual alignment between devices and target circuits is possible, offering an alignment accuracy of around 1.5μm for large arrays in the 3σ range.

In this chapter, we utilize μTP technology to integrate grating couplers with

bottom reflectors onto a standard Si_3N_4 platform. Efficient coupling can be achieved without jeopardizing the rest of the PIC. Moreover, it creates more diverse options for the supply chain of PICs by enabling the addition of grating couplers in a late stage of fabrication.

5.2 Design of the grating coupler

In Figure 5.4, we sketch the cross-section and top-down view of the grating coupler with a bottom reflector. The source device contains a grating, an adiabatic taper, a gold reflector and SiO_2 cladding, while the target substrate has another adiabatic taper, a photonic waveguide, and a taper connecting them. The source device is attached to the target substrate assisted by a thin layer of benzocyclobutene (BCB).

The gratings have a width of 5 μm to match the core diameter of single-mode optical fibers at 785 nm. When light is coupled into the circuit through the grating coupler, the downward-diffracted light is reflected by the gold reflector and coupled into the taper. By carefully adjusting the vertical distance between the reflector and the grating, we can realize constructive interference between the reflected and directly coupled light for specific wavelengths. The tapers in source and target structures have the same geometry but are in opposite directions. They form an adiabatic coupler between the Si_3N_4 layers, through which light is coupled to the target Si_3N_4 layer. Compared to directional couplers, such adiabatic couplers achieve the same efficiency with more extensive lengths and better tolerance to layer thicknesses, indices, and coupler length. Then the light is tapered from the adiabatic coupler into a waveguide.

The coupling efficiency is boosted mainly by the bottom reflector. Meanwhile, the gratings are apodized to further improve the coupling efficiency. Regular grating couplers have a constant pitch and fill factor, leading to a constant coupling strength and an exponentially decaying out-coupling power. It has a considerable mismatch with the Gaussian mode of optical fibers. By varying the fill factor and the period along the propagation direction, the out-coupling power can become more Gaussian-like [103–107]. In this work, we adapt the method of Marchetti *et al.* presented in [107]. The fill factor F is linearly varied along the grating as

$$F = F_0 - R \cdot z \tag{5.1}$$

where F_0 is the initial fill factor at the start of the grating, R is the varying rate of the fill factor, and z is the distance from the grating input. The initial fill factor is set to 0.9 to mitigate the abrupt change of optical impedance and reduce scattering. It has been shown that a fill factor of 0.5 gives rise to the lowest reflection and thus the highest out-coupling power [108]. Therefore, the out-coupling power is lowered

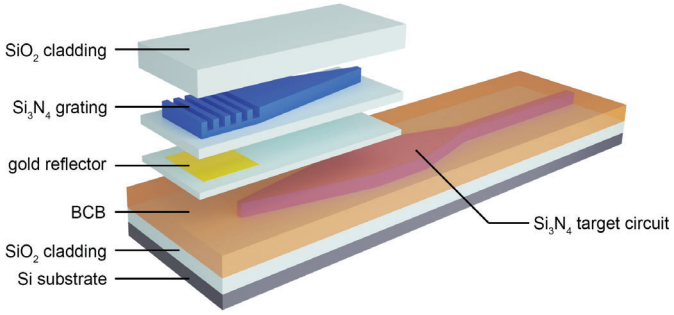

Figure 5.4: Schematics of a μTP grating coupler on a Si_3N_4 waveguide.

at the grating input. Once the fill factor is reduced to 0.5 along the propagation direction, it stays at this value afterward to diffract out as much power as possible.

As depicted by the k-vectors in Figure 5.5, the Bragg condition of the first-order diffraction is

$$\mathbf{k}_{out} \sin\theta + \mathbf{K} = \mathbf{k}_{in}. \tag{5.2}$$

Consider a uniform grating with period Λ, the Bragg condition can be written as

$$\frac{2\pi}{\lambda_c} n_{air} \sin\theta + \frac{2\pi}{\Lambda} = \frac{2\pi}{\lambda_c} n_{eff} \tag{5.3}$$

where λ_c is the center wavelength, θ the diffraction angle, n_{air} the refractive index of air, and n_{eff} the effective index of the grating. Thus the diffraction angle θ is given by

$$\sin\theta = n_{eff} - \frac{\lambda_c}{\Lambda}. \tag{5.4}$$

When the grating is apodized, the effective index changes with the fill factor. Therefore, to maintain the same diffraction angle θ, the period Λ should be varied accordingly as

$$\Lambda = \frac{\lambda_c}{n_{eff} - \sin\theta}. \tag{5.5}$$

A cross-section of the grating is sketched in Figure 5.6. The Si_3N_4 thickness is varied between the original thickness t_o and the etched thickness t_e. The effective index n_{eff} of each pitch is estimated as

$$n_{eff} = F \cdot n_o + (1 - F) \cdot n_e \tag{5.6}$$

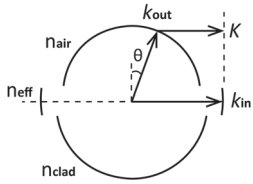

Figure 5.5: k-vector diagram of a grating

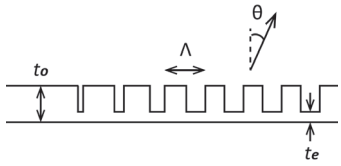

Figure 5.6: Sketch of the cross-section of the apodized grating

where n_o and n_e are the effective indices of waveguides with a thickness of t_o and t_e, respectively. These effective indices can be calculated numerically.

Combining the gold bottom reflector with the apodized grating, the proposed structure is expected to deliver high coupling efficiency on Si_3N_4 platforms. In the next section, we will discuss the procedure of numerically estimating the coupling efficiency and optimizing the structure.

5.3 Simulation of the coupling efficiency

Two components govern the efficiency of the μTP grating coupler: the grating with the bottom reflector and the adiabatic coupler. To reduce the complexity and running time of the simulation, the two parts are evaluated separately.

5.3.1 Coupling efficiency of grating couplers

The structure of the apodized grating coupler with bottom reflector is sketched in Figure 5.7. Several parameters control the coupling efficiency. The varying rate R of the fill factor along the propagation direction tailors the output profile.

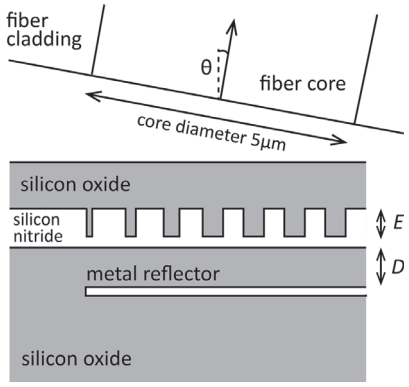

Figure 5.7: Sketch of the cross-section of the apodized grating with a metallic bottom reflector

The out-coupling power is also affected by the etch depth E. Moreover, the oxide thickness D determines the optimal wavelength of constructive interference. All these parameters should be swept to identify the optimal combination. The grating coupler is examined as an in-coupling device using Lumerical FDTD solutions. Two-dimensional (2D) FDTD simulations show the coupling efficiency from the input power of the optical fiber to the power in the channel waveguide. Besides R, E, and D, the fiber angle θ and position of the optical fiber should also be optimized.

The Si_3N_4 is assumed to have a refractive index of 1.93 around the target wavelength of 785 nm. This is measured using ellipsometry on Si_3N_4 thin films deposited via PECVD in the cleanroom of Ghent University. The thickness of Si_3N_4 is configured as 300 nm to match the thickness of the target circuit. The refractive index of SiO_2 is measured at around 1.44. The fill factor starts from 0.9 and gradually decreases to 0.5. The reflector is assumed to be a 100 nm-thick gold patch.

Fiber angle 5°

The fiber angle is first assumed to be 5°. As an initial guess from the target wavelength and angle, the oxide thickness is chosen as 140 nm. The optimization starts from a rough sweep of R and E. Figure 5.8(a) shows the numerically

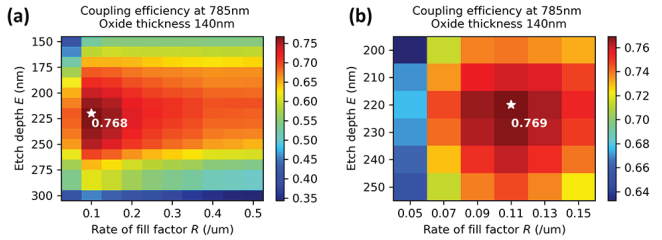

Figure 5.8: Estimated coupling efficiency at 785 nm for varied R and E, fiber angle 5°. The rough sweep shown in (a) is followed by a fine sweep shown in (b).

calculated coupling efficiency. The fiber position is swept simultaneously for each combination of R and E. Only the results from the optimal fiber positions are recorded. Then a fine sweep is performed around the optimal combination in the rough sweep ($R = 0.1\ \mu\text{m}^{-1}$, $E = 220$ nm). The results are presented in Figure 5.8(b), from which the final optimal combination is found at $R = 0.11\ \mu\text{m}^{-1}$ and $E = 220$ nm.

Then the oxide thickness D is swept from 100 nm to 250 nm while sweeping the fiber position. For each value of D, the optimal coupling efficiency is included in Figure 5.9(a). The highest power coupling efficiency is reached when the oxide thickness is 170 nm. For this grating coupler design with $R = 0.11\mu\text{m}^{-1}$, $E = 220$ nm and $D = 170$ nm, the coupling efficiency for a wavelength range from 740 nm to 840 nm is numerically estimated as shown in Figure 5.9(b). The coupling efficiency is 79.2% (-1.01 dB) at the wavelength of 785 nm. The 1-dB bandwidth is 30 nm.

Fiber angle 10°

10° is a more common fiber angle, which prevents back reflection into the waveguide when using the grating coupler for out-coupling. The same optimization process is carried out for optical fiber tilted at 10°. The results are shown in Figure 5.10. The coarse sweep of R and E is followed by a fine sweep around the optimal design, giving a combination of $R = 0.09\ \mu\text{m}^{-1}$ and $E = 290$ nm. Then the oxide thickness between the bottom reflector and the grating is varied from 100 nm to 250 nm. The maximum coupling efficiency of 64.9% (-1.88 dB) at 785 nm is found with 200-nm thick oxide. From the estimated coupling efficiency shown in Figure 5.10(d), the 1-dB bandwidth is 44 nm.

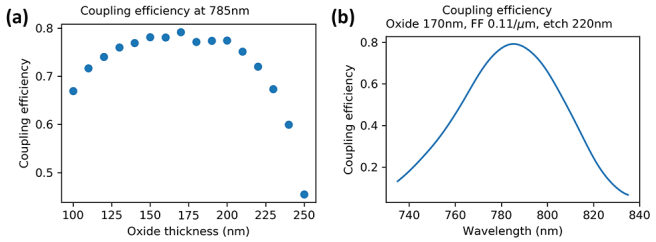

Figure 5.9: (a) Estimated coupling efficiency at 785 nm of a range of oxide thicknesses between Si_3N_4 and the reflector, fiber angle 5°. (b) The estimated coupling efficiency of the optimal design.

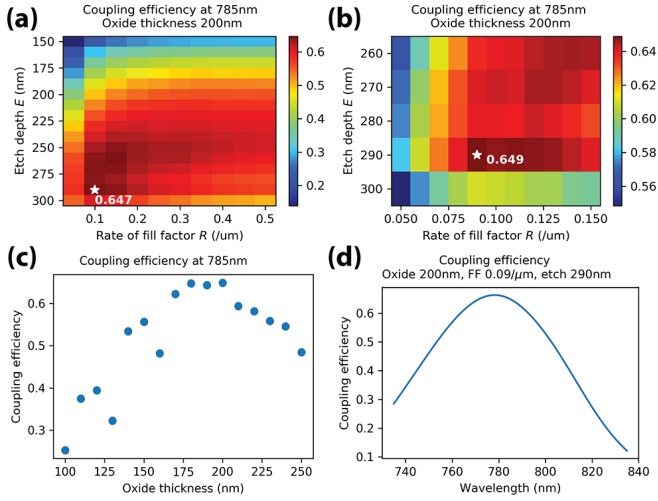

Figure 5.10: Estimated coupling efficiency with 10°-tilted fiber. (a) A coarse sweep of R and E. (b) A fine sweep of R and E. (c) A sweep of oxide thickness between the metal reflector and the grating. (d) The coupling efficiency of the optimal design.

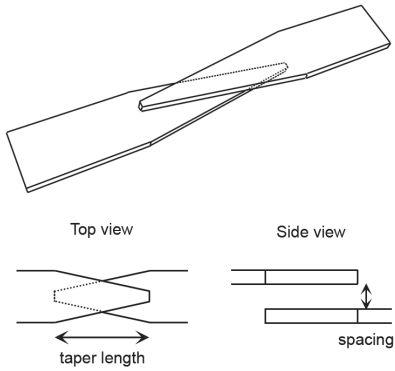

Figure 5.11: Sketch of the proposed adiabatic coupler in 3D, top view, and side view.

5.3.2 Coupling efficiency of adiabatic couplers

The adiabatic coupler consists of two tapers separated vertically, positioned in opposite directions, as sketched in Figure 5.11. The effective index gradually changes in both layers along the propagation direction. The coupling efficiency is determined by the taper length and the vertical spacing. Compared to directional couplers consisting of two parallel waveguides, adiabatic couplers generally require longer lengths. But the phase match condition between the two guiding layers is easier to achieve, relaxing the stringent requirement on design and fabrication variations. The misalignment tolerance improves with increased taper length.

The coupling efficiency of the adiabatic coupler is evaluated using the EME solver in Lumerical MODE solutions. It is mainly affected by the taper length and the spacing between the tapers. The latter is a summation of the oxide thickness D, the reflector thickness, the bottom oxide thickness on the source, and the thickness of BCB as shown in Figure 5.4(a). From previous experiments, the BCB thickness after printing is known to be around 50 nm. The bottom oxide thickness is set to 50 nm as well. Using also the oxide thickness $D = 170$ nm obtained in the grating coupler simulations, the total spacing is calculated as 370 nm. The two identical trapezoid tapers have base widths of 5μm and 0.15μm. The coupling efficiency for varied taper lengths is estimated as in Figure 5.12(a). It requires a minimum length of 150μm to achieve a coupling efficiency of 99% at the wavelength of 785 nm. The coupling efficiency of 150μm long adiabatic couplers is shown in

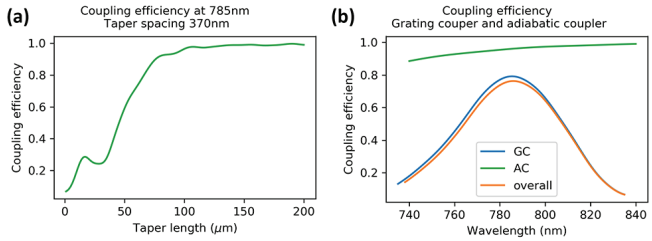

Figure 5.12: (a) Estimated coupling efficiency of adiabatic couplers with varied taper lengths. (b) Estimated coupling efficiency of the grating coupler (GC), 150μm long adiabatic coupler (AC), and the overall coupling efficiency of the μTP grating coupler.

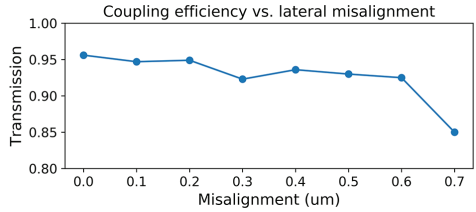

Figure 5.13: Estimated coupling efficiency of 150 μm long adiabatic couplers with varied misalignment perpendicular to the propagation direction.

Figure 5.12(b), together with that of the grating coupler and the overall structure. The overall efficiency at 785 nm is 78.4% (-1.06 dB) for a fiber angle of 5°.

Misalignment between the tapers may occur during μTP in translational or rotational manners. The effect of lateral misalignment relative to the propagation direction on the coupling efficiency of the 150μm long adiabatic coupler is presented in Figure 5.13. With a misalignment up to 0.6 μm, the change in coupling efficiency is negligible.

5.4 Fabrication of μTP grating couplers

5.4.1 Process flow

The process flow is performed and iterated in the cleanroom of Ghent University. The fabrication process of coupons is shown in Figure 5.14. It starts by depositing 180 nm silicon oxide (SiO_2) on a bare silicon (Si) sample. The purpose of this oxide layer is to separate the gold patch from the Si substrate, protect it during release, and support it afterward. After a recess with the same size and depth as the reflector is etched in the oxide layer using UV lithography and reactive ion etching (RIE), an 80 nm thick layer of gold is deposited using a metal evaporator. The gold reflectors are then defined through metal lift-off. The top surface becomes flat thanks to the recess. Gold markers for the following lithography steps are defined simultaneously. To improve the adhesion between gold and SiO_2, titanium layers of a few nanometers are deposited before and after the gold deposition. Then a layer of SiO_2 is deposited via plasma-enhanced vapor deposition (PECVD). Its target thickness may vary between 150 nm–200 nm depending on the coupling angle and wavelength. The guiding layer, 300 nm-thick Si_3N_4, is also deposited via PECVD. We first remove the Si_3N_4 and SiO_2 on top of the gold markers to image and align better. The shallow-etched gratings and deep-etched tapers are then defined by two separate steps of electron beam lithography (EBL) and RIE. To fill the grating lines and planarize the top surface, hydrogen silsesquioxane (HSQ) is spun onto the sample and cured at 400 °C. Then a 100 nm-thick layer of SiO_2 is deposited via PECVD.

The release process begins with a deep, dry etching around the coupons into the Si substrate. The coupons are anchored to the sample via tethers formed in this step. Then the sample is immersed in 5% tetramethylammonium hydroxide (TMAH), which etches the Si substrate with high selectivity against SiO_2 [109]. After the under-etching of the Si substrate, the coupons are ready for μTP.

The target sample also starts from a bare Si substrate. After depositing 3 μm of SiO_2 and 300 nm of Si_3N_4 via PECVD, waveguides with adiabatic tapers are etched in the Si_3N_4 layer using EBL and RIE. Before μTP, a thin layer of BCB (4022-35, diluted 1:3 using mesitylene) is spun onto the target sample at 3000 rpm for 40 seconds. It is later heated at 150 °C for 15 minutes to accelerate the evaporation of the solvent mesitylene and slightly cure the layer to prevent subsequent flowing. The BCB thickness is around 150 nm at this stage. Then the coupons are printed onto the ends of the waveguides. The BCB thickness is reduced to 50 nm beneath the coupon after printing. Figure 5.15 shows μTP grating couplers printed onto a target sample, observed under an optical microscope.

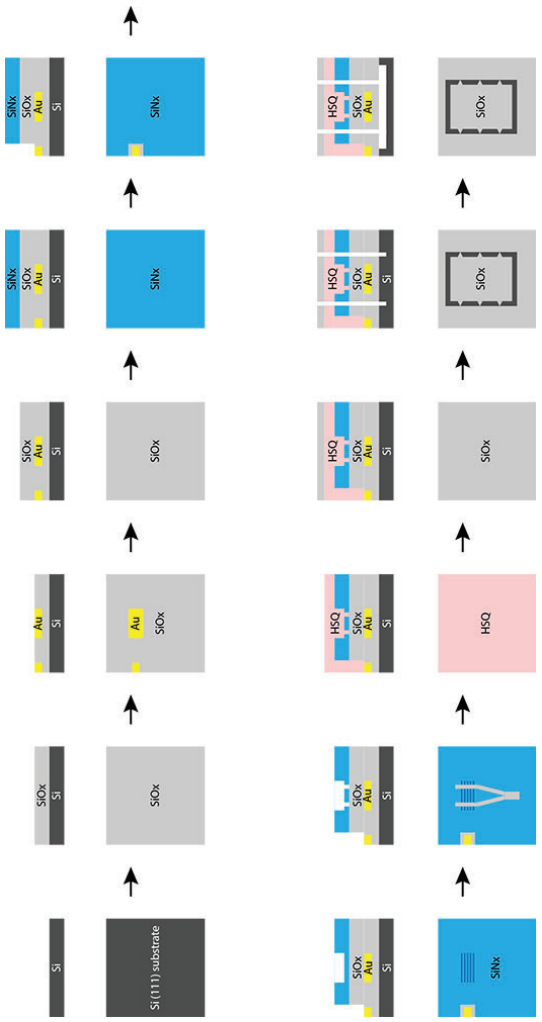

Figure 5.14: Process flow of coupons of coupon patterning and release. Cross-section and top-view are shown for each step.

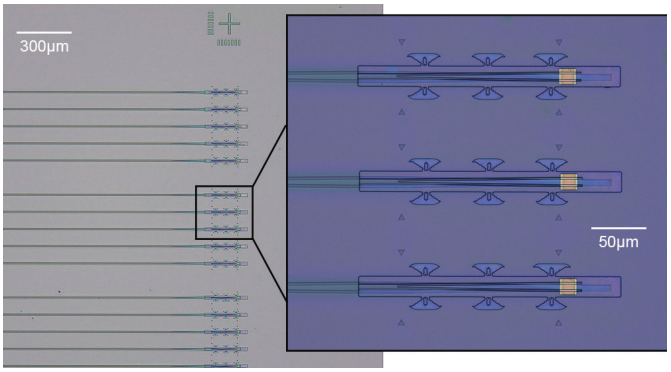

Figure 5.15: Grating couplers printed onto a target sample

5.4.2 Problems and solutions in process development

5.4.2.1 Top cladding of gratings

The gratings we fabricated using EBL and RIE have negatively sloped sidewalls, as depicted in Figure 5.16. The negative slope has two plausible origins. First, the electron beam resist employed (ARP 6200.09) exhibits a negative slope after developing if a high dose factor was used. In practice, we use a dose factor of 160 μC/cm^2 to fully expose the resist with a thickness of around 300 nm. With 50 kV voltage and a low current, this dose factor gave rise to the optimal balance between feature resolution and writing speed. However, as demonstrated in the datasheet of ARP 6200 resists [110], this dose factor is considered relatively high, and a noticeable undercut is introduced in the trenches. The slope affects the subsequent dry etching into the Si_3N_4 layer. Secondly, plasma etching can also introduce an undercut in trenches with a high aspect ratio, such as the openings in the apodized grating. In plasma etching, electrons are much lighter and faster than positive ions, hitting the wafer surface first and getting depleted. Ultimately, a sheath is formed near the wafer surface with only positive ions and neutrals, accelerating positive ions and redirecting the electrons. Therefore, the electrons that penetrate the sheath are decelerated, and their angular distribution is wider compared to the positive ions. In the high-aspect-ratio trench, the electrons are distributed evenly on the sidewalls and bottom, while the positive ions are headed directly to the bottom. Eventually, the positive charge on the bottom surface must be

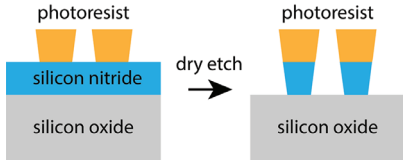

Figure 5.16: The effect of photoresist sidewall slope and RIE etching on Si_3N_4 waveguides.

reduced to achieve a steady state by deflecting the positive ions toward the sidewall. With extra bombardments and reactions on the sidewall close to the bottom, an undercut is formed, with the severity growing with the aspect ratio [111].

In practice, it is common to coat Si_3N_4 gratings with a top cladding for planarization and protection. The top cladding is usually deposited via atomic layer deposition (ALD) and PECVD of SiO_2. Both methods have excellent conformality. However, as shown in Figure 5.16, a bottleneck is formed between two adjacent grating teeth due to the negative sidewall. Conformal deposition of SiO_2 closes the bottleneck first and seals an air bubble underneath, as shown in Figure 5.17(a)-(c). It changes the effective index of the grating randomly and induces additional scattering loss. The overall coupling efficiency is significantly reduced.

One solution is to use spin-on dielectric materials as the top cladding. HSQ is an inorganic oligomer extensively investigated as a low-k spin-on dielectric [112–115]. After thermal curing, HSQ can form a three-dimensional network structure of Si, oxygen, and hydrogen atoms. Looking for good mechanical integrity and chemical resistance, thermal curing of HSQ is studied in the temperature range up to 480°C. [114–116] As stated by Siew *et al.* [114], the HSQ thermal curing takes four stages as listed in Table 5.1. At an optimal temperature of around 400°C, the HSQ forms a mixture of silsesquioxane and silicon-rich oxide with the lowest refractive index.

Temperature range	Main reaction
Room temperature – 200°C	Loss of carrier solvent
250 – 350°C	Network redistribution, $SiO_{4/2}$ formation
350 – 435°C	Network redistribution, Si-H thermal dissociation
$>$ 435°C	Collapse of porous network

Table 5.1: Stages of HSQ thermal curing [114]

The commercial product of HSQ usually uses methyl isobutyl ketone (MIBK) as a carrier solvent, which volatilizes rapidly during spin-coating and leaves a

Orientation	Etch rate (μm/min)
(100)	0.603
(110)	1.114
(111)	0.017

Table 5.2: Orientation-dependent etch rates in 20 wt% TMAH at 80°C from [119]

planar surface. In our experiments, the HSQ resin is spun onto the source sample at 5000 rpm targeting a thickness of around 400 nm. After spin-coating, the sample is heated at 120°C and 220°C on a hotplate to remove the solvent as much as possible. Then the sample is cured at 400°C in a nitrogen-flow environment for two hours. Compared to ALD and PCVD SiO_2, cured HSQ has a lower refractive index of 1.385 at the wavelength of 785 nm. The cross-section of a grating with HSQ cladding is shown in Figure 5.17(d). No distinct air bubbles can be seen, and the top surface is planarized. It solves the problem of applying top cladding to bottlenecked gratings.

It is worth noting that the cured HSQ thin film is resistant to TMAH used in under-etching but not resistant to the developer AZ400K used in UV lithography, which is a potassium-based, alkaline solution. Therefore, after HSQ application and before dry etching into the Si substrate, a thin layer of SiO_2 is deposited via PCVD to protect the HSQ film during the subsequent UV lithography and deep etching. This step is included in the process flow shown in Figure 5.14.

5.4.2.2 Etching of Si substrate

The grating couplers are released from the substrate by etching the Si substrate with TMAH solution, which is also used as a developer in photolithography. The alkaline aqueous solution of TMAH etches Si with higher selectivity against SiO_2 than KOH solutions [117]. Therefore, TMAH is more suitable for the proposed grating couplers. Nonetheless, on monocrystalline Si substrates, the etching with TMAH is highly anisotropic [118, 119]. As stated by Shikida *et al.* [119], the etch rates in different orientations are shown in Table 5.2.

As shown in the process flow in Figure 5.14, the Si substrate is exposed by vertical dry etching around the device before releasing the device from the source substrate. Then the trenches are filled with TMAH to etch the Si substrate horizontally. On Si (100) wafers, the horizontal etching is prohibited by the (111) planes as sketched in Figure 5.18. The thin film is not separated from the substrate. On the contrary, the etching on Si (111) wafers is mostly horizontal until it is stopped by the (111) planes. It can remove the Si substrate underneath the thin film and

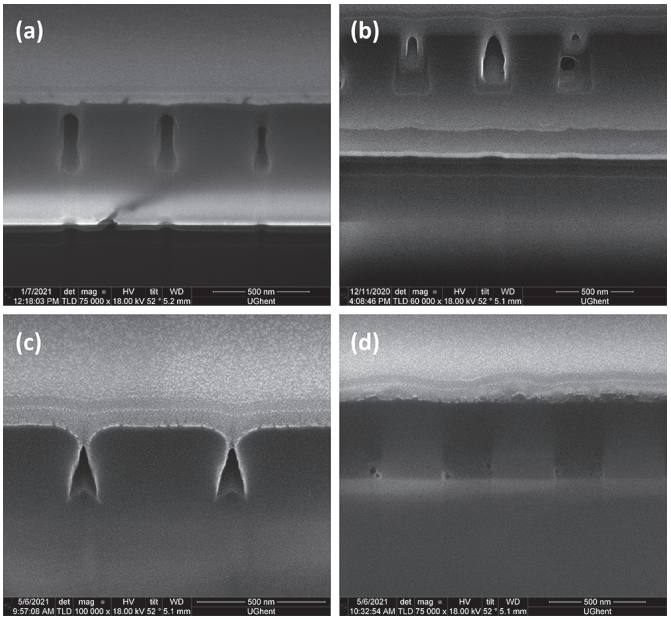

Figure 5.17: Cross-sections of the Si_3N_4 gratings under a scanning electron microscope. Top oxide cladding is deposited by (a) ALD, (b) ALD, (c) PCVD, and (d) spin-coating HSQ, respectively.

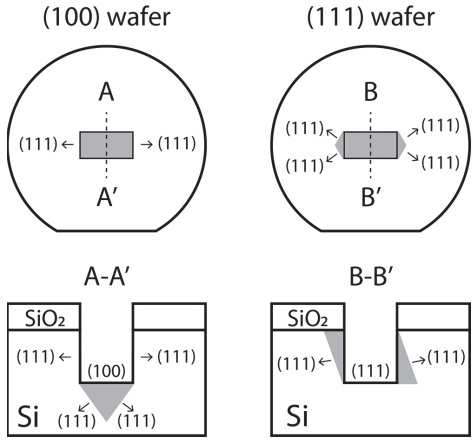

Figure 5.18: Schematics of Si (100) and (111) wafers after anisotropic wet etching. The rectangles in the top views represent dry-etched openings into the Si substrate, which are also the vertical trenches in the cross-sections. The shadowed area represents the part of Si that is removed by TMAH.

prepare it for the subsequent μTP.

The orientation of source devices on Si (111) wafers affects the etching time and the outcome of the release. Figure 5.19 demonstrates released grating couplers in different orientations, denoted by the (111) plane hexagons in the figures. The devices are enclosed in a rectangular shape, namely a coupon in μTP. The released coupons are bent by the stress in PECVD SiO_2 and Si_3N_4 thin films, inducing interference rings on the coupons. With the orientation in Figure 5.19(a), the under-etching progresses perpendicular to the tapers, where the etching time is the shortest. The etch rate in this direction is around 1 μm/min in 5% TMAH at 70°C. The released area extends into the surroundings, leaving a larger suspended area. It leads to further bending of the thin film and imposes an extra force on tethers during pick-up. The yield is hence reduced. If the coupons are rotated by 90° as shown in Figure 5.19(b), under-etching is limited to the horizontal direction. The etching in the perpendicular direction is limited. Therefore the suspended area is smaller and less susceptible to bending. The yield is significantly improved. However, as the etching progresses in the horizontal direction, it requires a much longer etching time.

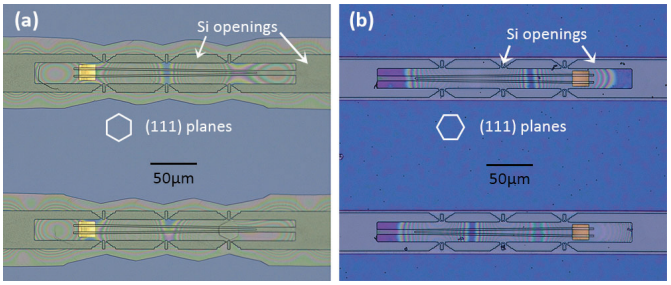

Figure 5.19: Coupons released from the Si (111) substrates, aligned to different crystal orientations. (a) The suspended area is larger and more susceptible to bending. (b) The suspended area is limited to only necessary.

The bending of coupons after release may cause partial or complete collapse onto the Si substrate. For instance, it can be seen from the solid purple- and blue-ish colors on the left and right ends of the coupons in Figure 5.19(b). The larger the collapsed area is, the more difficult it is to pick up these coupons. Moreover, the bottom surface of coupons may be contaminated. Besides optimizing the PECVD recipe to reduce stress, the condition can be improved by etching deeper into the Si substrate to reserve more space for bending.

5.5 Measurements of coupling efficiency

We characterize the coupling efficiency of the μTP grating couplers printed onto Si_3N_4 waveguides. The coupling loss of the grating coupler and the adiabatic couplers are treated as a whole, as they are both necessary parts of the proposed device. Light with a wavelength from 780 nm to 880 nm is coupled into the waveguide through a single-mode optical fiber tilted at 10° with a mode field diameter of 5 μm. We first measure the insertion loss of waveguides with μTP grating couplers on both ends.

The insertion loss consists of the coupling loss at the two ports and the propagation loss. The propagation loss is estimated from the change of scattered intensity along the waveguide. It is recorded by a camera looking at the sample from above. Some example pictures are included in Figure 5.20. The decay rate of the intensity along the waveguide represents the propagation loss of the waveguide. The periodic peaks in Figure 5.20 correspond to the stitching error in electron beam lithography,

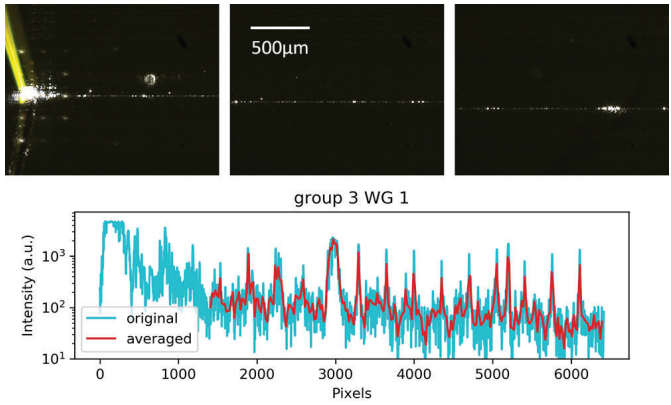

Figure 5.20: Above: camera pictures of light scattered by the waveguide. Below: the scattered intensity recorded along the waveguide.

which are 500 μm apart. By measuring three waveguides on the sample, the average propagation loss is 8.5$\pm$0.3 dB/cm. This is measured on 300-nm thick, 800-nm wide, low-frequency PECVD Si_3N_4 waveguides fabricated using EBL.

We obtain an average coupling efficiency between the two grating couplers on one waveguide by subtracting the propagation loss from the insertion loss. Figure 5.21 shows the coupling efficiency measured with standard and μTP grating couplers. The μTP grating couplers have an etch depth of 230 nm and a fill factor varied at 0.11 μm^{-1}. When the fill factor reaches 0.5, the pitch is 616 nm. Six of them are printed onto three identical waveguides. The colored dots in Figure 5.21 show the average coupling efficiency on each waveguide. As a comparison, we include the measured coupling efficiency of standard grating couplers (black dots in Figure 5.21), which are fully etched on the input and output of the waveguides with a pitch of 610 nm and a fill factor of 0.5. The highest coupling efficiency of the μTP grating couplers is found around the wavelength of 840 nm as -2.1 dB, while the average efficiency on the three waveguides is -4.0 dB. The maximum and average coupling efficiency are both 3 dB better than the efficiencies measured with the standard grating couplers, which comply with the simulation.

It needs to be noted that the center wavelength is shifted by over 50 nm compared to the design. Multiple factors may have contributed to the problem. First, the properties of Si_3N_4 and SiO_2 thin films deposited using PECVD in our cleanroom

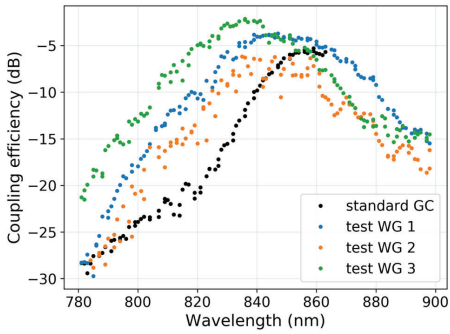

Figure 5.21: Coupling efficiency of μTP and standard grating couplers in the wavelength range from 780 nm to 880 nm.

change gradually with time due to changed deposition conditions. It affects the effective index of the grating and the effective distance between the grating and the reflector. Second, due to the short length of the waveguides, we do not have sufficient space to tilt the fiber at 5° without the bulky fiber holders on top colliding, which is the design angle for most devices. By increasing the tilt angle to 10°, the center wavelength also increases. Finally, uncertainties in other properties, such as HSQ thickness and index, may also affect the center wavelength and efficiency.

5.6 Conclusion

In this chapter, we present a micro-transfer-printed Si_3N_4 grating coupler that can boost the coupling efficiency on Si_3N_4 platforms. It improves the coupling efficiency through a metallic bottom reflector and apodized grating. Thanks to the micro-transfer-printing technology, modifications of the existing platform are not necessary when applying such grating couplers. We first numerically optimize the grating parameters and layer thicknesses for the wavelength of 785 nm. Then a process flow is developed in the UGent cleanroom to fabricate the optimal device. The best coupling efficiency is measured as -2.1 dB at a wavelength of 840 nm, 3 dB better than conventional grating couplers. It can significantly increase the coupling efficiency in waveguide-enhanced Raman spectroscopy and improve the detection limit.

6

Optical phased array spectrometer

For various fields, including Raman spectroscopy, optical spectrometers are essential to capture spectral information in the output signal. With the development of sensors based on photonic integrated circuits (PICs), there is a growing need for integrated spectrometers with broad bandwidth, good resolution, and sufficient detection limit. Candidate spectrometers have been developed, such as arrayed waveguide grating (AWG) [120–122] and Fourier-transform spectrometers (FTS) [123–125]. However, they both suffer from inevitable trade-offs among spectral range, resolution, and footprint. An adequate integrated spectrometer is still in demand for on-chip Raman spectroscopy.

This chapter presents a broadband spectrometer based on an optical phased array (OPA) on a Si_3N_4 platform. The OPA consists of arrayed waveguides with a fixed delay length and grating couplers for off-chip coupling. The structure is previously described by Van Acoleyen *et al.* as a beam steering component on SOI platforms [126]. It is also employed for beam steering applications on Si_3N_4 platforms [127, 128]. Each wavelength dispersed by the OPA corresponds to a unique emission direction. With the Fourier-space imaging technique, each emission direction is imaged to a point with a unique coordinate in the back focal plane of the collecting lens. A spectrum of the input signal can be reconstructed after imaging the back focal plane with a camera. One of the advantages is the ease of using off-the-shelf, cooled image sensors, which is not convenient with AWGs.

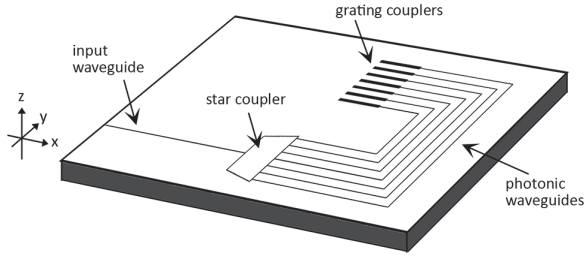

Figure 6.1: Schematic of the OPA

It is also more convenient to integrate free-space filters with a high rejection ratio for the pump wavelength into the system. With this novel configuration of a hybrid guided wave and free-space optical system, we can realize a compact spectrometer with good performance. The on-chip footprint can be reduced to 0.1 mm^2. It offers a much better resolution (0.5 nm) than FTS with a similar footprint [124].

6.1 Working principle

6.1.1 Dispersion mechanisms

As shown in Figure 6.1, the OPA consists of three fundamental sections: an input waveguide, a star coupler, and an array of photonic waveguides connected to grating couplers. In this work, a similar structure is implemented on a Si_3N_4 platform. Light is coupled into the input waveguide and then split into the waveguide array through the star coupler. The arrayed waveguides have ascending lengths with a fixed length difference. At the end of each waveguide, a grating coupler is etched to diffract light out of the sample plane. The gratings are separated from each other by a fixed spacing.

As discussed in section 5.2, the Bragg condition of the first-order diffraction of a grating is given by

$$\mathbf{k}_{out} \sin\theta_x + \mathbf{K} = \mathbf{k}_{in}, \tag{6.1}$$

where θ_x is the angle from the surface normal. For a uniform grating with a period Λ, it can be written as

$$\frac{2\pi}{\lambda} n_{air} \sin\theta_x + \frac{2\pi}{\Lambda} = \frac{2\pi}{\lambda} n_{gr} \tag{6.2}$$

where λ is the wavelength, and n_{gr} the effective index of the grating. Therefore, the diffraction angle θ_x is given by

$$\sin\theta_x = \frac{\lambda}{\Lambda} - n_{gr} \tag{6.3}$$

which changes with the input wavelength. The steering speed can be calculated as

$$\frac{d(\sin\theta_x)}{d\lambda} = \frac{1}{\Lambda} - \frac{dn_{gr}}{d\lambda}. \tag{6.4}$$

The dispersion of the effective index of the grating n_{gr} can be estimated numerically. For a typical SiO_2-cladded Si_3N_4 grating with a period of 500 nm, a fill factor of 0.5, and an etch depth of 200 nm, the steering speed is calculated as 2.3×10^{-3}/nm, equivalent to 0.13°/nm.

Meanwhile, light is also steered in the y-direction with an angle θ_y due to the arrayed waveguides. As depicted in Figure 6.2, an array of emitters with a fixed phase delay $\Delta\varphi$ can form a combined wavefront of a quasi-plane wave. From Figure 6.2, the propagation direction θ_y is related to the phase delay $\Delta\varphi$ as

$$\Delta\varphi = \frac{2\pi}{\lambda} d\sin\theta_y + m\cdot 2\pi \tag{6.5}$$

where d is the center-to-center distance between emitters, and m is an integer. In our design, the phase delay $\Delta\varphi$ is determined by the delay length ΔL of arrayed waveguides as

$$\Delta\varphi = \frac{2\pi}{\lambda} n_{eff}\Delta L \tag{6.6}$$

where n_{eff} is the effective index of the waveguides. From equation (6.5) and (6.6), the steering angle in y-direction is deduced as

$$\sin\theta_y = \frac{n_{eff}\Delta L}{d} - m\lambda. \tag{6.7}$$

The steering speed is given by

$$\frac{d\theta_y}{d\lambda} \approx \frac{d\sin\theta_y}{d\lambda} = \frac{dn_{eff}}{d\lambda}\frac{\Delta L}{d} - \frac{m}{d} \tag{6.8}$$

when the steering angle θ_y is small. To give a typical value of the steering speed, we first need to establish typical values of ΔL, d, and m.

The far-field distribution in the y-direction can be calculated by summing the far-field of all grating couplers considering the phase difference. The Fraunhofer diffraction formula calculates the far-field $e(y_1)$ from the radiation pattern $e(y_0)$ as

$$e(y_1) = \frac{je^{-jkz_0}}{\lambda z_0} e^{-\frac{jk}{2z_0}y_1^2} \iint_{-\infty}^{+\infty} e(y_0) e^{j\frac{2\pi}{\lambda z_0}y_1 y_0} dy_0 \tag{6.9}$$

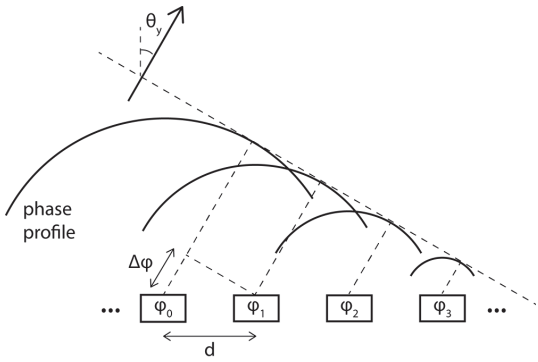

Figure 6.2: Phased array with a linear array of apertures

where y_0 represents the position of the grating, y_1 the position on the far-field, and z_0 the distance from the far-field. The grating can be approximated to a Gaussian aperture with a beam width ω in the y-direction as follows:

$$e(y_0) = e^{-\frac{y_0^2}{\omega^2}}, \tag{6.10}$$

and

$$e(y_1) = \frac{je^{-jkz_0}}{\lambda z_0} e^{-\frac{jk}{2z_0}y_1^2} \omega^2 e^{-(\frac{\pi\omega}{\lambda z_0})^2 y_1^2} \tag{6.11}$$

The overall far-field of all grating couplers is

$$e(\mathbf{r}) = \sum_{n_y=0}^{N_y-1} A_y e^{j\beta_y} F(\theta_y) \frac{e^{-jk_0|\mathbf{r}-\mathbf{s}_y|}}{|\mathbf{r}-\mathbf{s}_y|} \tag{6.12}$$

where A_y is the field amplitude, β_y the relative phase of each grating, F the far-field of each element, k_0 the free-space wave vector, and $\mathbf{s}_y$ the position of each grating. When the far-field plane is far enough from the sample so the relative position difference can be ignored, the distance factor $|\mathbf{r}-\mathbf{s}_y|$ can be approximated to a constant R for all gratings. Then the overall far-field can be written as

$$e(\mathbf{r}) = F(\theta_y) \frac{e^{-jk_0R}}{R} \sum_{n_y=0}^{N_y-1} A_y e^{j\beta_y} e^{-j\mathbf{k}\cdot\mathbf{s}_y}. \tag{6.13}$$

The first two terms are the far-field of one element, while the terms in summation consider the distribution of all gratings. Using equation (6.13), we can estimate

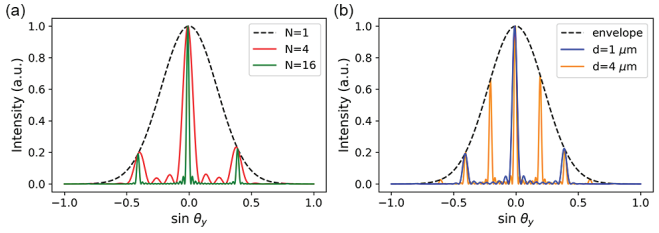

Figure 6.3: (Left) Far-field of different number of gratings with a width of 0.8 μm at the wavelength of 0.8 μm. (Right) Far-field of 8 gratings with different center-to-center distances at the wavelength of 0.8 μm.

the far-field distribution of a given array of waveguides and gratings. Figure 6.3 shows the effect of the number of gratings N_y and center-to-center spacing d on the far-field. On the one hand, the overall aperture becomes larger with more gratings, and its Fourier transform becomes narrower. Better spectral resolution can be achieved by including more gratings at the expense of a larger footprint. On the other hand, the angular distance between adjacent orders is increased when the spacing d is decreased. Setting d as low as possible allows us to concentrate more intensity on the main order and avoid undesirable lobes. However, two waveguides or gratings cannot be put unlimitedly close before inter-waveguide coupling occurs. From simulations, we conclude that the minimum d is around 1.5 μm.

It is also essential to keep the waveguides sufficiently separated during the propagation from the star coupler to the gratings to avoid inter-waveguide coupling. For 800 nm wide Si_3N_4 waveguides, the typical bend radius is over 50 μm. In practice, we found out that the waveguides in the array should be separated by at least 9 μm to avoid inter-waveguide coupling and phase noise. To fulfill that requirement, the delay length difference ΔL between each waveguide should be at least 25 μm. At the target wavelength of 800 nm, it gives rise to an order m around 50. Putting these typical values of d, ΔL, and m in equation (6.8), the steering speed in the y-direction is about 0.041/nm, i.e., 2.3°/nm. It is much faster than in the x-direction, as it is steered from a much higher order.

The two steering mechanisms in x- and y-directions help to form a two-dimensional OPA. Each wavelength is dispersed to a unique direction characterized by (θ_x, θ_y). Therefore, by examining the far-field of an unknown signal emitted by the OPA, we can calculate the wavelength and intensity of each spectral component. This is the function of a spectrometer.

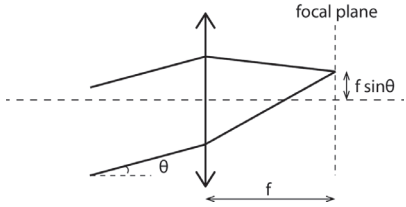

Figure 6.4: Sketch of basic Fourier imaging

6.1.2 Fourier imaging technique

Consider the incidence of a parallel beam onto a simple convex lens. The beam is focused to a point on the back focal plane as sketched in Figure 6.4. The focal length f and incident angle θ determine its distance from the center. Therefore each direction of injection is imaged as a point on the back focal plane, i.e., the Fourier plane. To collect a larger part of the far-field, it is necessary to use lenses with larger numerical aperture (NA). One common choice is a high NA microscope objective (MO). However, the back focal plane of our MO lies inside its housing. It can be imaged onto an image sensor through a two-lens system, as shown in Figure 6.5. By adding an extra lens (L3) between the camera and the last lens (L2), the setup can also image the real space of the sample.

6.1.3 Spectral range and resolution

As shown in Figure 6.3, there are multiple local maxima in the far-field of an OPA. The main order of one wavelength λ_1 may appear at the same θ_y as the second order of λ_2. It potentially limits the measurable spectral range of the OPA spectrometer. Nonetheless, the slower tuning in the x-direction assigns different θ_x to the two wavelengths. Figure 6.6 plots the calculated Fourier space of an OPA. It has 16 waveguides in the array with a delay length of 25 μm, and the grating couplers are separated by 1.6 μm. As annotated in the figure, the spots correspond to varied wavelengths from 820 nm to 860 nm with a 2 nm step size. Different colors represent different orders of the OPA. The crossbars indicate the FWHM in the x- and y-direction. The circle shows the field of view in the Fourier space, the radius of which is determined by the NA of the MO. It can be seen that all light spots are resolved nicely in both the x- and y-direction. Therefore, the multiple orders from the OPA do not impose restrictions on the spectral range. In this case, the spectral range is primarily limited by the MO's NA and the grating couplers' transmission. From our simulation of a 300 nm thick Si_3N_4 grating with a period

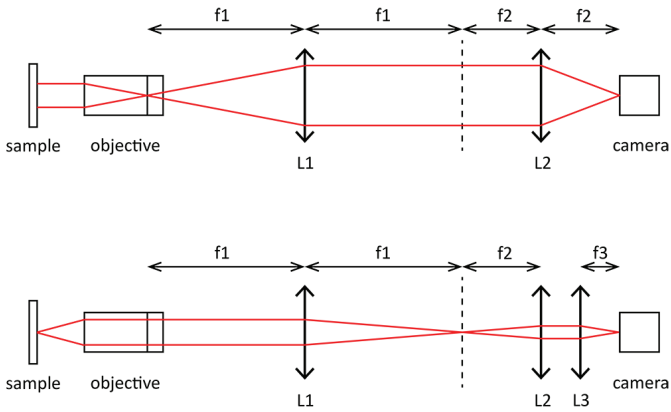

Figure 6.5: Sketch of the Fourier imaging setup. The upper setup images the Fourier plane of the sample onto the camera. By adding an extra lens (L3), the setup can also image the real space.

of 500 nm, a fill factor of 0.5, and an etch depth of 200 nm, the spectral range can easily cover 200 nm with a MO with 0.28 NA.

As the steering is faster in the y-direction, the resolution is defined by the FWHM in this direction and the angular dispersion. It is affected by the number of gratings N_y and the spacing between gratings d as follows:

$$\Delta\theta_y \approx \frac{\lambda}{N_y d} \tag{6.14}$$

With 16 waveguides separated by 1.5 μm, the FWHM is 1.9° at a wavelength of 800 nm. To convert the angular span into wavelengths, we need to use angular dispersion, roughly 2.3°/nm as calculated in section 6.1.1. Therefore, the spectral resolution is about 0.8 nm with the given OPA.

6.2 Characterization of the OPA spectrometer

6.2.1 Fabrication and measurement

We fabricated the OPAs on a 300 nm Si_3N_4 platform from IMEC using EBL and RIE. Figure 6.7 shows the top view of an OPA with 32 waveguides in the array.

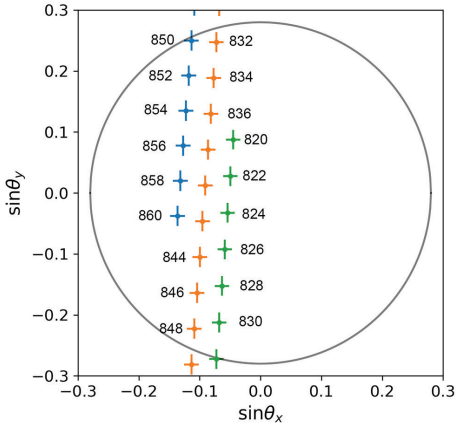

Figure 6.6: Calculated Fourier space of an OPA with 16 waveguides.

The photonic structure has a small footprint of about 0.56×0.22 mm^2. The entire structure is fully etched with an etch depth of 300 nm, including the grating couplers. The strip waveguides are 800 nm wide. Light is coupled into the PIC through a 3 μm-wide edge coupler, tapered down to the strip waveguide. Then the 800 nm wide waveguide is tapered again to 3 μm to connect with a star coupler, where a slab mode is excited. At the end of the star coupler, 32 3 μm wide tapers are placed on an arc to collect light and couple it into the waveguide array. The bend radius is 50 μm. The delay length different ΔL is 24.9 μm. And the spacing between the gratings is 1.6 μm.

The sample is tested on the setup sketched in Figure 6.8. We combine the output of a tunable laser and a broadband supercontinuum light source through a 50:50 fiber splitter. It is converted to a collimated beam in free space through a collimator. A half-wave plate and a polarizing beam splitter (PBS) are employed to excite only the TE mode. Then the light is split through a 50:50 splitter. Half of it goes to an optical spectrum analyzer (OSA) through a single-mode fiber (SMF). The remaining half is coupled into the waveguide through an objective (10×, NA=0.28) and the edge coupler. The light emitted from the chip is imaged onto a camera through a Fourier imaging system. The camera (Thorlabs DCU224M) has a sensor size of 6.0×4.8 mm^2 with square pixels of 4.65 μm wide. The lenses have focal lengths of 200 mm and 100 mm, respectively. The resulting magnification is 0.5× from the objective pupil to the camera.

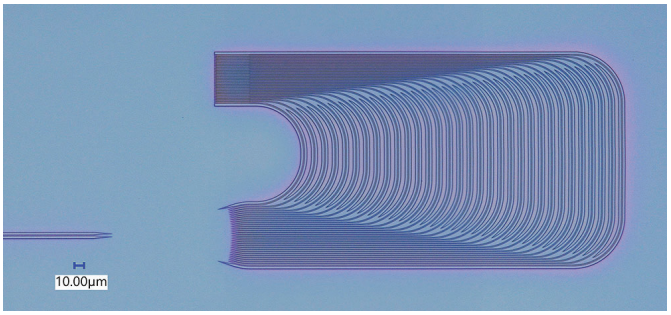

Figure 6.7: Top view of a fabricated OPA under an optical microscope

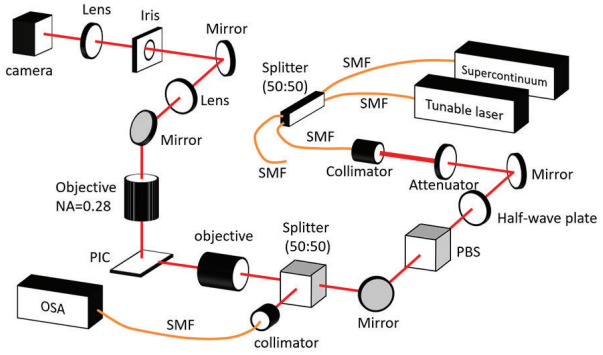

Figure 6.8: 3D schematics of the experiment setup for the characterization of OPA spectrometers

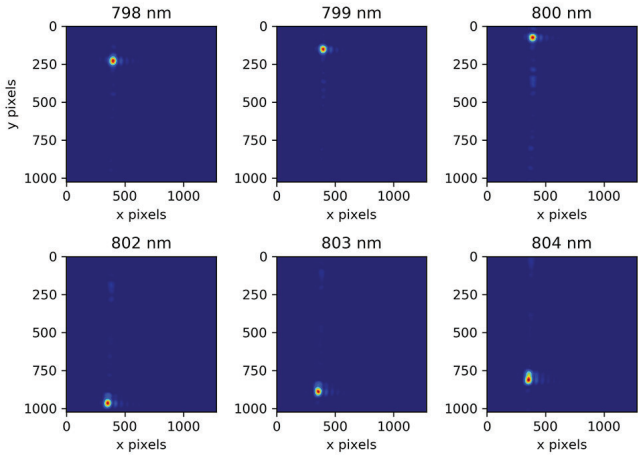

Figure 6.9: Far-field pattern of the OPA of different wavelengths, captured with a camera. Pseudo-colored to show intensity.

To reconstruct a spectrum from the far-field image on the camera, we must know the relation between wavelengths and the far-field coordinates. For such a calibration, we couple only the tunable laser into the waveguide and tune the wavelength from 750 nm to 850 nm with a step size of 1 nm. We record the laser wavelength, laser power before the input objective, and the far-field image on the camera. For instance, Figure 6.9 shows the far field of six different wavelengths. Fast steering in the y-direction can be observed. The coordinate of each light spot can be represented by the x- and y-pixel numbers at the spot center. Figure 6.10 shows the center x- and y-coordinates separately for all wavelengths tested. Theoretically, the x-position should vary slowly and smoothly with wavelength. However, a jump can be observed at the wavelengths where a new order appears in the y-direction. This results from a rotation of the sample with respect to its normal axis, whose x-axis does not align with the horizontal edge of the field of view. As long as the position of each wavelength is well recorded, the rotation does not affect the quality of spectrum reconstruction.

It is not sufficient to reconstruct a spectrum knowing only the relation between position and wavelength. It is also necessary to acquire the relation between the input and output intensities. During the wavelength tuning, the final readout at the center pixel is recorded as the output intensity of the optical system with a unit of

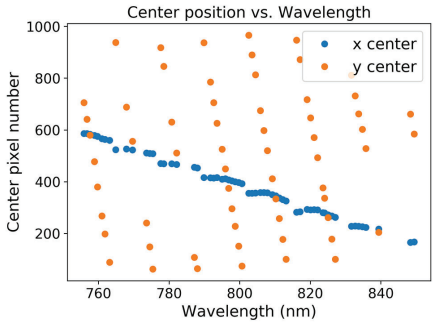

Figure 6.10: Center pixel numbers in x- and y-direction of varied wavelength, respectively.

electron counts. We define a conversion coefficient (counts/mW) that is the product of the readout over the input laser power. It can be calculated by dividing the readout by the input power measured at the beam splitter before the input objective. Figure 6.11 shows the conversion coefficient acquired in the measurement. It is affected by several components in the system. For instance, from the simulated transmission of the grating couplers presented in Figure 6.12(a), we observe two dips: the one around 760 nm corresponds to back reflection, while the one around 810 nm corresponds to interference with reflection from the Si substrate. Moreover, the normalized intensity of the primary peak of the OPA also varies with wavelength, as shown in Figure 6.12(b). Consider one main order of the OPA, its output intensity changes as the output angle changes. The angular intensity is determined by the far-field of one grating. Therefore, by changing the wavelength and sweeping the angle from one side of the normal direction to another, the intensity increases and then decreases. When this main order decreases to a side, the following order becomes stronger, substituting the previous main order. It induces the abrupt increases in Figure 6.12(b). Together with a decrease in the camera's quantum efficiency indicated in Figure 6.12(c), we can numerically calculate the conversion coefficient of the system. Figure 6.12(d) compares the numerical and experimental conversion coefficients. A good agreement in the general tendency can be observed. The cause of the minor spikes remains unclear.

It is possible to optimize and simplify this calibration process. For example, both the x- and y-positions should vary linearly with wavelength. If the camera is well aligned with the OPA, measuring the far field positions of a few wavelengths is sufficient to deduce the positions of the rest from a linear fitting. The conversion coefficient can be estimated theoretically with a better understanding of the fine

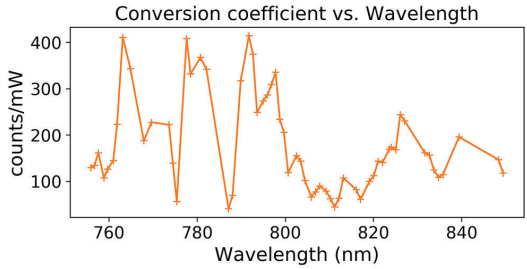

Figure 6.11: Conversion efficiency of the OPA spectrometer as a function of wavelength

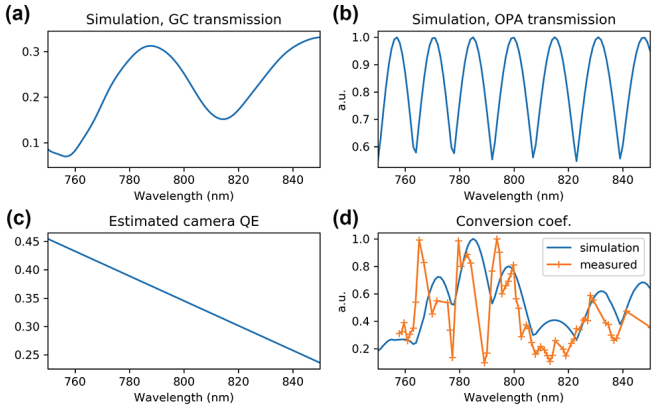

Figure 6.12: Simulated transmission of (a) the grating couplers and (b) the optical phased array. (c) Quantum efficiency of the camera, estimated from the datasheet. (d) The conversion coefficients were obtained from simulation (blue) and experiment (orange).

features. Then there is no need to record the output of all wavelengths with high resolution. The calibration time can be reduced, and the instrumental requirement can be relaxed.

6.2.2 Result: measured spectrum of laser and supercontinuum light sources

The broadband supercontinuum light and the tunable laser are simultaneously coupled into the sample as a test signal. Figure 6.13 demonstrates the far-field image on the camera. The far-field can be converted to a spectrum using the calibration data acquired in the previous section. The result is shown in Figure 6.14 with blue dots. The same signal is simultaneously measured by the OSA presented in Figure 6.8 as a reference. It is also included in Figure 6.14 in an orange line. Good agreement in wavelength and relative intensity can be seen. The deviation between the two spectra mainly exists in lower intensities, especially where the conversion coefficient is low. It is a result of decreased SNR. There are several methods to improve it, e.g., increasing the signal intensity by longer exposure on a camera with a higher dynamic range. Repeated, averaged measurements of the conversion coefficient may also improve the accuracy.

In this measurement, the average steering speed in the y-direction is about 81 pixels/nm. The FWHM spot width in the y-direction is 44 pixels on average. Therefore, the average spectral resolution is about 0.5 nm, agreeing with the theoretical calculation of a 32-waveguide OPA. The spectral range of 750–850 nm is determined by the tuning range of the tunable laser, which limits the calibration. It can be further expanded by replacing the light source in calibration and using an objective with a larger NA. However, it is worth noting that imaging a larger NA onto the same camera may reduce the spot size to be comparable with the pixel size. In this case, we may be forced to increase the spot size and reduce the spectral resolution to maintain the imaging quality. It can be mitigated by increasing the angular dispersion, using a larger image sensor, or reducing the pixel size.

The next step is to measure the Raman signal generated from a photonic waveguide. First, a pump-rejection filter must be added on the chip or in free space before the camera. Second, a cooled camera is required to detect the weak signal. From our calculation, a camera cooled to -20°C can already provide acceptable SNR. In conjunction with the on-chip dispersive OPA, a compact, sensitive spectrometer can be realized for the WERS sensor.

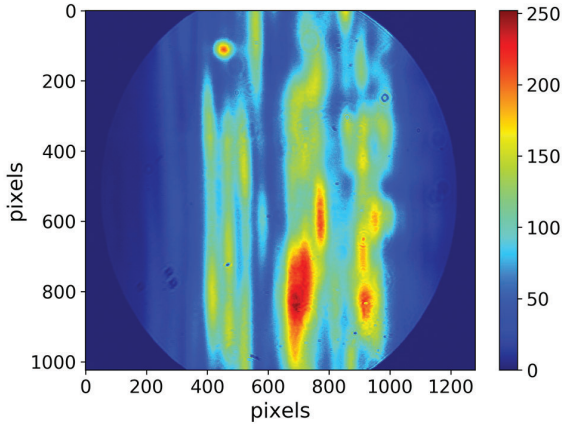

Figure 6.13: Far-field image of a test signal consisting of a broadband source and a laser

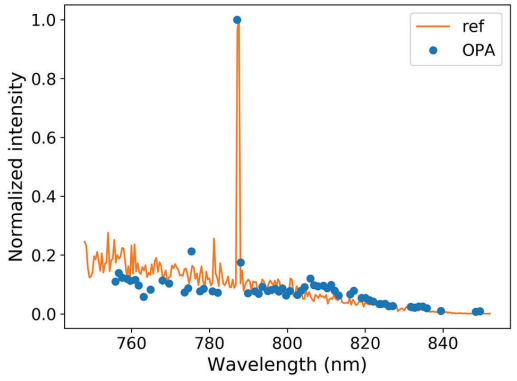

Figure 6.14: Spectrum measured with an OPA spectrometer (blue). The same signal is measured with an OSA as a reference (orange).

6.3 Conclusions

In summary, we demonstrate a hybrid spectrometer based on a Si_3N_4 optical phased array (OPA) that holds the potential of a compact and sensitive spectrometer. The image sensor is spatially separated from the PIC. It is compatible with off-the-shelf, cooled image sensors and free-space filters with a high rejection ratio for the pump wavelength. Enabled by arrayed waveguides and grating couplers, the OPA steers light in two orthogonal directions according to the wavelength. We can deduce the wavelength by measuring the emission direction using a Fourier-space imaging setup. With a small footprint, it can realize high resolution in a wide spectral range. From our calculation, a resolution of 1 nm can be realized using an OPA with 16 strip waveguides that are 800 nm wide. I fabricated and tested an OPA with 32 waveguides on a Si_3N_4 platform. A broadband spectrum is successfully reconstructed with a spectral resolution of 0.5 nm in the range of 750–850 nm. The spectral range can be further expanded by changing the calibration equipment and method. Theoretically, it is only limited by the grating coupler transmission and the NA of the microscope objective.

We will continue developing this spectrometer for on-chip Raman spectroscopy. The spectral resolution and range are sufficient already. It requires additional filters and a cooled camera in the measurement setup. We expect to demonstrate the measurement of a Raman signal or the Raman background of a dielectric waveguide shortly.

7

Conclusions and prospects

7.1 Conclusions

A series of components are relevant to a WERS sensor, including a laser, light-coupling devices, a sensing waveguide, a pump rejection filter, a spectrometer including detectors, and an analyte delivery system. In this thesis, I explored several aspects of such a system to improve the detection limit.

Currently, most works on WERS are conducted on Si_3N_4 platforms using strip or slot waveguides. We are looking for more efficient options for waveguide material and design. In previous works of our group, we experimentally compared the index contrast and Raman background of four different waveguide platforms: Al_2O_3, Si_3N_4, Ta_2O_5, and TiO_2 [50]. Si_3N_4 and Ta_2O_5 are found with relatively high index contrast and low Raman background. Meanwhile, slot waveguides are currently identified as the most efficient geometry for Raman sensing [57]. We first numerically evaluated the performance of a series of Si_3N_4 and Ta_2O_5 slot waveguides and pinpointed the optimal design. Then, in collaboration with the team of Prof. Blumenthal of University of California, Santa Barbara, we fabricated some Ta_2O_5 slot waveguides with slot widths between 40 nm and 150 nm. The Ta_2O_5 layer is 400 nm thick. Due to the narrow slot width, dry etching inside the slot is much slower than outside. It induced a significant over-etching of 500 nm into the buried oxide on the outside. The extreme aspect ratio affects the durability

of the waveguide during measurements. With a slot width of 90 nm, Ta_2O_5 slot waveguide exhibits a 4.8-fold stronger Raman signal of ethanol than a conventional Si_3N_4 slot waveguide.

By coating the waveguide with a tailored adsorbent, analytes in diluted concentrations can be selectively enriched, boosting the detection limit. We employed HMDS-modified mesoporous silica, which has a hydrophobic surface thanks to the methyl groups introduced by the HMDS. The high affinity to hydrophobic compounds helps enrich them from aqueous environments. In collaboration with the team of Prof. Lendl from Vienna University of Technology, we coated some Si_3N_4 slot waveguides with the modified mesoporous silica. We used cyclohexanone as the modal analyte, a hydrophobic, non-polar solvent. We dissolved it in water in low volume concentrations of 0.01%–1% and applied it onto the coated waveguide. As a comparison, it was also dissolved in isopropanol, a non-polar solvent, in higher concentrations (10%–40%) and applied onto a bare Si_3N_4 slot waveguide. On the coated waveguide, 0.01% cyclohexanone (0.97 mM) shows a distinct Raman signal as the enrichment factor reaches 600. The enrichment factor of cyclohexanone grows as the concentration in water decreases due to a limited number of absorption sites. The coated waveguide is expected to boost the detection limit down to the 10-μM level. Simultaneous detection of two non-polar compounds, cyclohexanone and 1-indanone, is also demonstrated. Repeated desorption tests prove good reusability and durability.

Higher coupling efficiency is beneficial when coupling the pump from the high-power laser into the PIC. Currently, we use edge couplers that are lossy and sensitive to alignment. Grating couplers are less sensitive to optical alignment, especially if assisted with micro-lenses. Also, it is well-known that bottom reflectors can boost the coupling efficiency of grating couplers. However, it is costly and time-consuming to include bottom reflectors in existing Si_3N_4 platforms. It prevents the mass production of an efficient WERS sensor. We proposed a micro-transfer-printed Si_3N_4 grating coupler with a metallic bottom reflector. This grating coupler is realized by micro-transfer-printing technology and is compatible with existing mature Si_3N_4 platforms. I developed a process flow in the cleanroom of Ghent University to fabricate such couplers. Various technical problems have been encountered and solved, including filling and planarizing apodized gratings and wet etching of the Si substrate. A coupling efficiency of -2 dB at the wavelength of 840 nm was measured on one of the fabricated devices. It is 3 dB better than standard uniform Si_3N_4 grating couplers and 5 dB better than the edge couplers.

I also worked on integrating a spectrometer on the chip. An on-chip optical phased array can replace the dispersive component in conventional spectrometers. The optical phased array consists of arrayed waveguides with a fixed delay length

difference and grating couplers at their ends. Similar components have been developed for LiDAR and beam steering applications [126, 127]. Light is steered in two orthogonal directions as the wavelength changes. Since each wavelength corresponds to a unique direction, we can deduce a spectrum from its spatial distribution over the image sensor. I designed and fabricated an OPA on a 300 nm Si_3N_4 platform, with 32 waveguides in the array. The footprint is as small as 0.1 mm^2. I achieved a resolution of 0.5 nm over a spectral range of more than 100 nm in the wavelength range of 750–850 nm. A broadband test spectrum is reconstructed with good agreement with the spectrum obtained with a conventional optical spectrum analyzer. In this approach, the image sensor is separated from the PIC. It is convenient to combine with off-the-shelf, cooled image sensors to achieve excellent performance. It is particularly interesting if we prefer to keep the PIC at ambient temperature and use a cooled image sensor for weak signals. Moreover, the rejection ratio of on-chip filters is not yet sufficient to meet the requirement of pump rejection in Raman spectroscopy. With the image sensor separated from the chip, it becomes convenient to add a free-space filter with a high rejection ratio. In the near future, we expect to measure the Raman signal of a dielectric waveguide using the presented spectrometer.

With the optimized waveguide and improved coupling efficiency, the detection limit of the WERS sensor has been improved by over 15 times. If a suitable sorbent is employed, the detection limit can be further boosted by hundreds and thousands of times. The sensor is also more compact with an integrated spectrometer. With the work of this thesis, we are closer to an integrated Raman sensor with high sensitivity, small size, and low cost.

7.2 Prospects

Ta_2O_5 is an interesting material for WERS because of its high index contrast and low Raman background. From simulations and experiments, the optimal slot width is found below 100 nm. There are technical difficulties in fabricating very narrow slots on Ta_2O_5 platforms, on which the fabrication process is not sufficiently mature yet. The wettability of liquid analytes in the narrow slot may also be problematic due to capillary repulsion. Currently, these waveguides cannot replace the conventional Si_3N_4 waveguides, especially not in mass production. One method to circumvent the narrow slot is to functionalize the waveguide with mesoporous silica. With the strong enrichment of the target analyte, the requirement on the slot width can be relaxed. Even with the same narrow slots and high-aspect-ratio waveguides, the mesoporous silica thin film can support the waveguide mechanically. The wettability can also be improved. In mesoporous silica, the distribution of the target

analyte is via surface diffusion, independent of the slot width. However, filling a 40 nm wide slot with mesoporous silica is currently beyond the state of the art. It could become feasible upon investigation as nanoparticles of mesoporous silica with a diameter below 50 nm are already developed [129]. In addition, studies on other relevant components, such as couplers and spectrometers, are necessary to build a complete sensor on this platform.

We have studied the enrichment of non-polar analytes using HMDS-modified mesoporous silica. However, separation based on polarity is relatively coarse in complex samples such as blood and bodily fluids. Despite polarity, there are other mechanisms to selectively adsorb the target analyte, such as ion exchange and adsorption of phenyl groups. The sorbent must be tailored for each type of analyte and the corresponding adhesion mechanism. It requires extensive knowledge of surface chemistry and synthesis to develop the desired sorbent. Since mesoporous silica films have good reusability and reproducibility, the cost per chip in mass production can be low. One method to comprehensively detect multiplexed analytes with various physical and chemical properties is combining different types of sorbent onto one chip. For instance, we can include several sensing waveguides in parallel, each functionalized with a different sorbent. In this way, analytes of a wider variety can be detected using one Raman sensor simultaneously. Another approach is to include in-line pre-separation in the analyte delivery system, such as nanostructured high-performance liquid chromatography (HPLC) columns [130].

Micro-transfer-printing (μTP) technology is well-suited to the massively parallel integration of devices. It is a relatively recent development in homogeneous or heterogeneous integration. Advance in this technology will improve the yield and reproducibility of our μTP grating couplers. It will also be possible to improve the coupling efficiency above -2 dB/port. If the material properties and fabrication process are better controlled, the adiabatic coupler can be replaced by a compact directional coupler, reducing the size of the component. The coupling efficiency of the adiabatic or directional coupler can also be customized to realize signal sampling in post-processing. Thanks to the high coupling efficiency of the grating coupler, the sampling and its effect on the propagating signal can be limited to the minimal. Moreover, an efficient spectrometer can be realized using an array of μTP grating couplers with differently tailored spectral responses, e.g., on an AWG.

With the development of thin-film image sensors, integration with an on-chip OPA can produce a relatively compact spectrometer with excellent spectral range and resolution. However, the signal intensity of an OPA varies significantly for different wavelengths. We can combine several OPA with complementary spectral responses on one chip to realize efficient detection over the entire spectral range. The current design makes the spectrometer quite lossy due to the star coupler and

grating couplers. It can be combined with μTP grating couplers to realize efficient out-coupling. The grating cannot be very long due to the absorption of gold and the short distance between the grating and the bottom reflector. It can be mitigated by extending the distance and the length of the adiabatic coupler. Nonetheless, the absorption might be less severe if a short grating can fulfill the required angular dispersion with a higher steering speed.

In future research, we expect to present a proof-of-concept demonstration of a Raman sensor optimized from the abovementioned aspects. The system may consist of a laser diode, an image sensor, an analyte distribution system, and a photonic chip. As the cost can be low in the production of the photonic chip and microfluidic devices, the system can fulfill demanding applications that require a disposable medium. For instance, monitoring antibiotic concentrations in blood is of essential importance for patients experiencing septic shock. A lower-than-optimal concentration leads to less effective treatments, while a higher concentration results in antibiotic resistance. Meanwhile, the drug concentration in the blood varies among individuals after the same drug administration. Real-time monitoring of antibiotic concentration in blood is in high demand. Raman spectroscopy is promising for its label-free, unambiguous, and fast detection. However, the typical concentration is below 10 mg/L, below the previous detection limit of WERS (10–100 mg/L). In this work, the detection limit is improved by at least a factor of 15, pushing it into the concentration range of antibiotics. A disposable and performant sensor can be developed to improve the survival rate of patients having sepsis. Another example is real-time water quality monitoring, especially for pollutants in water sources. Compared to current methods using fluorescence and UV absorption, WERS offers label-free detection and a less complex system. The typical concentration of pollutants, such as benzene, pesticides, and polycyclic aromatic hydrocarbons, falls below 1 μg/L. This was far below the detection limit of WERS before this study. Now, it becomes feasible using a Si_3N_4 slot waveguide functionalized with properly modified mesoporous silica. Other applications, such as trace gas detection and glucose sensing, may also be realized using this compact, sensitive, and robust Raman sensor.

As the cross-section of Raman scattering scales to $1/\lambda_0^4$, the signal intensity can be drastically increased by reducing the pump wavelength. If the pump wavelength is moved into the mid-UV range, resonance Raman scattering can be excited by the pump photons with energy close to the energy of electronic transitions. Under resonance conditions, the intensity of the Raman signal is significantly enhanced on top of the improved scattering cross-section. As a next step, the Photonics Research Group will continue the research on on-chip Raman spectroscopy in the mid-UV range. As Si_3N_4 and Ta_2O_5 are not transparent in this range, the couplers, waveguides, and spectrometers must be optimized for the new wavelengths on

another UV-compatible platform, e.g., Al_2O_3. The minimum feature size in slot waveguides and grating couplers may decrease significantly because of the reduced wavelength, imposing potential fabrication difficulties. Nevertheless, no theoretical obstacles are foreseen in porting the aforementioned components for a different platform and wavelength.

References

[1] R. Ballerstadt and J. S. Schultz, "A fluorescence affinity hollow fiber sensor for continuous transdermal glucose monitoring," *Analytical Chemstry*, 2000.

[2] S. C. Warren-Smith, E. Sinchenko, P. R. Stoddart, and T. M. Monro, "Distributed fluorescence sensing using exposed core microstructured optical fiber," *IEEE Photonics Technology Letters*, vol. 22, no. 18, p. 2010, 2010.

[3] J.-C. Tinguely, Øystein Ivar Helle, and B. S. Ahluwalia, "Silicon nitride waveguide platform for fluorescence microscopy of living cells," *Optics Express*, vol. 25, no. 22, pp. 27678–27690, 2017.

[4] J. Guo, M. Zhou, and C. Yang, "Fluorescent hydrogel waveguide for on-site detection of heavy metal ions," *Scientific Reports*, vol. 7, p. 7902, 2017.

[5] H. Aouani, O. Mahboub, E. Devaux, H. Rigneault, T. W. Ebbesen, and J. Wenger, "Plasmonic antennas for directional sorting of fluorescence emission," *Nano Letters*, vol. 11, no. 6, pp. 2400–2406, 2011.

[6] W. Deng and E. M. Goldys, "Plasmonic approach to enhanced fluorescence for applications in biotechnology and the life sciences," *Langmuir*, vol. 28, no. 27, pp. 10152–10163, 2012.

[7] W. Liang, Y. Huanga, Y. Xu, R. K. Lee, and A. Yariv, "Highly sensitive fiber Bragg grating refractive index sensors," *Applied Physics Letters*, vol. 86, no. 15, p. 151122, 2005.

[8] Z. Tian, S. S.-H. Yam, J. Barnes, W. Bock, P. Greig, J. M. Fraser, H.-P. Loock, and R. D. Oleschuk, "Refractive index sensing with Mach–Zehnder interferometer based on concatenating two single-mode fiber tapers," *IEEE Photonics Technology Letters*, vol. 20, no. 8, pp. 626–628, 2008.

[9] H.-Y. Lin, C.-H. Huang, G.-L. Cheng, N.-K. Chen, and H.-C. Chui, "Tapered optical fiber sensor based on localized surface plasmon resonance," *Optics Express*, vol. 20, no. 19, pp. 21693–21701, 2012.

[10] J. Jágerská, H. Zhang, Z. Diao, N. L. Thomas, and R. Houdré, "Refractive index sensing with an air-slot photonic crystal nanocavity," *Optics Letters*, vol. 35, no. 15, pp. 2523–2525, 2010.

[11] Y. Xu, P. Bai, X. Zhou, Y. Akimov, C. E. Png, L.-K. Ang, W. Knoll, and L. Wu, "Optical refractive index sensors with plasmonic and photonic structures: Promising and inconvenient truth," *Advanced Optical Materials*, vol. 7, no. 9, p. 1801433, 2019.

[12] G. Antonacci, J. Goyvaerts, H. Zhao, B. Baumgartner, B. Lendl, and R. Baets, "Ultra-sensitive refractive index gas sensor with functionalized silicon nitride photonic circuits," *APL Photonics*, vol. 5, p. 081301, 2020.

[13] Y. Shen, J. Zhou, T. Liu, Y. Tao, R. Jiang, M. Liu, G. Xiao, J. Zhu, Z.-K. Zhou, X. Wang, C. Jin, and J. Wang, "Plasmonic gold mushroom arrays with refractive index sensing figures of merit approaching the theoretical limit," *Nature Communications*, vol. 4, p. 2381, 2013.

[14] M. Nikodem, K. Krzempek, G. Dudzik, and K. Abramski, "Hollow core fiber-assisted absorption spectroscopy of methane at 3.4 μm," *Optics Express*, vol. 26, no. 17, pp. 21843–21848, 2018.

[15] K. J. Kim, P. Lu, J. T. Culp, and P. R. Ohodnicki, "Metal–organic framework thin film coated optical fiber sensors: A novel waveguide-based chemical sensing platform," *ACS Sensors*, vol. 3, no. 2, pp. 386–394, 2018.

[16] W.-C. Lai, S. Chakravarty, X. Wang, C. Lin, and R. T. Chen, "On-chip methane sensing by near-IR absorption signatures in a photonic crystal slot waveguide," *Optics Letters*, vol. 36, no. 6, pp. 984–986, 2011.

[17] S. Alberti, A. Datta, and J. Jágerská, "Integrated nanophotonic waveguide-based devices for IR and Raman gas spectroscopy," *Sensors*, vol. 21, no. 21, p. 7224, 2021.

[18] X. Jia, J. Roels, R. Baets, and G. Roelkens, "A miniaturised, fully integrated NDIR CO2 sensor on-chip," *Sensors*, vol. 21, no. 16, p. 5347, 2021.

[19] R. Stanley, "Plasmonics in the mid-infrared," *Nature Photonics*, vol. 6, pp. 409–411, 2012.

[20] R. Adato and H. Altug, "*In-situ* ultra-sensitive infrared absorption spectroscopy of biomolecule interactions in real time with plasmonic nanoantennas," *Nature Communications*, vol. 4, p. 2154, 2013.

[21] E. Miele, W. M. Dose, I. Manyakin, M. H. Frosz, Z. Ruff, M. F. L. D. Volder, C. P. Grey, J. J. Baumberg, and T. G. Euser, "Hollow-core optical fibre

sensors for operando Raman spectroscopy investigation of Li-ion battery liquid electrolytes," *Nature Communications*, vol. 13, p. 1651, 2022.

[22] B. G. Eleftheriades, E. E. Storey, and A. S. Helmy, "Label-free spontaneous Raman sensing in photonic crystal fibers with nanomolar sensitivity," *Advanced Optical Materials*, vol. 10, no. 6, p. 2101117, 2022.

[23] A. Dhakal, P. C. Wuytens, F. Peyskens, K. Jans, N. Le Thomas, and R. Baets, "Nanophotonic waveguide enhanced Raman spectroscopy of biological submonolayers," *ACS Photonics*, vol. 3, pp. 2141–2149, 2016.

[24] S. A. Holmstrom, T. H. Stievater, D. A. Kozak, M. W. Pruessner, N. Tyndall, W. S. Rabinovich, R. A. McGill, and J. B. Khurgin, "Trace gas Raman spectroscopy using functionalized waveguides," *Optica*, vol. 3, no. 8, pp. 891–896, 2016.

[25] P. L. Stiles, J. A. Dieringer, N. C. Shah, and R. P. V. Duyne, "Surface-enhanced Raman spectroscopy," *Annual Review of Analytical Chemistry*, vol. 1, pp. 601–626, 2008.

[26] F. Peyskens, A. Dhakal, P. Van Dorpe, N. Le Thomas, and R. Baets, "Surface enhanced Raman spectroscopy using a single mode nanophotonic-plasmonic platform," *ACS Photonics*, vol. 3, pp. 102–108, 2016.

[27] A. Bhattarai, I. V. Novikova, and P. Z. El-Khoury, "Tip-enhanced Raman nanographs of plasmonic silver nanoparticles," *The Journal of Physical Chemistry C*, vol. 123, no. 45, pp. 27765–27769, 2019.

[28] M. Fu, M. P. dS. P. Mota, X. Xiao, A. Jacassi, N. A. Güsken, Y. Chen, H. Xiao, Y. Li, A. Riaz, S. A. Maier, and R. F. Oulton, "Near-unity Raman β-factor of surface-enhanced Raman scatteringin a waveguide," *Nature Nanotechnology*, vol. 17, pp. 1251–1257, 2022.

[29] D. L. Dickensheets, D. D. Wynn-Williams, H. G. M. Edwards, C. Schoen, C. Crowder, and E. M. Newton, "A novel miniature confocal microscope/Raman spectrometer system for biomolecular analysis on future Mars missions after Antarctic trials," *Journal of Raman Spectroscopy*, vol. 31, pp. 633–635, 2000.

[30] Y. Komachi, H. Sato, K. Aizawa, and H. Tashiro, "Micro-optical fiber probe for use in an intravascular Raman endoscope," *Applied Optics*, vol. 44, no. 22, pp. 4722–4732, 2005.

[31] J. C. C. Day, R. Bennett, B. Smith, C. Kendall, J. Hutchings, G. M. Meaden, C. Born, S. Yu, and N. Stone, "A miniature confocal Raman probe for

endoscopic use," *Physics in Medicine and Biology*, vol. 54, no. 23, pp. 7077–7087, 2009.

[32] L. X. Quang, C. Lim, G. H. Seong, J. Choo, K. J. Do, and S.-K. Yoo, "A portable surface-enhanced Raman scattering sensor integrated with a lab-on-a-chip for field analysis," *Lab on a Chip*, vol. 8, pp. 2214–2219, 2008.

[33] P. Measor, L. Seballos, D. Yin, and J. Z. Zhang, "On-chip surface-enhanced Raman scattering detection using integrated liquid-core waveguides," *Applied Physics Letters*, vol. 90, no. 21, p. 211107, 2007.

[34] S. Dochow, M. Becker, R. Spittel, C. Beleites, S. Stanca, I. Latka, K. Schuster, J. Kobelke, S. Unger, T. Henkel, G. Mayer, J. Albert, M. Rothhardt, C. Krafft, and J. Popp, "Raman-on-chip device and detection fibres with fibre Bragg grating for analysis of solutions and particles," *Lab on a Chip*, vol. 6, pp. 1109–1113, 2013.

[35] A. Dhakal, F. Peyskens, S. Clemmen, A. Raza, P. Wuytens, H. Zhao, N. Le Thomas, and R. Baets, "Single mode waveguide platform for spontaneous and surface-enhanced on-chip Raman spectroscopy," *Interface Focus*, vol. 6, p. 20160015, 2016.

[36] P. C. Wuytens, A. Z. Subramanian, W. H. De Vos, A. G. Skirtach, and R. Baets, "Gold nanodome-patterned microchips for intracellular surface-enhanced Raman spectroscopy," *Analyst*, vol. 140, no. 24, pp. 8080–8087, 2015.

[37] F. Peyskens, P. Wuytens, A. Raza, P. Van Dorpe, and R. Baets, "Waveguide excitation and collection of surface-enhanced Raman scattering from a single plasmonic antenna," *Nanophotonics*, vol. 7, no. 7, pp. 1299–1306, 2018.

[38] H. Zhao, S. Clemmen, A. Raza, and R. Baets, "Stimulated Raman spectroscopy of analytes evanescently probed by a silicon nitride photonic integrated waveguide," *Optics Letters*, vol. 43, no. 6, pp. 1403–1406, 2018.

[39] A. Dhakal, A. Z. Subramanian, P. Wuytens, F. Peyskens, N. Le Thomas, and R. Baets, "Evanescent excitation and collection of spontaneous Raman spectra using silicon nitride nanophotonic waveguides," *Optics Letters*, vol. 39, no. 13, pp. 4025–4028, 2014.

[40] A. Raza, *Raman spectroscopy enhanced by on-chip dielectric and metal waveguides*. PhD thesis, Ghent University, 2020.

[41] P. J. Larkin, *$Infrared$ and $Raman$ spectroscopy: principles and spectral interpretation*. Elsevier, 2018.

[42] P. Wuytens, *Surface-Enhanced Raman Spectroscopy for Intracellular Sensing and Protease Activity Detection: From Chip Technology to Applications*. PhD thesis, Ghent University, 2018.

[43] R. Weissleder, "A clearer vision for *in vivo* imaging," *Nature Biotechnology*, vol. 19, pp. 316–317, 2001.

[44] S. V. Gaponenko, *Introduction to Nanophotonics*. Cambridge University Press, 2010.

[45] M. Pelton, "Modified spontaneous emission in nanophotonic structures," *Nature Photonics*, vol. 9, pp. 427–435, 2015.

[46] N. Le Thomas, A. Dhakal, A. Raza, F. Peyskens, and R. Baets, "Impact of fundamental thermodynamic fluctuations on light propagating in photonic waveguides made of amorphous materials," *Optica*, vol. 5, no. 4, pp. 328–336, 2018.

[47] P. C. Wuytens, H. Demol, N. Turk, K. Gevaert, A. G. Skirtach, M. Lamkanf, and R. Baets, "Gold nanodome $sers$ platform for label-free detection of protease activity," *Faraday Discussions*, vol. 205, pp. 345–361, 2017.

[48] A. Raza, S. Clemmen, P. Wuytens, M. Muneeb, M. Van Daele, J. Dendooven, C. Detavernier, A. Skirtach, and R. Baets, "ALD assisted nanoplasmonic slot waveguide for on-chip enhanced Raman spectroscopy," *APL Photonics*, vol. 3, no. 11, p. 116105, 2018.

[49] D. M. Kita, J. Michon, and J. Hu, "A packaged, fiber-coupled waveguide-enhanced Raman spectroscopic sensor," *Optics Express*, vol. 28, no. 10, pp. 14963–14972, 2020.

[50] A. Raza, S. Clemmen, P. Wuytens, M. De Goede, A. S. G. Tong, N. Le Thomas, C. Liu, J. Suntivich, A. G. Skirtach, S. M. Garcia-Blanco, D. J. Blumenthal, J. S. Wilkinson, and R. Baets, "High index contrast platforms for on-chip Raman spectroscopy," *Optics Express*, vol. 27, no. 16, pp. 23067–23079, 2019.

[51] F. Dell'Olio and V. M. N. Passaro, "Optical sensing by optimized silicon slot waveguides," *Optics Express*, vol. 15, no. 8, pp. 4977–4993, 2007.

[52] C. A. Barrios, K. B. Gylfason, B. Sánchez, A. Griol, H. Sohlström, M. Holgado, and R. Casquel, "Slot-waveguide biochemical sensor," *Optics Letters*, vol. 32, no. 21, pp. 3080–3082, 2007.

[53] T. Claes, J. G. Molera, K. De Vos, E. Schacht, R. Baets, and P. Bienstman, "Label-free biosensing with a slot-waveguide-based ring resonator in silicon on insulator," *IEEE Photonics Journal*, vol. 1, no. 3, pp. 197–204, 2009.

[54] J. G. Wangüemert-Pérez, P. Cheben, A. Ortega-Moñux, C. Alonso-Ramos, D. Pérez-Galacho, R. Halir, I. Molina-Fernández, D.-X. Xu, and J. H. Schmid, "Evanescent field waveguide sensing with subwavelength grating structures in silicon-on-insulator," *Optics Letters*, vol. 39, no. 15, pp. 4442–4445, 2014.

[55] J. Flueckiger, S. Schmidt, V. Donzella, A. Sherwali, D. M. Ratner, L. Chrostowski, and K. C. Cheung, "Sub-wavelength grating for enhanced ring resonator biosensor," *Optics Express*, vol. 24, pp. 15672–15686, Jul 2016.

[56] H. Yan, L. Huang, X. Xu, S. Chakravarty, N. Tang, H. Tian, and R. T. Chen, "Unique surface sensing property and enhanced sensitivity in microring resonator biosensors based on subwavelength grating waveguides," *Optics Express*, vol. 24, pp. 29724–29733, Dec 2016.

[57] D. M. Kita, J. Michon, S. G. Johnson, and J. Hu, "Are slot and sub-waveguide grating waveguides better than strip waveguides for sensing?," *Optica*, vol. 5, no. 9, pp. 1046–1054, 2018.

[58] V. R. Almeida, Q. Xu, C. A. Barrios, and M. Lipson, "Guiding and confining light in void nanostructure," *Optics Letters*, vol. 29, no. 11, pp. 1209–1211, 2004.

[59] M. Khorasaninejad, W. T. Chen, A. Y. Zhu, J. Oh, R. C. Devlin, C. Roques-Carmes, I. Mishra, and F. Capasso, "Visible wavelength planar metalenses based on titanium dioxide," *IEEE Journal of Selected Topics in Quantum Electronics*, vol. 23, no. 3, pp. 43–58, 2017.

[60] M. P. DeLisa, Z. Zhang, M. Shiloach, S. Pilevar, C. C. Davis, J. S. Sirkis, and W. E. Bentley, "Evanescent wave long-period fiber Bragg grating as an immobilized antibody biosensor," *Analytical Chemistry*, vol. 72, pp. 2895–2900, 2000.

[61] N. Trummer, N. Adányi, M. Váradi, and I. Szendrö, "Modification of the surface of integrated optical wave-guide sensors for immunosensor applications," *Fresenius' Journal of Analytical Chemistry*, vol. 371, pp. 21–24, 2001.

[62] H. Mukundan, A. S. Anderson, W. K. Grace, K. M. Grace, N. Hartman, J. S. Martinez, and B. I. Swanson, "Waveguide-based biosensors for pathogen detection," *Sensors*, vol. 9, pp. 5783–5809, 2009.

[63] B. Mizaikoff, R.Göbel, R.Krska, K.Taga, R.Kellner, M.Tacke, and A.Katzir, "Infrared fiber-optical chemical sensors with reactive surface coatings," *Sensors and Actuators B: Chemical*, vol. 29, pp. 58–63, 1995.

[64] R. Howley, B. D. MacCraith, K. O'Dwyer, P. Kirwan, and P. McLoughlin, "A study of the factors affecting the diffusion of chlorinated hydrocarbons into polyisobutylene and polyethylene-co-propylene for evanescent wave sensing," *Vibrational Spectroscopy*, vol. 31, pp. 271–278, 2003.

[65] Y. K. Wei and J. Yang, "Evanescent wave infrared chemical sensor possessing a sulfonated sensing phase for the selective detection of arginine in biological fluids," *Talanta*, vol. 71, pp. 2007–2014, 2007.

[66] B. J. Melde, B. J. Johnson, and P. T. Charles, "Mesoporous silicate materials in sensing," *Sensors*, vol. 8, pp. 5202–5228, 2008.

[67] B. Baumgartner, J. Hayden, A. Schwaighofer, and B. Lendl, "In situ IR spectroscopy of mesoporous silica films for monitoring adsorption processes and trace analysis," *ACS Applied Nano Materials*, vol. 1, pp. 7083–7391, 2018.

[68] D. Wacht, M. David, B. Hinkov, H. Detz, A. Schwaighofer, B. Baumgartner, and B. Lendl, "Mesoporous zirconia coating for sensing applications using attenuated total reflection Fourier transform infrared (ATR FT-IR) spectroscopy," *Applied Spectroscopy*, vol. 76, pp. 141–149, 2021.

[69] H. Zhao, B. Baumgartner, A. Raza, A. Skirtach, B. Lendl, and R. Baets, "Multiplex volatile organic compound Raman sensing with nanophotonic slot waveguides functionalized with a mesoporous enrichment layer," *Optics Letters*, vol. 45, no. 2, pp. 447–450, 2020.

[70] N. F. Tyndall, T. H. Stievater, D. A. Kozak, K. Koo, R. A. McGill, M. W. Pruessner, W. S. Rabinovich, and S. A. Holmstrom, "Waveguide-enhanced Raman spectroscopy of trace chemical warfare agent simulants," *Optics Letters*, vol. 43, no. 19, pp. 4803–4806, 2018.

[71] Z. Liu, H. Zhao, B. Baumgartner, B. Lendl, A. Stassen, A. Skirtach, N. Le Thomas, and R. Baets, "Ultra-sensitive slot-waveguide-enhanced Raman spectroscopy for aqueous solutions of non-polar compounds using a functionalized silicon nitride photonic integrated circuit," *Optics Letters*, vol. 46, no. 5, pp. 1153–1156, 2021.

[72] J. Rouquerol, D. Avnir, C. W. Fairbridge, D. H. Everett, J. H. Haynes, N. Pernicone, J. D. F. Ramsay, K. S. W. Sing, and K. K. Unger, "Recommendations for the characterization of porous solids," *Pure and Applied Chemistry*, vol. 66, no. 8, pp. 1739–1758, 1994.

[73] C. T. Kresge, M. E. Leonowicz, W. J. Roth, J. C. Vartuli, and J. S. Beck, "Ordered mesoporous molecular sieves synthesized by a liquid-crystal template mechanism," *Nature*, vol. 359, pp. 710–712, 1992.

[74] T. Asefa, M. J. MacLachlan, N. Coombs, and G. A. Ozin, "Periodic mesoporous organosilicas with organic groups inside the channel walls," *Nature*, vol. 402, pp. 867–871, 1999.

[75] S. Che, Z. Liu, T. Ohsuna, K. Sakamoto, O. Terasaki, and T. Tatsumi, "Synthesis and characterization of chiral mesoporous silica," *Nature*, vol. 429, pp. 281–284, 2004.

[76] T. Maschmeyer, F. Rey, G. Sankar, and J. M. Thomas, "Heterogeneous catalysts obtained by grafting metallocene complexes onto mesoporous silica," *Nature*, vol. 378, pp. 159–162, 1995.

[77] J. Liang, Z. Liang, R. Zou, and Y. Zhao, "Heterogeneous catalysis in zeolites, mesoporous silica, and metal-organic frameworks," *Advanced Materials*, vol. 29, p. 1701139, 2017.

[78] B. D. Hatton, K. Landskron, W. J. Hunks, M. R. Bennett, D. Shukaris, D. D. Perovic, and G. A. Ozin, "Materials chemistry for low-k materials," *Materials Today*, vol. 9, no. 3, pp. 22–31, 2006.

[79] M. Comes, M. Marcos, R. Martínez-Máñez, F. Sancenón, J. Soto, L. Villaescusa, P. Amorós, and D. Beltrán, "Chromogenic discrimination of primary aliphatic amines in water with functionalized mesoporous silica," *Advanced Materials*, vol. 16, no. 20, pp. 1783–1786, 2004.

[80] A. Walcarius and L. Mercier, "Mesoporous organosilica adsorbents: nanoengineered materials for removal of organic and inorganic pollutants," *Journal of Materials Chemistry*, vol. 20, pp. 4478–4511, 2010.

[81] V. S. Y. Lin, C.-Y. Lai, J. Huang, S.-A. Song, and S. Xu, "Molecular recognition inside of multifunctionalized mesoporous silicas: toward selective fluorescence detection of dopamine and glucosamine," *Journal of the American Chemical Society*, vol. 123, no. 46, pp. 11510–11511, 2001.

[82] A. Bouamrani, Y. Hu, E. Tasciotti, L. Li, C. Chiappini, X. Liu, and M. Ferrari, "Mesoporous silica chips for selective enrichment and stabilization of low molecular weight proteome," *Proteomics*, vol. 10, pp. 496–505, 2010.

[83] A. Dhakal, A. Raza, F. Peyskens, A. Z. Subramanian, S. Clemmen, N. Le Thomas, and R. Baets, "Efficiency of evanescent excitation and collection of spontaneous Raman scattering near high index contrast channel waveguides," *Optics Express*, vol. 23, no. 21, pp. 27391–27404, 2015.

[84] C. J. Brinker, Y. Lu, A. Sellinger, and H. Fan, "Evaporation-induced self-assembly: nanostructures made easy," *Advanced Materials*, vol. 11, no. 7, pp. 579–585, 1999.

[85] P. H. Eilers, "A perfect smoother," *Analytica Chemistry*, vol. 75, pp. 3631–3636, 2003.

[86] M. Thommes, K. Kaneko, A. V. Neimark, J. P. Olivier, F. Rodriguez-Reinoso, J. Rouquerol, and K. S. W. Sing, "Physisorption of gases, with special reference to the evaluation of surface area and pore size distribution," tech. rep., International Union of Pure and Applied Chemistry, 2015.

[87] J. V. Galán, P. Sanchis, G. Sánchez, and J. Martí, "Polarization insensitive low-loss coupling technique between SOI waveguides and high mode field diameter single-mode fibers," *Opt. Express*, vol. 15, pp. 7058–7065, May 2007.

[88] X. Wang, X. Quan, M. Liu, and X. Cheng, "Silicon-nitride-assisted edge coupler interfacing with high numerical aperture fiber," *IEEE Photonics Technology Letters*, vol. 31, no. 5, pp. 349–352, 2019.

[89] B. Bhandari, C.-S. Im, K.-P. Lee, S.-M. Kim, M.-C. Oh, and S.-S. Lee, "Compact and broadband edge coupler based on multi-stage silicon nitride tapers," *IEEE Photonics Journal*, vol. 12, no. 6, pp. 1–11, 2020.

[90] S. Romero-Garcia, F. Merget, F. Zhong, H. Finkelstein, and J. Witzens, "Visible wavelength silicon nitride focusing grating coupler with AlCu/TiN reflector," *Optics Letters*, vol. 38, no. 14, pp. 2521–2523, 2013.

[91] H. Zhang, C. Li, X. Tu, J. Song, H. Zhou, X. Luo, Y. Huang, M. Yu, and G. Q. Lo, "Efficient silicon nitride grating coupler with distributed Bragg reflectors," *Optics Express*, vol. 22, no. 18, pp. 21800–21805, 2014.

[92] J. Zou, Y. Yu, M. Ye, L. Liu, S. Deng, and X. Zhang, "Ultra efficient silicon nitride grating coupler with bottom grating reflector," *Optics Express*, vol. 23, no. 20, pp. 26305–26312, 2015.

[93] Z. Liu, G. Muliuk, J. Zhang, G. Roelkens, N. Le Thomas, and R. Baets, "Micro-transfer printed silicon nitride grating couplers for efficient on-chip light coupling," in *Proceedings of SPIE: Integrated Optics: Devices, Materials and Technologies XXVI*, p. 1200404, 2022.

[94] E. Menard, K. J. Lee, D. Y. Khang, R. G. Nuzzo, and J. A. Rogers, "A printable form of silicon for high performance thin film transistors on plastic substrates," *Applied Physics Letters*, vol. 84, no. 26, pp. 5398–5400, 2004.

[95] G. Muliuk, K. Van Gasse, J. Van Kerrebrouck, A. J. Trindade, B. Corbett, D. Van Thourhout, and G. Roelkens, "4x25 Gbit/s polarisation diversity silicon photonics receiver with transfer printed III-V photodiodes," *IEEE Photonics Technology Letters*, vol. 31, no. 4, pp. 287–290, 2019.

[96] J. Goyvaerts, S. Kumari, S. Uvin, J. Zhang, R. Baets, A. Gocalinska, E. Pelucchi, B. Corbett, and G. Roelkens, "Transfer-print integration of GaAs p-i-n photodiodes onto silicon nitride waveguides for near-infrared applications," *Optics Express*, vol. 28, no. 14, pp. 21275–21285, 2020.

[97] S. Cuyvers, A. Hermans, M. Kiewiet, J. Goyvaerts, G. Roelkens, K. V. Gasse, D. Van Thourhout, and B. Kuyken, "Heterogeneous integration of Si photodiodes on silicon nitride for near-visible light detection," *Optics Letters*, vol. 47, no. 4, pp. 937–940, 2022.

[98] J. Zhang, B. Haq, J. O'Callaghan, A. Gocalinska, E. Pelucchi, A. J. Trindade, B. Corbett, G. Morthier, and G. Roelkens, "Transfer-printing-based integration of a III-V-on-silicon distributed feedback laser," *Optics Express*, vol. 26, no. 7, pp. 8821–8830, 2018.

[99] C. Op de Beeck, B. Haq, L. Elsinger, A. Gocalinska, E. Pelucchi, B. Corbett, G. Roelkens, and B. Kuyken, "Heterogeneous III-V on silicon nitride amplifiers and lasers via microtransfer printing," *Optica*, vol. 7, no. 5, pp. 386–393, 2020.

[100] J. Goyvaerts, A. Grabowski, J. Gustavssson, S. Kumari, A. Stassen, R. Baets, A. Larsson, and G. Roelkens, "Enabling VCSEL-on-silicon nitride photonic integrated circuits with micro-transfer-printing," *Optica*, vol. 8, no. 12, pp. 1573–1580, 2021.

[101] B. Haq, S. Kumari, K. Van Gasse, J. Zhang, A. Gocalinska, E. Pelucchi, B. Corbett, and G. Roelkens, "Micro-transfer-printed III-V-on-silicon C-band semiconductor optical amplifiers," *Lasers & Photonics Reviews*, p. 1900364, 2020.

[102] C. O. de Beeck, F. M. Mayor, S. Cuyvers, S. Poelman, J. F. Herrmann, O. Atalar, T. P. McKenna, B. Haq, W. Jiang, J. D. Witmer, G. Roelkens, A. H. Safavi-Naeini, R. Van Laer, and B. Kuyken, "III/V-on-lithium niobate amplifiers and lasers," *Optica*, vol. 8, no. 10, pp. 1288–1289, 2021.

[103] D. Taillaert, P. Bienstman, and R. Baets, "Compact efficient broadband grating coupler for silicon-on-insulator waveguides," *Optics Letters*, vol. 29, no. 23, pp. 2749–2751, 2003.

[104] X. Chen, C. Li, C. K. Y. Fung, S. M. G. Lo, and H. K. Tsang, "Apodized waveguide grating couplers for efficient coupling to optical fibers," *IEEE Photonics Technology Letters*, vol. 22, no. 15, pp. 1156–1158, 2010.

[105] W. S. Zaoui, A. Kunze, W. Vogel, M. Berroth, J. Butschke, F. Letzkus, and J. Burghartz, "Bridging the gap between optical fibers and silicon photonic integrated circuits," *Optics Express*, vol. 22, no. 2, pp. 1277–1286, 2014.

[106] A. Bozzola, L. Carroll, D. Gerace, I. Cristiani, and L. C. Andreani, "Optimising apodized grating couplers in a pure SOI platform to -0.5 dB coupling efficiency," *Optics Express*, vol. 23, no. 12, pp. 16289–16304, 2015.

[107] R. Marchetti, C. Lacava, A. Khokhar, X. Chen, I. Cristiani, D. J. Richardson, G. T. Reed, P. Petropoulos, and P. Minzioni, "High-efficiency grating-couplers: demonstration of a new design strategy," *Scientific Reports*, vol. 7, no. 1, p. 16670, 2017.

[108] D. Taillaert, W. Bogaerts, P. Bienstman, T. F. Krauss, P. V. Daele, I. Moerman, S. Verstuyft, K. D. Mesel, and R. Baets, "An out-of-plane grating coupler for efficient butt-coupling between compact planar waveguides and single-mode fibers," *IEEE Journal of Quantum Electronics*, vol. 38, no. 7, pp. 949–955, 2002.

[109] J. T. L. Thong, W. K. Choi, and C. W. Chong, "TMAH etching of silicon and the interaction of etching parameters," *Sensors and Actuators A: Physical*, vol. 63, no. 3, pp. 243–249, 1997.

[110] Allresist, "E-beam resist AR-P 6200 series." https://www.allresist.com/portfolio-item/e-beam-resist-ar-p-6200-series-csar-62/.

[111] I. W. Rangelow, "Critical tasks in high aspect ratio silicon dry etching for microelectromechanical systems," *Journal of Vacuum Science and Technology A*, vol. 21, no. 4, p. 1550, 2003.

[112] M. J. Laboda, C. M. Grove, and R. F. Schneider, "Properties of a-SiOx:H thin films deposited from hydrogen silsesquioxane resins," *Journal of the Electrochemical Society*, vol. 145, no. 8, pp. 2861–2866, 1998.

[113] M. G. Albrecht and C. Blanchette, "Material issues with thin film hydrogen silsesquioxane low k dielectrics," *Journal of The Electrochemical Society*, vol. 145, no. 11, pp. 4019–4025, 1998.

[114] Y. K. Siew, G. Sarkar, X. Hu, J. Hui, A. See, and C. T. Chua, "Thermal curing of hydrogen silsesquioxane," *Journal of The Electrochemical Society*, vol. 147, no. 1, pp. 335–339, 2000.

[115] C.-C. Yang and W.-C. Chen, "The structures and properties of hydrogen silsesquioxane (HSQ) films produced by thermal curing," *Journal of Materials Chemistry*, vol. 12, pp. 1138–1141, 2002.

[116] H.-C. Liou and J. Pretzer, "Effect of curing temperature on the mechanical properties of hydrogen silsesquioxane thin films," *Thin Solid Films*, vol. 335, no. 1–2, pp. 186–191, 1998.

[117] MicroChemicals, "Basics of microstructuring: wet-chemical etching of Si and SiO_2." http://www.microchemicals.com/downloads/application_notes.html.

[118] O. Tabata, R. Asahi, H. Funabashi, K. Shimaoka, and S. Sugiyama, "Anisotropic etching of silicon in TMAH solutions," *Sensors and Actuators A*, vol. 34, pp. 51–57, 1992.

[119] M. Shikida, K. Sata, K. Tokoro, and D. Uchikawa, "Differences in anisotropic etching properties of KOH and TMAH solutions," *Sensors and Actuators*, vol. 80, pp. 179–188, 2000.

[120] P. Cheben, J. H. Schmid, A. Delage, A. Densmore, S. Janz, B. Lamontagne, J. Lapointe, E. Post, P. Waldron, and D. X. Xu, "A high-resolution silicon-on-insulator arrayed waveguide grating microspectrometer with sub-micrometer aperture waveguides," *Optics Express*, vol. 15, no. 5, pp. 2299–2306, 2007.

[121] N. Ismail, L. P. Choo-Smith, K. Wörhoff, A. Driessen, A. C. Baclig, P. J. Caspers, G. J. Puppels, R. M. de Ridder, and M. Pollnau, "Raman spectroscopy with an integrated arrayed-waveguide grating," *Optics Letters*, vol. 36, no. 23, pp. 4629–4631, 2011.

[122] A. van Wijk, C. R. Doerr, Z. Ali, M. Karabiyik, and B. I. Akca, "Compact ultrabroad-bandwidth cascaded arrayed waveguide gratings," *Optics Express*, vol. 28, no. 10, pp. 14618–14626, 2020.

[123] E. Le Coarer, S. Blaize, P. Benech, I. Stefanon, A. Morand, G. Lérondel, G. Leblond, P. Kern, J. M. Fedeli, and P. Royer, "Wavelength-scale stationary-wave integrated Fourier-transform spectrometry," *Nature Photonics*, vol. 1, pp. 473–478, 2007.

[124] X. Nie, E. Ryckeboer, G. Roelkens, and R. Baets, "CMOS-compatible broadband co-propagative stationary Fourier transform spectrometer integrated on a silicon nitride photonics platform," *Optics Express*, vol. 25, no. 8, pp. A409–A418, 2017.

[125] H. Podmore, A. Scott, P. Cheben, A. V. Velasco, J. H. Schmid, M. Vachon, and R. Lee, "Demonstration of a compressive-sensing Fourier-transform on-chip spectrometer," *Optics Letters*, vol. 42, no. 7, pp. 1440–1443, 2017.

[126] K. Van Acoleyen, W. Bogaerts, and R. Baets, "Two-dimensional dispersive off-chip beam scanner fabricated on silicon-on-insulator," *IEEE Photonics Technology Letters*, vol. 23, no. 17, pp. 1270–1272, 2011.

[127] W. D. Sacher, F.-D. Chen, H. Moradi-Chameh, X. Liu, I. F. Almog, T. Lordello, M. Chang, A. Naderian, T. M. Fowler, E. Segev, T. Xue, S. Mahallati, T. A. Valiante, L. C. Moreaux, J. K. S. Poon, and M. L. Roukes, "Optical phased array neural probes for beam-steering in brain tissue," *Optics Letters*, vol. 47, no. 5, pp. 1073–1076, 2022.

[128] P. Muñoz, D. Pastor, L. A. Bru, G. M. Cabanes, J. Benítez, D. Goodwill, and E. Bernier, "Scalable switched slab coupler based optical phased array on silicon nitride," *IEEE Journal of Selected Topics in Quantum Electronics*, vol. 28, no. 5, p. 8300416, 2022.

[129] M. Manzano and M. Vallet-Regí, "Mesoporous silica nanoparticles for drug delivery," *Advanced Functional Materials*, vol. 30, no. 2, p. 1902634, 2020.

[130] T. F. S. Inc., "Low-flow HPLC and UHPLC columns." https://www.thermofisher.com/be/en/home/industrial/chromatography/chromatography-consumables/hplc-uhplc-columns/low-flow-hplc-columns.html.